

## ***Contents — P through S***

---

Estimations of Axial Moment of the Growing Earth <i>G. V. Pechernikova and I. W. Davidenko</i> .....	4015
The Suvasvesi South Structure, Central Finland: Further Evidences of Impact <i>L. J. Pesonen, F. Donadini, J. Salminen, and M. Lehtinen</i> .....	4074
Starting Conditions for Hydrothermal Systems Underneath Martian Craters: 3D Hydrocode Modeling <i>E. Pierazzo, N. A. Artemieva, and B. A. Ivanov</i> .....	4102
Recent Research in the Chesapeake Bay Impact Crater, USA — Part 1. Structure of the Western Annular Trough and Interpretation of Multiple Collapse Structures <i>D. S. Powars, G. S. Gohn, R. D. Catchings, J. W. Horton Jr., and L. E. Edwards</i> .....	4053
Strangelove Ocean and Deposition of Unusual Shallow-Water Carbonates After the End-Permian Mass Extinction <i>M. R. Rampino and K. Caldeira</i> .....	4077
Magnetostratigraphy of the K/T Boundary from Yaxcopoil-1 Borehole, Chicxulub Impact Crater <i>M. Rebolledo-Vieyra and J. Urrutia-Fucugauchi</i> .....	4012
Authigenic and Allogenic Impact Breccias — Open Questions <i>W. U. Reimold, B. O. Dressler, and C. Koeberl</i> .....	4036
Structural Characteristics of the Sudbury Impact Structure, Canada, Point to a Protracted Tectonomagmatic Evolution of the Sudbury Igneous Complex <i>U. Riller and B. O. Dressler</i> .....	4045
Bajo Hondo, a Very Puzzling Crater in Chubut, Patagonia, Argentina <i>M. C. L. Rocca</i> .....	4001
Estancia Los Mellizos: A Potential Impact Structure in Santa Cruz, Patagonia, Argentina, South America <i>M. C. L. Rocca</i> .....	4003
Potential Impact Sites in Southern Argentina: Simple Craters? <i>M. C. L. Rocca</i> .....	4002
Mass-Movement in Geological Strata of Some Astroblemes <i>J. Rondot</i> .....	4007
Structural Investigations in the Central Uplift of the Upheaval Dome Impact Crater, Utah <i>D. Scherler, A. Jahn, and T. Kenkmann</i> .....	4072
Composition of the Late Influx of the Earth <i>G. Schmidt</i> .....	4006
The ICDP Drill Core Yaxcopoil-1, Chicxulub Impact Crater, Mexico: Shock Metamorphism of the Impactite Units (794–894 m) <i>R. T. Schmitt, A. Wittmann, and D. Stöffler</i> .....	4061

Internal Shearing and Subsurface Erosion from the Chicxulub Ejecta Blanket (Albion Fm.), Quintana Roo, Mexico <i>F. Schönian, T. Kenkmann, and D. Stöffler</i> .....	4128
Additional Observations on the Impact Breccias of the Chicxulub Ejecta Blanket from the UNAM-7 Drill Core, Yucatán, Mexico <i>F. Schönian, T. Salge, D. Stöffler, and J. Urrutia Fucugauchi</i> .....	4132
“Fingerprinting” Target Lithologies of the Chicxulub Crater in Ejecta from NE Mexico and Texas: Yucatán Subsurface Revisited <i>P. Schulte, A. Kontny, and W. Stinnesbeck</i> .....	4090
Al-rich Orthopyroxenes in Impact Melt Coatings of Gneiss Bombs from Popigai, Russia — New ATEM Data <i>A.-M. Seydoux-Guillaume, A. Deutsch, and R. Wirth</i> .....	4085
Shocked Quartz at the Permian-Triassic Boundary (P/T) in Spiti Valley, Himalaya, India <i>A. D. Shukla, N. Bhandari, and P. N. Shukla</i> .....	4059
Cratering Process After Oblique Impacts <i>V. V. Shuvalov</i> .....	4130
Mechanisms of Tsunami Generation by Impacts <i>V. V. Shuvalov</i> .....	4131
Experimentally Shock-loaded Anhydrite: Unit-Cell Dimensions, Microstrain and Domain Size from X-Ray Diffraction <i>R. Skála and F. Hörz</i> .....	4093
Diaplectic Glass Content in Experimentally Shock-loaded Quartz Determined by X-Ray Powder Diffraction <i>R. Skála, F. Hörz, and F. Langenhorst</i> .....	4033
Chilling Evidence for the Bulk Composition of the Impact Melt Sheet at Sudbury: Evidence from Offset Dykes <i>J. G. Spray, A. J. Murphy, C. S. J. Shaw, and M. G. Tuchscherer</i> .....	4101
Yaxcopoil-1 and the Chicxulub Impact <i>W. Stinnesbeck, G. Keller, T. Adatte, M. Harting, and D. Stüben</i> .....	4037
Origin and Emplacement of the Impact Formations at Chicxulub, Mexico, with Special Emphasis on the Yax-1 Deep Drilling <i>D. Stöffler, B. A. Ivanov, L. Hecht, T. Kenkmann, R. T. Schmitt, T. Salge, F. Schönian, R. Tagle, S. Weseler, and A. Wittmann</i> .....	4092
Simulations of Very Large Impacts on the Earth <i>V. V. Svetsov</i> .....	4133

## ESTIMATIONS OF AXIAL MOMENT OF THE GROWING EARTH

G.V. Pechernikova, I.W. Davidenko, Institute for Dynamics of Geospheres RAS, 38 Leninsky prosp. (bldg. 1), 119334 Moscow, Russia, avit@idg.chph.ras.ru.

**Introduction.** 30 yrs of analytical modeling and numerical simulation have revealed two general stages in the terrestrial accretion process: 1) stage in which planetesimals experience runaway growth and form lunar-sized “planetary embryos” in approximately  $10^5 - 10^6$  years; and 2) final stage dominated by mutual gravitational perturbations between embryos, resulting in large, stochastic impact events and formation of the final terrestrial planets after about  $10^8$  years. Recent dynamical models of lunar formation in the giant impact scenario have raised new complicating issues. It was shown that (a) the angular momentum of the Earth-Moon system could have resulted from more than one impact, (b) the moon-forming impact may not have been the last large impact on the Earth [1-3].

Some tentative results of calculations of mass increase of the planet  $m$  and corresponding planetary spin  $\mathbf{K}$  in the new model [4] are presented. Our aim is to estimate the number of macro-impacts (with masses  $m_{imp} > 10^{26}$  g) and impact angular momenta and the evolution of planetary spins during the late stage of terrestrial planet formation in the framework Standard Scenario of the Solar System formation [5-9] with the use of new model.

Up to now there is a competition between the model where planets are gradually spun up and another model where a massive late-stage impact dominates. Both of these models have its preferences and its disadvantages.

Our model combines analytical (I) and statistical (II) approaches where the planetesimals swarm evolution (including the growth of the RMS planetesimal velocities  $\bar{v}$  and the corresponding increase of the width of a planet’s feeding zone  $2\Delta R$ , decrease in surface density of condensed matter  $\sigma_d$ , the change of the total mass of matter in the expanding feeding zone  $Q$ , the change of upper limit of mass distribution  $M$ ) is

calculated according to analytical theory [5-7] and impacts of largest bodies to the planet are treated statistically. We assume complete mergers upon collisions in all cases.

**I. Analytical part.** According to [5] we have  $\bar{v} = (Gm/\theta r)^{1/2} \propto m^{1/3}$ , where  $\theta \sim 2$ ,  $m$  is the mass of the growing planet. Such quantities as  $\Delta R \cong \bar{e}R \cong \bar{v}R/V_K \propto m^{1/3}$ ,  $\sigma_d = \sigma_0[1 - (m/m_\oplus)^{2/3}]$ ,  $\sigma_0 = 10 \text{ g/cm}^2$ ,  $M = [1 - (m/m_\oplus)^{2/3}]m$ ,  $Q = (m/m_\oplus)^{-2/3}m$  (here  $V_K$  is the Kepler circular velocity at the distance  $R$ ,  $m_\oplus$  is the present Earth’s mass) are calculated as functions of  $m$ . The time of the planet growth to the mass  $m$  is

$$t = (t_0/P_\oplus) \ln[(1 + (m/m_\oplus)^{1/3}) / (1 - (m/m_\oplus)^{1/3})],$$

where  $t_0/P_\oplus = \delta r_\oplus / [2(1+2\theta)\sigma_0]$ . It is suggested that the angular momentum vector for the axial spin of a planet  $\mathbf{K}$ , inclined at an angle  $\varepsilon$  to axis  $z$  ( $z$  is perpendicular to the orbital plane), is equal to the sum of the regular component  $\mathbf{K}_1$ , which is directed along axis  $z$  and the random component  $\mathbf{K}_2$ , which is inclined at an angle  $\gamma$  to  $z$ .  $\mathbf{K}_1$  is calculated as a function of mass  $m$  according to [5, 6].

**II. Simulation.** We calculated a growth dynamics beginning from the initial value of the mass  $m = 0.001 m_\oplus$ . At every step of calculation, the values of parameters enumerated in the previous section were calculated. Then, one of 10 largest bodies ( $k = 1, 2, 3, \dots, 10$  in order of mass decreasing) from the hierarchy mass spectrum with an exponent  $q$  was selected in a random manner as an impactor. Mass  $m_k$  of the selected  $k$ -th body was estimated according to power law distribution by the method described in [10] as

$$m_k = \left[ 1 + \frac{q-1}{2-q} (k-1) \frac{M}{Q-m} \right]^{(2-q)/(1-q)} (Q-m) - \left[ 1 + \frac{q-1}{2-q} k \frac{M}{Q-m} \right]^{(2-q)/(1-q)} (Q-m).$$

The increase of mass of the growing planet on each step is equal to  $m_k + \Delta m$ , where  $\Delta m$  is determined as corresponding fraction of masses of more small bodies ( $k > 10$ ). The increase of the random component  $\mathbf{K}_2$  due to impact by  $m_k$  is defined with the use of additional five stochastically determined values, that are three components of the impactor velocity  $V_{imp\ x}$ ,  $V_{imp\ y}$  and  $V_{imp\ z}$  and two coordinates of the impact point on the planet's surface - the angles  $\Theta$  and  $\Phi$ .

**Results.** Figure 1 illustrates 4 of our simulations in which a model of "particle-in-a-box" with Maxwell velocity distribution was suggested. The angular momentum delivered to the planet by the largest impactors in this model may be considered as a minimum. In presented simulations from 5 to 7 bodies with masses  $> 10^{26}$  g impacted to the growing planet.

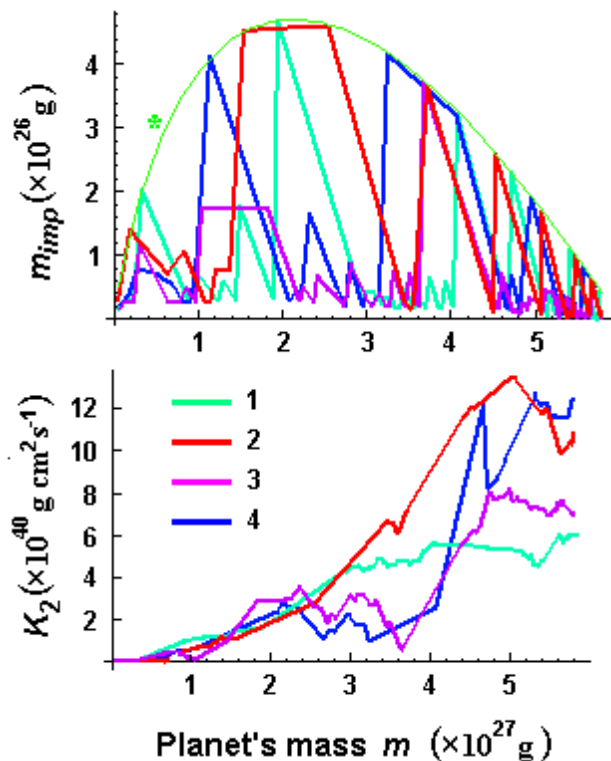


Figure 1. The impactor masses (top) and increase of the modulus of the random momentum  $\mathbf{K}_2$  (bottom) as a function of the growing planet's mass are presented. The change of upper limit of mass distribution  $M(m)$  is shown by the curve "\*" (top).

The current angular momentum of the Earth-Moon system  $\mathbf{K}_{\oplus-M} = 3.45 \cdot 10^{41}$  g cm<sup>2</sup>/s, and assuming an "early-earth" rotation period of 10 hours we obtain  $\mathbf{K} = 1.4 \cdot 10^{41}$  g cm<sup>2</sup>/s,  $\mathbf{K}_1 = 6.5 \cdot 10^{40}$  g cm<sup>2</sup>/s and  $\mathbf{K}_2 = 7.7 \cdot 10^{40}$  g cm<sup>2</sup>/s for early-Earth respectively.

**References.** [1] Richardson, D.C. *et al.* (2000) *Icarus* **143**, 45-59. [2] Pechernikova, G.V., and A.V. Vityazev (1996) *LPSC XXVII* 1213-1214. [3] Agnor, C.B., *et al.* (1999) *LPSC XXX*, 1878. [4] Davidenko, I.W., A.V. Vityazev and G.V. Pechernikova (2001) *The 34<sup>th</sup> Vernadsky-Brown Microsymposium on comparative planetology*, Moscow. [5] Vityazev, A.V., and G.V. Pechernikova (1991) *Planet. Sci., American and Soviet Research - Proceedings from the US-USSR Workshop on Planetary Sciences*. (T.M.Donahue, K.K.Trivers, D.M.Abramson, Eds.), 143-162. National Academy Press, Washington. [6] Vityazev, A.V., G.V. Pechernikova and V.S. Safronov (1990) *Terrestrial Planets: Origin and Early Evolution*. Nauka Press, Moscow. [7] Safronov, V.S., (1969) *Evolution of the Proto-planetary Cloud and Formation of the Earth and Planets*. Nauka Press, Moscow. [8] Wetherill, G.W., (1986) In *Origin of the Moon* (Hartmann, W.K., *et al.*, Eds.) 519-550, Houston, LPI. [9] Stevenson, D.J., (1987) *Ann. Rev. Earth and Planet Sci.* **15**, 271-315. [10] Safronov, V.S., and E.V. Zvjagina (1969) *Icarus* **10**, 109-118.

## THE SUVASVESI SOUTH STRUCTURE, CENTRAL FINLAND: FURTHER EVIDENCES OF IMPACT.

L.J. Pesonen<sup>1</sup>, F. Donadini<sup>1</sup>, J. Salminen<sup>1</sup> and M. Lehtinen<sup>2</sup>, <sup>1</sup>Division of Geophysics, University of Helsinki, P.O. Box 64, 00014 Helsinki, Finland; Lauri.Pesonen@helsinki.fi), <sup>2</sup>Geological Museum, University of Helsinki, P.O. Box 64, 00014 Helsinki, Finland (Martti.Lehtinen@helsinki.fi)

**Introduction:** The Suvasvesi South structure is located in Central East Finland (62°41'N, 28°11'E) and correlates with the Haapaselkä open lake, the southern of the two circular Suvasvesi lakes. The target rock consists mainly of Proterozoic mica schists and migmatites in its easternmost part and granitoids in the western part. Suvasvesi S was first perceived in satellite images [1], and might form a crater doublet with the Suvasvesi N impact structure [2]. We have previously presented evidences, such as presence of fractured target rocks and shatter-cone boulders on the eastern shore of Haapaselkä, which suggest that the Suvasvesi S is also an impact structure [2]. During the summer 2002 we carried out a new field survey in the area. The new bathymetric and geophysical data, coupled with thin section studies of the discovered melt boulders confirm that the Suvasvesi S is a new impact structure in Finland.

**Target and Impact Rocks:** The target rock of the Suvasvesi South crater consists mainly of Proterozoic mica schists and migmatites in its easternmost part and granitoids in its western part. The morphology is strongly effected by Quaternary ice movements: the outcrops are smoothed, rounded and show at the surface distinct glacial striations.

**New Field Discoveries:** All the investigated outcrops show mainly closed fractures. The two dominant fracture families are subvertical, N-S and E-W oriented. In particular, Takunluoto islet, located near the centre of the Suvasvesi South structure, consists mainly of heavily fractured granitoids. Shatter cone-like features were observed in outcrops at three different places. Their orientation is clearly different from the tectonic deformation trends. However, decimeter long striated structures may be the result of glacial erosion, even though the linear direction of both structures points toward the centre of the crater. Still, it is unsure if those are the result of glacial erosion or impact. At Takunluoto islet, possible in situ shatter cones of 50 cm length were observed. Also in this case, however, the cones are weakly developed and may be slickenslide structures originated by the heavy fracturing.

Several boulders proving impact evidence were collected in the easternmost part of the Suvasvesi S structure. These shatter cones were found in mica schist and granitoid boulders along the NW coast of Haapasaari island and at Lusikkaniemi bay. Further cutting in the laboratory revealed that such boulders might consist of breccia containing granitoid clasts of few cm in size. In such a case the cones developed on the granitoid clasts. Finding of such boulders is restricted to particular areas: the Lusikkaniemi and the Haapasaari region, about one km away from each other.

We collected several impact melt boulders along in gravel pits along the roadsides at Mannamäki hill, about 5 km southeast of the structure (Fig. 1). The rock consists of a fine-grained black matrix with fluidal texture, alternated with cm-sized clasts of target rock. Both the impact lithologies showed planar deformation features (PDFs) in quartz grains and a breccia structure. PDFs can be distinguished as two different sets and are mainly decorated, meaning that syngenetic impact fluid inclusions were present. Breccia structure is distinguishable because of the fine-grained matrix surrounding the bigger quartz or feldspar grains. Instead, the granite sample collected in situ did not show any impact evidence. It should be noticed that the thin sections were prepared also for Takunluoto granitic sample, which represents the strongly fractured outcrop on the islet near to the centre of impact. Clasts are mainly melted, vesiculated or crushed.



Fig. 1: Impact melt boulder from a gravel pit near Mannamäki hill, Suvasvesi South, Finland. This sample is about 10cm long. Photo: Kari A. Kinnunen.

**Summary:** The new discoveries during the field trip to the Suvasvesi South area strengthen the hypothesis of an impact origin. The boulders show all the evidences of shock metamorphism, i.e. shatter cones, PDFs, diaplectic and melt glass, brecciation, kink bands and fluidal textures. In situ structures like shatter cones are weakly developed and difficult to recognize. However, the directions of shatter cone-like features point toward the center of the structure and not from the Northern one. Measurements of ice flow directions, show that the boulders should be transported from the southern structure. The location of the boulders in restricted areas suggests either that erosion has been acting differently or that lithologies were not ho-

mogeneously distributed. One other interpretation may be also related to the fragility and easy weathering of impact rocks, which may have been crushed during glaciations.

In the light of our observations, one would suggest that Suvasvesi S aroused from a small projectile. This would explain the weak magnetic anomaly and a lack of central peak anomaly, the reasonably shallow bathymetric profile and the poorly developed impact features in outcrops. In the same way, the discovery of boulders in the eastern part of the structure, together with the magnetic anomaly map may indicate that a small impact layer is still present near the submerged impact centre. Erosion could be another possible explanation for the lack of impact evidences in situ. However, studies on the Suvasvesi N impact structure favour a relatively young (ca. 260-280 Ma) event [3]. Bathymetric and airborne magnetic and electromagnetic data point also to a distinct structure of smaller dimension than the northern one.

We are now studying the paleomagnetism of the fractured and target rocks in order to find further evidences of impact and to check if the two structures have same age. Modeling the erosion of the structure would allow determining the probability that the two events represent a doublet [4].

**References:** [1] Pesonen, L.J., Lehtinen, M., Deutsch, A., Elo, S., Lukkarinen, H., 1996. LPSC 27, 1021-1022. [2] Lehtinen, M., Pesonen, L.J., Kuulusa, M., 2002. LPSC 33. [3] Werner, S.C., Plado, J., Pesonen, L.J., Janle, P., Elo, S., 2002. Physics and Chemistry of the Earth, vol. 27, 1237-1245. [4] Bottke, F. and Melosh, H.J., 1996. Icarus, 124, 372-391.

## STARTING CONDITIONS FOR HYDROTHERMAL SYSTEMS UNDERNEATH MARTIAN CRATERS: 3D HYDROCODE MODELING.

E. Pierazzo<sup>1</sup>, N.A. Artemieva<sup>2</sup>, and B.A. Ivanov<sup>2</sup>, <sup>1</sup>Planetary Science Institute (620 N. 6<sup>th</sup> Ave., Tucson, AZ 85705; betty@psi.edu), <sup>2</sup>Institute for Dynamics of Geospheres (Russian Academy of Sciences, Leninsky pr., 38-6, 117334, Moscow, Russia; art@idg.chph.ras.ru; ivanov@idg.chph.ras.ru).

**Introduction:** Mars is the most Earth-like of the other planets of the Solar System. With widespread evidence of both heat sources and water, Mars is the first place to look for any sign of present or past extraterrestrial life. The presence of sub-surface water and surface ice or liquid water reservoirs throughout the Martian history is rather evident [1] and it has received further confirmation by the current Odyssey mission [2,3,4]. On the Martian surface, impact cratering and volcanism have provided temporary heat sources throughout Mars geologic history. This alters locally the thermal evolution of a mixed ice-rock sub-surface mixture, and could cause the onset of a hydrothermal circulation.

The realization that hydrothermal systems are possible sites for the origin and early evolution of life on Earth [e.g., 5,6,7] has given rise to the hypothesis that hydrothermal systems may have had the same role on Mars [8,9,10]. The ample evidence for hydrothermal circulation underneath terrestrial impact structures suggests that hydrothermal system could have formed underneath large Martian impact structures as well [11]. Rough estimates of the heat generated in impact events, as initial conditions for the development of an impact-related hydrothermal system, have been based on scaling relations [e.g., 12,13]. Preliminary studies [14,15] suggest that the melt sheets and target uplift are equally important heat sources for the development of a hydrothermal system, while the lifetime of a hydrothermal system depends on the cooling rate of the heat source, as well as the permeability of the host rocks.

Numerical studies of the thermal evolution of the target during an impact event have been carried out for specific terrestrial cases using two-dimensional (2D) impact simulations [16,17]. We present preliminary results of three-dimensional simulations of impacts on Mars aimed at constraining the initial conditions for modeling the onset and evolution of a hydrothermal system on the red planet. The simulations of the early stages of impact cratering allow us to determine the amount of shock melting and the pressure-temperature distribution in the target caused by various impacts on the Martian surface. The late stage of crater collapse are then necessary to determine the final thermal state of the target, including crater uplift, and the final

distribution of the melt pool, heated target material and hot ejecta around the crater.

**Early stage:** Simulations of the early stage of the impact event are carried out with the 3D hydrocode SOVA, developed at the Institute for Dynamics of Geospheres [18], coupled to tabular equations of state built from the ANEOS package [19]. 3D benchmark tests have shown that SOVA produces shock melting and vaporization patterns and volumes similar to the well-known CTH.

We model spherical comets and asteroids of various sizes impacting Mars' surface at 15.5 and 8 km/s, respectively. These roughly correspond to median impact velocities for short-period comets and for asteroids. Simulations have been carried out for 90° (vertical), and 45° impact angles (most probable angle of impact). A spatial resolution of 20 to 25 cells-per-projectile-radius (cpr) is maintained over a central region (only the  $y > 0$  half space is modeled, where the  $y < 0$  half space is its mirror image) around the impact point, followed by regions of progressively lower resolution, extending to about 13 km downrange (and 5 km uprange), and 15 km below (9 km above) the surface. Tabular versions of ANEOS equations of state for granite (no basalt ANEOS is available at this time), and water ice or granite are employed to model the target and projectile respectively. Ideally, we should model a mixed target, where the basic crystalline crust contains a component of ice and/or liquid water. While the initial simulations use a single material (granite) target, we are exploring how using a mixed material, granite and water, for the target may affect the distribution of the shock in the target and the final estimate of melting during the early stage of impact cratering. A very thin CO<sub>2</sub> atmosphere was included in the simulations as well to model the present-day Martian atmosphere, although this is not expected to influence the thermal characterization of the target.

Over 1200 Lagrangian tracers are regularly distributed inside the (model half-) target to record the material's thermodynamic evolution (with time steps of 0.005 seconds). These tracers record temperatures and pressures as well as positions and velocities during the impact. To estimate melt volumes as accurately as possible, we use a second set of tracers to mark each computational cell of the target around the impact

point (of given volume), for a total of more than 500,000 tracers. Volume estimates are determined by adding up the volume of tracers experiencing shock pressures above a given threshold. We use 46 and 56 GPa as threshold pressures for incipient and complete melting of pure granite.

Table 1 shows melt volumes,  $V_m$ , associated with impacts producing a final crater (rim to rim) of about 33 km, according to Pi-scaling laws (code use for estimates developed by H.J. Melosh: see [www.lpl.arizona.edu/tekton/crater.html](http://www.lpl.arizona.edu/tekton/crater.html)), for comet and asteroid impacts ( $D_{pr}$  is the diameter of impactor,  $v_{imp}$  and  $\theta_{imp}$  are impact velocity and angle, respectively). These results indicate that impact velocity plays a very important role in determining the total volume of melt produced in the impact. In particular, cometary impacts, because of their larger impact velocities, are much more efficient in creating larger melt pools whose longer cooling time may contribute to a longer duration of the hydrothermal system under an impact crater. The maximum depth at which shock pressure reaches the threshold for 50% vaporization of water (20 GPa),  $D_{vap}$ , is also shown. Initial shock vaporization of water may affect the onset of the hydrothermal circulation.

Type	$D_{pr}$ (km)	$v_{imp}$ (km/s)	$\theta_{imp}$	$V_m$ ( $km^3$ )	$D_{vap}$ (km)
Comet	2	15.5	90°	31.6	4.9
Comet	2.32	15.5	45°	32.5	4.5
Asteroid	2	8	90°	4.1	4.8
Asteroid	2.32	8	45°	3.7	1.9

**Late Stages:** The final temperature field around an impact crater depends both on the shock compression/decompression cycle and friction heating due to plastic deformation. As the geothermal heat flow gradient is responsible for an increase in temperature downward, material uplifted from below during the formation of the central peak/ peak ring in complex craters is at higher temperatures that surrounding material, thus providing a further source of heat. For a complete picture of the thermal field underneath an impact crater it is thus necessary to follow the entire crater-forming event, from impact to the final crater. To model crater formation and the formation of the final crater, we use the 2D hydrocode SALE [20]. Originally developed for calculating 2D fluid flow, SALE has been modified for modeling impact cratering [21,22], and has so far been used to model the formation and thermal evolution of several terrestrial impact structures of various sizes and their thermal fields, from Kärdla (Estonia,  $D\sim 4$  km), to Ries (Germany,  $D\sim 23$  km), to Sudbury (Canada,  $D\sim 250$

km). We found that for the smallest craters the 373K isotherm, corresponding to the boiling point of water, is buried only  $\sim 1$  km below the crater floor. For craters in the 20-40 km range (Figure 1), the 373K isotherm reaches a depth of about 5 km. For even larger craters the extent of a post-impact hydrothermal system seems to be controlled by the permeability of the rocks under lithostatic pressure. On Mars, the lower gravity should allow less self-compaction of rocks under a crater than on Earth, thus increasing the region where a potential hydrothermal system could develop. For detailed estimates, however, we will use the early stage modeling as a starting point for modeling crater collapse on Mars,

**References:** [1] Carr M.H. (1996) *Water on Mars*, Oxford Univ. Press (New York). [2] Boynton, W.V. et al. (2002) *Science*, 297, 81. [3] Feldman W.C. et al. (2002) *Science*, 297, 75. [4] Mitrofanov I. et al. (2002) *Science*, 297, 78. [5] Corliss J.B. et al. (1981) *Ocean. Acta*, SP, 59. [6] Baross J.A., Hoffman S.E. (1985) *Origins Life*, 15, 327. [7] Holm N.G. (1992) *Origins Life Evol. Biosph.*, 22, 5. [8] Farmer J. (1996) In *Evolution of hydrothermal ecosystems on Earth (and Mars?)*, G. Bock, J. Goode Eds. (Wiley, New York), 273. [9] Farmer J., Des Marais D.J. (1999) *J. Geophys. Res.*, 104, 26977. [10] Newsom H.E. et al. (2001) *Astrobiol.*, 1, 71. [11] Rathbun J.A., Squyres S.W. (2002) *Icarus*, 157, 362. [12] Grieve R.A.F., Cintala M.J. (1992) *Meteoritics*, 27, 526. [13] Clifford S.M. (1993) *J. Geophys. Res.*, 98, 10973. [14] Daubar I.J., Kring D.A. (2001) LPSC, 32, #1727. [15] Thorsos I.E. et al. (2001) LPSC, 32, #2011. [16] Ivanov B.A., Deutsch A. (1999) *GSA Spec. Pap.* 339, 389. [17] Turtle E.P. et al. (2003) *Meteor. Planet. Sci.*, 38. In Press. [18] Shuvalov V. (1999) *Shock waves*, 9, 381. [19] Thompson S.L., Lauson H.S. (1972) *SC-RR-61 0714*, Sandia Nat. Labs. [20] Amsden A.A. et al. (1980) *LA-8095*, Los Alamos Nat. Labs. [21] Ivanov B.A. (1994) *GSA Spec. Pap.*, 293, 81. [22] Ivanov B.A., Kostuchenko V.N. (1997) *LPSC*, 27, #1655.

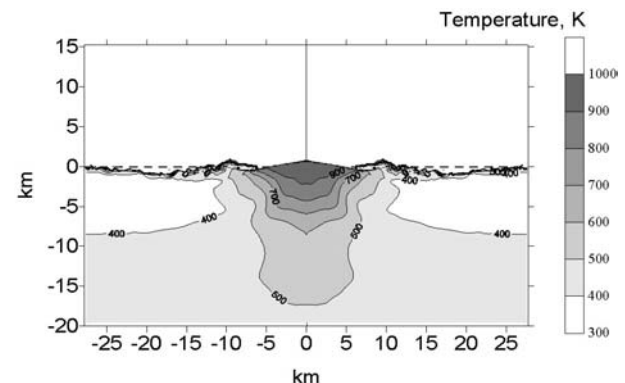


**Figure 1:** Post-impact temperature field for Puchezh-Katunki crater (Russia,  $D\sim 40$  km). Sedimentary layer (wet tuff) over granite basement, projectile 3.8 km in diameter, 15 km/s impact velocity, computational cell 200x200 m.

**RECENT RESEARCH IN THE CHESAPEAKE BAY IMPACT CRATER, USA—PART 1. STRUCTURE OF THE WESTERN ANNULAR TROUGH AND INTERPRETATION OF MULTIPLE COLLAPSE STRUCTURES.** D.S. Powars<sup>1</sup>, G.S. Gohn<sup>1</sup>, R.D. Catchings<sup>2</sup>, J.W. Horton, Jr.<sup>1</sup>, and L.E. Edwards<sup>1</sup>; <sup>1</sup>USGS, MS 926A, National Center, Reston, VA 20192; <sup>2</sup>USGS, 345 Middlefield Rd., Menlo Park, CA 94025

**Introduction:** The buried late Eocene Chesapeake Bay impact structure is a complex crater formed in a multi-layered, marine target. The target consisted of a neritic water column, 400 to >750 m of lower Tertiary and Cretaceous sediments, and underlying crystalline rocks. The 85-km-wide crater has a subquadrate, ~38-km-wide inner basin that is surrounded by a ~24-km-wide, flat-floored annular trough. The annular trough's outer margin has a slumped terrace zone surrounded by a ~35-km-wide outer fracture zone.

New insights into the stratigraphic and structural configuration of the annular trough come from correlation of four deep coreholes and two corehole velocity logs with marine seismic-reflection surveys and a high-resolution, land-based, reflection survey (CDP spacing of 2.5m). The high-resolution survey is adjacent to two of the coreholes and provides sufficient resolution to delineate small structures.

**Outer-margin structures:** On the seismic profiles, the outer margin of the annular trough separates discontinuous, locally inclined or offset reflectors, which are interpreted as large slumped fault blocks and overlying ocean-resurge and tsunami deposits, from relatively continuous, horizontal reflectors that represent little-disturbed Cretaceous sediments outside the margin. These relatively undisturbed sediments appear fractured and faulted but to a much lesser degree than the slump blocks. Inward-dipping normal faults and antithetic faults define the typically rotated slump blocks. The major normal faults displace the sediment-crystalline rock contact, indicating that they are relatively deep seated.

Resurge-tsunami and overlying post-impact sediments buried the irregular upper surface of the slump blocks. Observed thickness variations, dip reversals, and fault displacements of these sediments probably result from differential compaction across the underlying irregular surface. The impact-generated resurge-tsunami deposits are up to 100 m thick in the annular trough but abruptly thin to 7.5 m just outside the outer rim in one corehole.

**Collapse structures:** Interpretation of the marine seismic surveys indicates that numerous extensional collapse structures are present across the western annular trough. Most of these structures disrupt parautochthonous Cretaceous sediments, resurge-tsunami sediments, and post-impact sediments but do not deform the underlying crystalline rocks, thereby suggesting

detachment zones within the sedimentary section. The high-resolution survey shows a collapse structure that significantly affects only the variably deformed parautochthonous beds below the resurge-tsunami and post-impact sediments. The high-resolution survey also shows that the extensional collapse structures are formed by abundant short, small-displacement faults and are not grabens bounded by a few long, large-displacement normal faults.

Correlation of the collapse structures across the seismic grid suggests that they are concentrated in three narrow structural rings. The width of these rings varies from 0.5 to 3.9 km, and their inner edges are located at about 8, 15, and 22 km from the inner-basin rim. Between these rings, the sedimentary section appears relatively undeformed. A denser seismic dataset likely would reveal a more complex pattern with discontinuous individual structures and intervening transfer zones.

The internal structure of the sedimentary section of the annular trough of the Chesapeake Bay impact crater typically has been described as slumped, normal-fault-bounded megablocks overlain by a resurge-tsunami diamicton (Exmore beds). This model likely remains accurate for the large slump blocks at the outer margin but may need to be revised to account for the shallow collapse structures, and a paucity of megablocks, in the remainder of the annular trough. The shallow collapse structures invite comparison with similar shallow extensional features recently observed in the Silverpit crater of the North Sea.

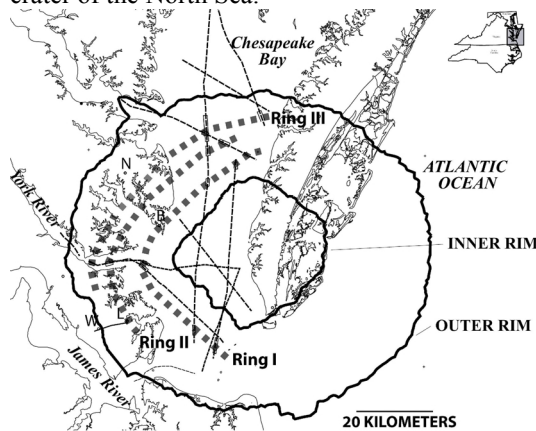


Figure 1. Map showing interpreted structural rings (heavy dotted lines) superimposed on seismic tracks (thin dashed lines) in the Chesapeake Bay impact crater.

## Strangelove Ocean and Deposition of Unusual Shallow-Water Carbonates After the End-Permian Mass Extinction.

Rampino, Michael R., Earth and Environmental Science Program, New York University, 100 Washington Square East, New York, New York 10003, USA ([mrr1@nyu.edu](mailto:mrr1@nyu.edu)), and NASA, Goddard Institute for Space Studies, New York, NY 10025, USA.

Caldeira, Ken, Lawrence-Livermore National Laboratory, Livermore, C 94551, USA.

The severe mass extinction of marine and terrestrial organisms at the end of the Permian Period (~251 Ma) was accompanied by a rapid negative excursion of ~3 to 4 per mil in the carbon-isotope ratio of the global surface oceans and atmosphere that persisted for some 500,000 into the Early Triassic. Simulations with an ocean-atmosphere/carbon-cycle model suggest that the isotope excursion can be explained by collapse of ocean primary productivity (a Strangelove Ocean) and changes in the delivery and cycling of carbon in the ocean and on land. Model results also suggest that perturbations of the global carbon cycle resulting from the extinctions led to short-term fluctuations in atmospheric pCO<sub>2</sub> and ocean carbonate deposition, and to a long-term (>1 Ma) decrease in sedimentary burial of organic carbon in the Triassic (Figs. 1 and 2).

Deposition of calcium carbonate is a major sink of river-derived ocean alkalinity and for CO<sub>2</sub> from the ocean/atmosphere system. The end of the Permian was marked by extinction of most calcium carbonate secreting organisms. Therefore, the reduction of carbonate accumulation made the oceans vulnerable to a build-up of alkalinity and related fluctuations in atmospheric CO<sub>2</sub>. Our model results suggest that an increase in ocean carbonate-ion concentration should cause increased carbonate accumulation rates in shallow-water settings. After the end-Permian extinctions, early Triassic shallow-water sediments show an abundance of abiogenic and microbial carbonates that removed CaCO<sub>3</sub> from the ocean and may have prevented a full "ocean-alkalinity crisis" from developing.

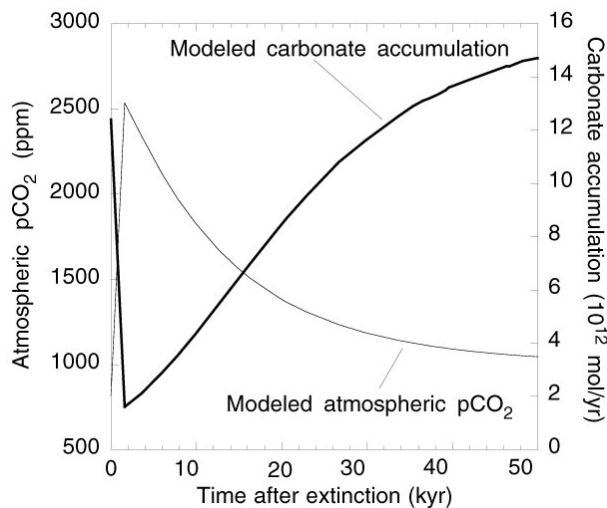


Figure 1: Results of model simulation for shallow-water carbonate accumulation rates (mol/year) and atmospheric pCO<sub>2</sub> (ppm) for the first 50,000 years after a sudden ocean productivity collapse.

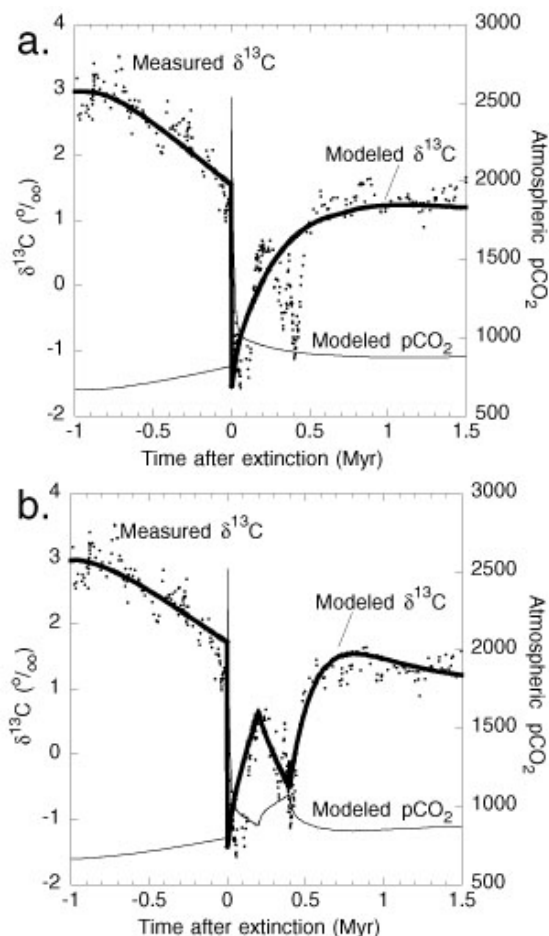


Figure 2. A: Results of model simulation for delta<sup>13</sup>C of ocean-surface waters compared with data from the GK-1 core from the Carnic Alps, Austria (black dots). In this case, the second delta<sup>13</sup>C shift at ~300 ka after the extinction event is interpreted as a local signal. B: Results of model simulation considering that the delta<sup>13</sup>C shift at of ocean-surface waters ~300 ka after the extinction event represents a global signal. This run includes partial recovery of productivity followed by a second collapse, and a reduction in the rate of burial of organic carbon. The long-term shift in model surface-water delta<sup>13</sup>C from late Permian to Early Triassic was simulated by a 15% decrease in organic carbon burial. Also plotted is the predicted perturbation of atmospheric pCO<sub>2</sub> calculated by the model.

**MAGNETOSTRATIGRAPHY OF THE K/T BOUNDARY FROM YAXCOPOIL-1 BOREHOLE, CHICXULUB IMPACT CRATER.** M. Rebolledo-Vieyra<sup>1,2</sup> and J. Urrutia-Fucugauchi<sup>1</sup>, <sup>1</sup>Laboratorio de Paleomagnetismo, Instituto de Geofísica, UNAM, Circuito Exterior S/N, Cd. Universitaria, Coyoacan, D.F., 04510, Mexico. <sup>2</sup>Laboratoire des Sciences du Climat et de l'Environnement, Unité de recherche mixte CEA/CNRS Avenue de la Terrasse, Bât. 12, 91198 Gif-sur-Yvette Cedex, France. marior@lsce.cnrs-gif.fr, +33-16982-3527

Recently a debate on the position of the K/T boundary within ICDP-UNAM borehole Yaxcopoil-1 has arisen.

We report the magnetostratigraphy of K/T boundary and the base of Paleocene conducted on samples recovered by the Chicxulub Scientific Shallow Drilling Program. A sharp contrast of the magnetic susceptibility, from diamagnetic range up to  $8000 \times 10^{-6}$  SI, marks the contact between the Tertiary and impact lithologies. Samples of impact breccias show a reverse polarities which spans up to  $\sim 40$  cm in to the Tertiary lithologies. We correlate this breccias to those of PEMEX borehole Yucatan-6, from which we tie our magnetostratigraphy to the radiometric age from this borehole. We consider that the reversal

polarity within the impact breccias lies within the 29R chron, which contains the K/T limit. The Polarities recorded span from the magnetochron 29R to 29N. In this borehole we found a 36 cm interval between the K/T and the change in polarity, suggesting that the sedimentation during the 250,000 years from the K/T boundary to the polarity shift, was in the range of  $6.5 \times 10^{-3}$  cm/yr, suggesting a very low sedimentation rate, or a hiatus of the base of Paleocene. We propose that the K/T limit in Yaxcopoil-1, is located at the contact between the impact series and the Tertiary sedimentary sequence, at 794.43 m and not at the last occurrence of redeposited suevite at 794 m proposed by other authors.

**AUTHIGENIC AND ALLOGENIC IMPACT BRECCIAS – OPEN QUESTIONS.** W.U. Reimold<sup>1</sup>, B.O. Dressler<sup>2</sup>, and C. Koeberl<sup>3</sup>. <sup>1</sup>ICRG, School of Geosciences, Univ. of the Witwatersrand, Private Bag 3, P.O. Wits 2050, Johannesburg, South Africa (reimoldw@geosciences.wits.ac.za); <sup>2</sup>185 Romfield Circuit, Thornhill, Ontario, Canada (burkhard@attcanada.net); <sup>3</sup>Dept. of Geological Sciences, Univ. of Vienna, Althanstrasse 14, A-1090 Vienna, Austria (christian.koeberl@univie.ac.at).

**Introduction:** Between the 1960s and 1980s, a considerable number of detailed, mostly mineralogical and geochemical studies of impact breccias in and outside of terrestrial impact structures, as well as in the available lunar rock and meteorite record, have been carried out. Since then, a rather limited number of groups has pursued this line of research. Many issues have remained either controversial or unresolved. This has recently been emphasized when a series of quite anomalous impact breccias were intersected in the Yaxcopoil-1 borehole in the Chicxulub impact structure. It, thus, is timely to revisit these impactite issues and attempt an inventory of current knowledge and remaining problematics. The timeliness of this attempt is further emphasized by the current efforts of impact researchers to compare their multidisciplinary data sets and cross-fertilize the discipline of impact cratering studies [1].

**Status:** One outcome of the first round of concerted impact breccia studies has been a comprehensive impactite nomenclature, as proposed to the IUGS Subcommission on the Systematics of Metamorphic Rocks [2]. Despite this generally widely accepted nomenclature, the application of regional or local terminology for impact melt rocks (e.g., tagamite, kárnäite) is still widespread. In addition, a nomenclature based on the notion that impactites are catastrophically generated rocks and, thus, applying the prefix “copto-“ is also still applied – mostly in countries of the former USSR [e.g., 6]. Main issues raised with the proposed IUGS nomenclature include the use of the terms “fragmental breccia” and “pseudotachylite”.

The controversial use of the term “pseudotachylite” has been widely debated in recent years [e.g., 3-5]. In this regard the problematics of distinguishing between impact melt rock, friction melt, and shock-*cum*-shearing derived melt must be emphasized. This also relates to the discussion of the origin of so-called “shock veins” in meteorites, which are observed as thin veinlets either directly related to narrow vein-parallel zones of strongly enhanced shock pressure with high-pressure polymorphs or not. In addition, the multifold A, A1, A2, B, B1, B2, E, S-type nomenclature is controversial [5], and the often difficult or impossible identification of primary breccia types after hydrothermal and/or metamorphic overprint need to be recognized. Besides the discussion of which physical processes form “pseudotachylitic breccias”, temporal and spatial issues must be considered: at which

stage(s) in the cratering process are such breccias formed and where in the evolving or modified crater? Naturally, this latter aspect is not reserved for “pseudotachylitic breccias” only, but relates to the formation of any type of dike breccia [e.g., 7,8]. Problematic are also whether “pseudotachylitic breccia” is formed preferentially in annular zones around large impact structures, as suggested for Sudbury and disputed for the deeply eroded Vredefort impact structure, and by which process (enhanced shock pressure, friction, or both). Are the sometimes massive breccias in the Vredefort Dome the result of friction melt generation of fault planes followed by intrusion into dilational openings, or of enhanced shock compression ± friction? What is the origin of the breccias in the central part of the dome – where higher grade shock pressure than further outwards contrasts a somewhat lesser volume of breccia than in the outer part of the core of the Dome?

**Some Open Questions:** Other issues that still need to be resolved include:

- Where in the evolving crater are the various constituents of impact breccia generated, how effective is the mixing process, and how are the products of mixing deposited – and where? This not only concerns the mixtures of melt and clastic components of suevitic and polymict lithic breccia, but also the origin of impact melt breccia.
- How are the various products of shock deformation transported and deposited, within and outside of craters, and even globally (in this latter case, with special regard to the distribution of melt and projectile-derived material)?
- Is there a relationship between spherule layers (distal impact ejecta beds) and the chondrules/globules described from various impact breccia occurrences (e.g., Ries crater, Chicxulub/Yax-1)?
- What do the Archean impact breccia layers (spherule beds) imply about large Archean impact events? Why are several such impact spherule beds known from the Archean-Proterozoic record and are, with one notable exception, absent from the later rock record? Why are Archean spherule layers more or less devoid of shocked minerals, whereas the oldest known impact structures on Earth (Vredefort and Sudbury) actually contain abundant evidence of macroscopic and microscopic shock deformation?

- Is it possible to explain the settings of pseudotachylitic breccias as the consequence of compressional and/or extensional impact tectonics?
  - What do impact breccias in the subcrater environment tell us about shock compression and crater modification? Are these regimes in large, complex impact structures related to a mega-brecciation process? And how does “pseudotachylitic breccia relate to formation of central uplifts and possibly to the concept of “acoustic fluidization”?”
  - It was recently proposed that (a) pseudotachylites occurring in the central parts of impact structures form during the compression phase of the cratering event, whereas “clastic-matrix” breccias form during the modification phase of impact cratering, on the basis of breccia-in-breccia and cross-cutting breccia relationships [8]. Does this generalization stand up to the record?
  - What influence have target rocks on the formation of breccias in target rocks – i.e. why are some central uplifts practically unbrecciated (e.g., Manicouagan), whereas the central uplifts of other structures (e.g., Slate Islands) consist of about 20% breccia?
  - Why is there such a variation in the occurrence and distribution of shatter cones in impact structures, and how exactly (and when in the sequence of impact crater formation) do they actually form?
  - How widespread is the occurrence of carbonate melts in impact structures? Are there melt rocks based only on carbonate, and, most importantly, how do we characterize and recognize shocked carbonates in the field and in the laboratory?
  - The distribution and incorporation of a meteoritic component in impact breccias is a largely unresolved question. Why are some breccias/melt rocks relatively rich in an extraterrestrial component (e.g., Morokweng, Sudbury, Clearwater), whereas other impact structures, seemingly formed by similar types of projectiles, have no detectable or a very low abundance of meteoritic material? Why are the interelement ratios of, e.g., the siderophile elements, in impact glasses from small craters for which the meteorites are preserved different than the values in the actual meteorites? Obviously some fractionation takes place, but no known physical process has been identified to be responsible for this fractionation.
  - Why are there such large variations in the amount of meteoritic components in impact breccias from some craters (e.g., the huge variations observed in samples from West Clearwater), but in other craters the meteoritic component is much more evenly distributed?
  - Are there any impact structures that do really contain differentiated impact melt bodies? Some melt bodies do show some variation in composition, but does this imply a differentiated melt sheet or was the cooling of the melt body too fast for such a process and materials of different zones derived from different parts of the crater structure?
  - Another chemical issue is mostly related to Sudbury, where melt rocks of different chemical compositions are found in the Sudbury Igneous Complex and Offset Dikes. Can this be explained by melt mixing and subsequent differentiation or assimilation of large amounts of target rock? How does this compare with the extremely homogeneous Granophyre dikes in the Vredefort structure?
- Conclusions:** It is obvious that further concerted effort is required to solve these and other remaining questions regarding the formation and emplacement of impactite deposits. This has to be done in a combination of field work (geology, geophysics, remote sensing, drilling...), laboratory studies (petrography, geochemistry, geochronology...), and theoretical modeling/numerical calculations. In this respect the upcoming drilling projects, largely under the auspices of the International Continental Scientific Drilling Program (ICDP), at several impact structures (e.g., Bosumtwi, Chesapeake Bay, Sudbury, Elgygytgyn) are of great importance and will produce not only large amounts of samples and data but also will provide an interdisciplinary forum for the investigation of impact craters, and generate interest among the geological community.
- Acknowledgments:** CK is supported by the Austrian Science Foundation (project Y58-GEO) and the Wits ICRG from the NRF of RSA.
- References:** [1] Impact Cratering: Bridging the Gap Between Modeling and Observations; LPI Contrib. 1155. [2] Stöffler, D. & Grieve, R.A.F., Impact Cratering and Evolution of Planet Earth, Lockne-94, 2<sup>nd</sup> Int. ESF Workshop, The Identification and Characterization of Impacts, Östersund, Sweden, 31/5-5/6/1994, 3 pp.; and Stöffler D. and Grieve R.A.F., 1994, Lunar Planet. Sci. 25, 1347-1348. [3] Reimold, W.U., 1995, Earth-Sci. Rev. 39, 247-264. [4] Reimold, W.U., 1998, Earth-Sci. Rev. 43, 25-47. [5] Reimold, W.U., 2002, Abstracts of the 8<sup>th</sup> European Science Foundation “Impact” Programme Workshop, “Impact tectonics”, Mora, Sweden, p. 36. [6] Deutsch, A. et al. (eds.), 2003, The Puchezh-Katunki Deep Drilling Project (updated translation from the Russian), Impact Studies Series, Springer-Verlag, Heidelberg, in preparation [7] Lambert, P., 1981, Proc. Lunar Planet. Sci. Conf. 12A, pp. 56-78. [8] Dressler, B.O. & Reimold, W.U., 2003, Earth-Sci. Rev., in revision.

## STRUCTURAL CHARACTERISTICS OF THE SUDBURY IMPACT STRUCTURE, CANADA, POINT TO A PROTRACTED TECTONOMAGMATIC EVOLUTION OF THE SUDBURY IGNEOUS COMPLEX.

U. Riller<sup>1</sup> and B. O. Dressler<sup>2</sup>, <sup>1</sup>Humboldt-Universität zu Berlin, Museum für Naturkunde, Invalidenstrasse 43, 10115 Berlin, Germany, ulrich.riller@museum.hu-berlin.de, <sup>2</sup>185 Romfield Circuit, Thornhill, Ontario, Canada, L3T 3H7; burkhard@attcanada.ca.

**Introduction:** The Sudbury Impact Structure, Ontario, is widely regarded as the relic of a large multi-ring impact basin, the centre of which is considered to be defined by the exposed portion of the synformal Sudbury Igneous Complex (SIC), e.g., [1]. In most impact models, the main mass of the SIC is believed to have formed entirely by fusion of upper crust followed by static differentiation of the resulting impact melt sheet into the observed basal quartz-dioritic Sublayer and overlying norite, quartz gabbro and granophyre layers, respectively. Based on inference from crater-floor geometry of lunar multi-ring basins and numeric modelling, the basal contact of this melt sheet is required to have been horizontal prior to tectonic modification. Evidence for the multi-ring nature of the Sudbury Impact Structure hinges strongly on the assertion that zones of pseudotachylite and impact breccia in the tectonically least affected area north of the SIC connect to concentric zones, i.e. structural rings. By contrast, a number of well-documented structural characteristics of the Sudbury Impact Structure have not been considered in any impact model but point to a more complex tectono-magmatic evolution of the Sudbury Impact Structure and as a consequence, of terrestrial multi-ring structures in general.

**Structural Characteristics:** Clearly, orogenic deformation at Sudbury strongly hampers a straightforward assessment of impact-induced geological processes that generated the Sudbury Impact Structure. Nonetheless, the structural continuity of pre-impact lithological units, bordering on the southern SIC, to a distance of up to 100 km from the western SIC suggests little differential rotation within these units and thus within the SIC following its emplacement [2]. This is corroborated by low magnitudes of solid-state tectonic strain and the preservation of magmatic fabrics in the norite and the granophyre even in zones where the curvature of both is maximal in plan view [3]. Furthermore, the norite and quartz gabbro are unstrained where the South Range Shear Zone, a post-impact ductile thrust fault, transects the SIC, e.g., [4], [5]. In fact, prolate and oblate magmatic fabrics in the granophyre and norite layers, respectively, suggest that these units did not share the same tectono-magmatic history [3]. Collectively, these relationships indicate that the norite was emplaced after the granophyre. Similarly, the presence of norite inclusions in the quartz-dioritic sublayer and quartz-diorite dikes in the norite,

indicates emplacement of the Sublayer after solidification of the norite [4]. In summary, these structural relationships point to a prolonged tectono-magmatic evolution of the SIC upon impact.

**Centre Of The Sudbury Impact Structure:** Pre-impact rocks immediately south of the SIC are affected most by localized and distributed impact brecciation. This area is regarded by many geoscientists as the southern portion of the innermost crater characterised by crater wall collapse. As a consequence, radial and concentric quartz diorite dikes in this area have been considered as impact melt-filled discontinuities that formed by differential slumping of crater wall segments towards the crater centre, e.g., [6], [7]. The structural continuity of pre-impact lithological boundaries in this area, however, casts doubt on this interpretation of radial and concentric quartz-diorite dikes. Also, the centro-symmetric strain field, i.e. converging rock flow toward the apparent crater centre, imposed by such slumping on collapsing crater wall terraces is unfavourable for magma propagation through such discontinuities. Alternatively, this area may represent the central portion of the impact structure, i.e. part of the root zone of the transient central uplift, exhumed by post-impact NW-directed thrusting on the South Range Shear Zone. Upon collapse, structures formed as a consequence of transient uplift were truncated and covered by impact melt and subject to further impact-induced crater modification. A crude structural 3-D restoration of the primary geometry of the SIC suggests, however, that the SIC did not solidify as a horizontal melt sheet [3]. Both primary parabolic geometry and prolonged tectono-magmatic evolution of the SIC point to a protracted phase of crater modification that may have even outlasted consolidation of the impact melt. In such a scenario, the pervasive presence of impact breccia bodies and quartz-diorite dikes south of the SIC are best explained in terms of discontinuous deformation induced by the formation of a transient central uplift.

**References:** [1] Grieve R. A. F. (1991) *JGR*, 96, 22753-22764. [2] Riller U. and Schwerdtner W. M. (1997) *GSAB*, 109, 841-854. [3] Cowan E. J. et al. (1999) *GSA Spec. Paper*, 339, 399-418. [4] Dressler B. O. (1996) *Geochimica et Cosmochimica*, 60, 2019-2036. [5] Riller U. et al. (1998) *Tectonophysics*, 287, 59-75. [6] Spray J. G. (1997) *Geology*, 25, 579-582. [7] Scott R.G. and Benn K. (2002) *Geology*, 29, 747-750.

**BAJO HONDO, A VERY PUZZLING CRATER IN CHUBUT, PATAGONIA, ARGENTINA.**

M. C. L. Rocca , Mendoza 2779-16A, Ciudad de Buenos Aires, Argentina, (1428DKU),maxrocca@hotmail.com.

This work was funded by the Planetary Society, CA, USA.

**Introduction:** Bajo Hondo is a very puzzling crater in Chubut Province, Patagonia, Argentina, ( S 42°15' W 67° 55').

Diameter: 4.8 kilometers. It has a 100-150 meters raised rim and several decametric blocks are visible on its Western rim.

Its proportions match perfectly those of a simple impact crater. Bajo Hondo is located in the Somuncura Plateau, 10 km. SE to the Talagapa stratovolcano.

The whole Somuncura Plateau is composed of volcanic rocks, mainly Oligocene-Miocene basaltic floods and ignimbrite deposits. Bajo Hondo has been interpreted in the past as a collapsed basaltic caldera , [ 1,2 ].

The same happened in the case of Lonar Lake, India: a 1.8 kilometers well confirmed impact crater in the Deccan Basaltic plateau, [ 3 ]. However close examination of satellite LANDSAT images and aerial photographs of Bajo Hondo reveals possible flaws in that interpretation. A reported volcanic cone on the Western rim is probably just a collapsed part of that rim. The association of lava floods to Bajo Hondo is also doubtful. Probably the reported ones were erupted by Talagapa and not by Bajo Hondo itself.

Rocks exposed on Bajo Hondo's rims are clearly piroclastic: basaltic breccia, glass bombs and glassy scoriae.

Those rocks are present in Lonar Lake's rim,[ 3 ].

Explosive origin is evident. The question is: Volcanic or Impact? Bajo Hondo is probably too big to be a Maar.

The author believes it is in fact a misinterpreted gigantic simple impact crater. If it is in fact an impact then Bajo Hondo is very important because it would be a gigantic simple crater and at the same time an impact crater in basaltic rocks. The site demands more research.

**References:** [ 1 ] Ardolino A. and Delpino D.: ( 1986 ), Revista Asociacion Geologica Argentina ( RAGA ), 41( 3-4), pp. 386-396, ( In Spanish ); [ 2 ] Ardolino A. : ( 1987), "Descripcion Geologica de la Hoja 42 f, Sierra de Apas ", in Boletin N° 203 Direccion Nacional de Minería y Geología, Buenos Aires, 91 pps., ( in Spanish ); [ 3 ] Fredriksson K. et al. (1973), Science 180, pp. 862-864.

**ESTANCIA LOS MELLIZOS: A POTENTIAL IMPACT STRUCTURE IN SANTA CRUZ, PATAGONIA, ARGENTINA, SOUTH AMERICA.**

M. C. L. Rocca , Mendoza 2779-16A, Ciudad de Buenos Aires, Argentina, (1428DKU), maxrocca@hotmail.com.  
This work was funded by The Planetary Society, CA, USA.

**Introduction:** The Southern part of Argentina has a total surface of 786,112 square kilometers. It is composed of five Provinces: Neuquen, Rio Negro, Chubut, Santa Cruz and Tierra del Fuego.

So far no impact sites has been reported in this wide zone.

As a part of an on-going project to discover meteorite impacts, this area was investigated by the author through the examination of 76 color LANDSAT satellite images ( 1:250,000 - resolution = 250 meters ) at the Instituto Geografico Militar ( IGM ) (=Military Geographic Institute) of Buenos Aires city.

When a potential candidate was found a more detailed study of images was done. LANDSAT color images; scale 1:100,000 ( IGM ), and aerial photographs; scale 1: 60,000 ( IGM ), were then consulted .

One promising site to be a complex impact structure was identified in Santa Cruz .

The co-ordinates given bellow are those of the two corners of a rectangle enclosing the site: the upper left and the lower right points. That is the system used at IGM to obtain the data. Further evaluation of this site is in progress.

**Estancia Los Mellizos**, Ruta Provincial N° 39.

Area: W 70° 10' S 47° 15' / W 69° 50' S 47° 28'

Possible eroded and covered complex structure.

In this site there is a circular feature of ridges and low hills. Diameter: 15 km.

The DLR's X-SAR images ql 10028 ( La Española ) and ql 10029 ( Cerro Cojudo Blanco ) also show this circular structure.

The geology of this entire area is not very well known. Apparently, it is composed of degraded volcanic (ignimbrite and piroclastic rocks) of Chon Aike Fm. of Jurassic age, ( 170 - 140 Ma ). ( geologic map 4769-III, 1:250,000, SEGEMAR ( =Geological Survey of Argentina ) , 1998), [ 1 ].

**References:** [ 1 ] Barrio de R., Panza J.L. and Nullo F.E. (1999) Geología Argentina : Caminos R. Editor, SEGEMAR Anales N° 29, 511-527. ( in Spanish )

**POTENTIAL IMPACT SITES IN SOUTHERN ARGENTINA: SIMPLE CRATERS?**

M. C. L. Rocca , Mendoza 2779-16A, Ciudad de Buenos Aires, Argentina, (1428DKU), maxrocca@hotmail.com.  
This work was funded by The Planetary Society, CA, USA.

**Introduction:** The Southern part of Argentina has a total surface of 786,112 square kilometers. It is composed of five Provinces: Neuquen, Rio Negro, Chubut, Santa Cruz and Tierra del Fuego. So far no impact sites has been reported in this wide zone. As a part of an on-going project to discover meteorite impacts, this area was investigated by the author through the examination of 76 color LANDSAT satellite images ( 1:250,000 - resolution = 250 meters ) at the Instituto Geografico Militar ( IGM ) (=Military Geographic Institute) of Buenos Aires city. When a potential candidate was found a more detailed study of images was done. LANDSAT color images; scale 1:100,000 ( IGM ), and aerial photographs; scale 1: 60,000 ( IGM ), were then consulted . A few potential simple impact craters were identified. The co-ordinates given bellow are those of the two corners of a rectangle enclosing the site: the upper left and the lower right points. Further evaluation of these sites is in progress.

**NEUQUEN PROVINCE.** 1 ) Meseta de la Barda Negra. Area : W 70° 00' S 39° 00' / W 69° 45' S 39° 25'

Possible simple crater in black Miocene's ( radiometric ages : 14 to 10 Ma ) basaltic plateau. Diameter: 1.5 km. Raised rim. There are no visible lava flows coming from this crater.

The crater was described as a "salitral" (= salty pan shape basin ) containing blocks, conglomerates and sands on the geologic map of the Province by SEGEMAR(= Geological Survey of Argentina), [ 1 ].

**SANTA CRUZ PROVINCE.** 2 ) Meseta del Lago Buenos Aires-(Site A). W 70° 50' S 46° 54' / W 70° 46' S 46° 57'

Possible simple crater of 0.3 Km. Raised rim. The area is composed of Pliocene's basalts ( radiometric ages: 7 to 3 Ma ),[ 2 ]. 3 ) Meseta del Lago Buenos Aires-( Site B). W 71° 10' S 47° 00' / W 71° 30' S 47° 05'. Possible simple crater of 1.0 Km. Similar to Lonar Lake impact crater, India,[ 3 ]. The area is composed of basalts of Pliocene age ( 7 to 3 Ma ),[ 2 ]. 4 ) Gran Altiplanicie Central. W 70° 10' S 48° 23' / W 70° 05' S 48° 28'. Possible eroded simple crater in basaltic upper Miocene's plateau ( c.a. 12 to 11 Ma ). Diameter: 1.0 km.. [ 4, 5 ].

**References:** [ 1 ] Suero T. (1951) Carta y Hoja Geologica 36c Cerro Lotena, SEGEMAR Boletin N° 76, 67 pp. ( in Spanish); [ 2 ] Giacosta R. And Franchi M. (2001) Carta y Hoja Geologica 4772-IV Lago Belgrano y Lago Posadas, SEGEMAR, 61pp. ( in Spanish ); [ 3 ] Fredriksson K. et al. (1973 )Lonar Lake, India: An Impact Crater in Basalt: Science **180**, pp. 862-864.; [ 4 ] Panza J. L. and Marin G. (1998) Carta y Hoja Geologica 54d. Boletín SEGEMAR N° 239, 104 pp. ( in Spanish ); [ 5 ] Ardolino A. et al.(1999) Geologia Argentina: Caminos R. Editor, SEGEMAR Anales N° 29 , 579-612. ( in Spanish )

**MASS-MOVEMENT IN GEOLOGICAL STRATA OF SOME ASTROBLEMES.** J. Rondot, Astroblème Exploration, 1111 rue d'Amiens, Sainte-Foy, Qc, Canada G1W 4C8. email: mrondot@cegep-ste-foy.qc.ca.

**Introduction:** The impact of large meteorites results in the displacement of two main rock types apart from the relatively undisplaced autochthonous target rocks. The first type consists of allochthonous rocks which, during the formation of a transient crater, are transformed and displaced from their original position, in part to great distances: deposits of breccia, suevite, impactite, etc. They lie on the crater floor and beyond. The second type are parautochthonous rocks which are composed of sedimentary or crystalline rock assemblages which have preserved their internal coherence, but are separated by faults containing a particular kind of breccia indicating a long period of relative movements, which are often contradictory. From a geological point of view, the relative positions of these rock assemblages with respect to their original position provides indications on their displacements during the readjustment which followed the excavation of the original crater.

**Observations:** The displacement of parautochthonous rock masses is recognized with the help of the bedding of the sedimentary rocks which is usually horizontal. The first evident displacement, which also defines the diameter of the structure, is the collapse in terraces of a sedimentary cover. It is generally not observable on earth because of the erosion, hence the name "astrobleme" rather than a "crater" for the whole structure. The first normal faults locally create openings where the allochthonous rocks were engulfed as we can see in Charlevoix astrobleme. In Charlevoix astrobleme, we can observe, on the Precambrian rocks, a cover of Ordovician limestone 100 to 200 m of thickness. It appears from 4 to 6 km from the rim. In these first zones, the rocks are in a subhorizontal position forming terraces, more than 5 km<sup>2</sup> in area in the western part, and about 4 km long in the eastern part. The most evident collapse of the rocks forms a ring graben where cover strata are folded and depressed to a depth of more than 1 km with respect to their initial position in Charlevoix. The presence, nearly continuous, of a thin layer of sedimentary cover rocks in several astroblemes allows to estimate the diameter of the excavated crater to be about half of the diameter of the astrobleme. Ring graben are also visible in other astroblemes. The relics of a thin cover of limestone over an ancient peneplane, are observable in the structures of Manicouagan (50 m), Siljan (400 m), West-Clearwater, etc. The Carswell structure also has, at the same distance relative to the centre, a ring graben of rocks which have totally disappeared from the surrounding areas by erosion. A central uplift is evident in structures affecting the sedimentary rocks: Wells Creek, Sierra Madera, etc. The kind of deformation affecting the sedimentary rocks of the central uplift is

well studied in the Sierra Madera structure. It indicates movements towards the centre and upwards. The same observation can be made in Charlevoix. Here Cambrian and Ordovician strata show tectonic repetition and a centrifugal dip in a zone of uplift visible along a distance of 20 km and with a maximum width of 5 km, southeast of the St Laurent fault.

**Models:** Several models have been proposed to explain the displacement of parautochthonous rock assemblages. In most cases they use the effect of gravity on homogeneous material surrounding the transient crater. The calculations carried out indicate movement of material near the border of the cavity, along listric faults, towards the centre of the depression. The cohesion of rock material limits the displacements to a narrow zone parallel to the slope. In order to reduce material cohesion and to enlarge the affected zone, some envisage acoustic fluidization of the material. But, the movement of large masses of material at depth involves movement along well-defined surface. The proposed model implies the development of deep-seated faults during the descent of the meteorite. Such fractures have been observed in laboratory experiments involving the plunging of a pillar into compacted sand. The sand did not move in a continuous manner, but in blocks along surfaces of displacement which tend to project upwards (fig. 1).

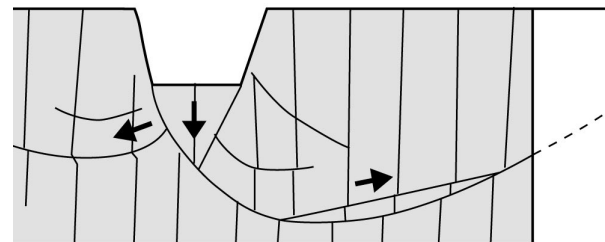


Figure 1. Sliding surfaces under descent of a pillar in compacted sand. Muhs, H. (1966), Pro. 6<sup>th</sup> I.G.S.M. and F.E., Vol. III, U. of Toronto Press.

**Readjustment:** During the decompression phase, these fault surfaces using planes of discontinuity (joints, old faults, etc.) are supposed to be used to reduce disequilibrium by a centripetal collapse, at depth, of terraces and ring graben affecting the surface rocks, and provoking the uplift, at centre, of deep-seated rocks, as has been observed in several astroblemes. In Charlevoix, if we admit that the excavation crater Da has a depth to diameter ratio of about 0,20 Da, the volume of the depth uplifted parautochthonous masses in the central part is similar to the volume of the collapsed masse outside. The degree of readjustment de-

depends upon the relative magnitude of the speed and the mass of the meteoroid, and the nature of the target rocks (fig. 2).

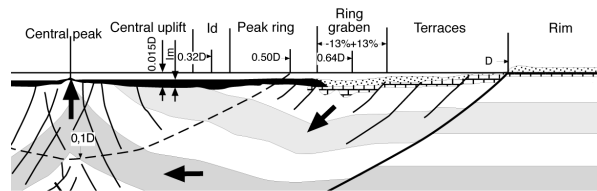
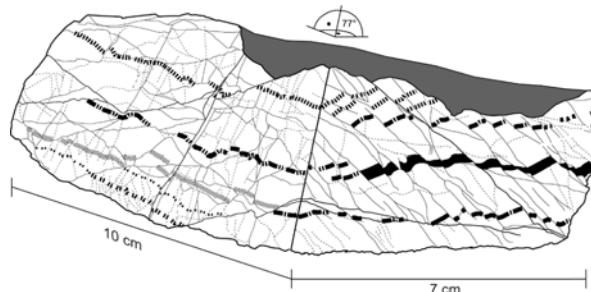


Figure 2. Schematic cross-sections for readjusted impact structures. Rondot, J. (2000), *Meteoritics & Planet. Sci.*, 35, 707-712.  $D$  = apparent diameter of the structure which is the basis of all measurements;  $0,5 D$  = diameter of the excavated crater (transient crater); dotted = allogenic breccia; bricks = preimpact sedimentary cover; stripes indicate hypothetical horizontal layers in the basement; dashed line represents the level of the excavated crater floor; Id = inner depression.

**STRUCTURAL INVESTIGATIONS IN THE CENTRAL UPLIFT OF THE UPHEAVAL DOME IMPACT CRATER, UTAH.** D. Scherler<sup>1</sup>, A. Jahn<sup>1</sup> and T. Kenkmann<sup>1</sup>. <sup>1</sup>Institut für Mineralogie, Museum für Naturkunde, Humboldt-Universität Berlin, Invalidenstrasse 43, D-10115 Berlin, Germany, dirk\_scherler@hotmail.com.

**Introduction:** The Upheaval Dome structure is a morphological expression of variously deformed sedimentary rocks in the otherwise relatively flat lying rocks of the Colorado Plateau in SE Utah. It has been identified to be an impact structure by early workers such as Shoemaker et al. in 1983 [1]. Even though Jackson et al. [2] proposed a concurring genetic theory of salt tectonics, geological [3] and geophysical [4] contributions as well as recent rock mechanical evidence [5] provides us with the impact-theory as the most favorable starting point for a kinematic model of the structure's genesis. Using geological and structural features, which were mapped during a field campaign in the innermost part, comprising of layered Triassic rocks (Chinle & Moenkopi formations), we generated a 3D-model using ArcGIS and the 3D-Analyst by ESRI. In addition to the mapping, several samples of the outcropping lithologies were taken to compare their microstructure with respect to those of undeformed samples in later work. By combining field observations with the visualization benefits of a 3D-model, important structural elements, their lateral development and relevance for uplifting material shall provide helpful insights on the formation of a central uplift in a layered target. The spatial distribution of the dipping strata, faults, folds and cataclastically deformed rocks were used for imposing constraints on the kinematics of central uplift formation during crater collapse. The work is in progress and displayed are the results so far. Further processing of the data shall result in a structure-map of marker horizons, the 3D-visualization of faults and eventually a balanced restoration of movements during crater collapse.

**Structure and Deformation:** The mapped units mainly consist of terrigenous clastic lithologies and are dominated by sand- and siltstones. Their deformational behavior range over a large scale though aren't everywhere visible due to distributed faulting and weathering. Close spaced fracturing is abundant over the entire structure and even though only small individual offsets (mm-cm) can be observed (Fig. 1), their accumulation might result in remarkably strain on a macroscale. On a dm- to m-scale, intraformational thrusting in a ramp-flat-geometry is common in stratified units such as the Jurassic Kayenta Formation or the Chinle and Moenkopi Formations. While concentric shortening, bound to reverse faults or folding, is well localized at the perimeter, the fault pattern gets more complex



**Fig. 1:** Blockview of Church Rock sample (Chinle Fm)

and diffuse towards the center. Anyhow, several major thrust faults are traceable from the margin of the mapped area towards the center and allow to distinguish blocks of relatively less internal deformation. Their radial arrangement [6], likewise reported from the Spider Impact Structure [7] in an iris-like fashion, appears to allow the accommodation of vertical displacement by stacking of inward flowing material. The amount of displacement increases centerward and is sometimes seen to develop from a radial striking fold, eventually indicating thrust direction by its vergency.

Clastic dikes [2,3] of different lithologies occur throughout the structure but concentrate in the center, where the White Rim Sandstone (Permian), as the lowermost outcropping unit, forms a complex dike network [7]. It's proximity to the overlying Hoskinnini Member suggests short transport distances. Other dike occurrences are generally smaller and the determination of their protoliths is future work, but can on first sight by means of color and mineralogy be restricted to high-porosity sandstones. In several locations, sandstones of various lithologies, though not displaced as dikes, display thickening with a massive appearance and the loss of sedimentary structures.

Rock masses within Wingate Sandstone (~100 m thick unit overlying the Triassic formations mentioned above) that outcrop at the perimeter of the inner depression appear to have undergone some ductile deformation similar to the dike rocks. Besides folding, due to convergent material flow, in some places the rock became displaced into the hanging wall unit with dike-like crosscutting relationships. The downward displacement of these rock masses apparently affected the internal geometry of the central uplift during its formation as seen from a normal fault overprint of a reverse fault structure.

**3D-Model and data processing:** The GIS-database (Fig. 2) consists of a DTM (A), polygons (e.g. outcropping units, B), lines (e.g. faults, C) and points (e.g. dips, D). The result is a DTM covered with geological signatures (E). Besides our own mapping of the innermost part, further information was taken from the works of [2] and [3].

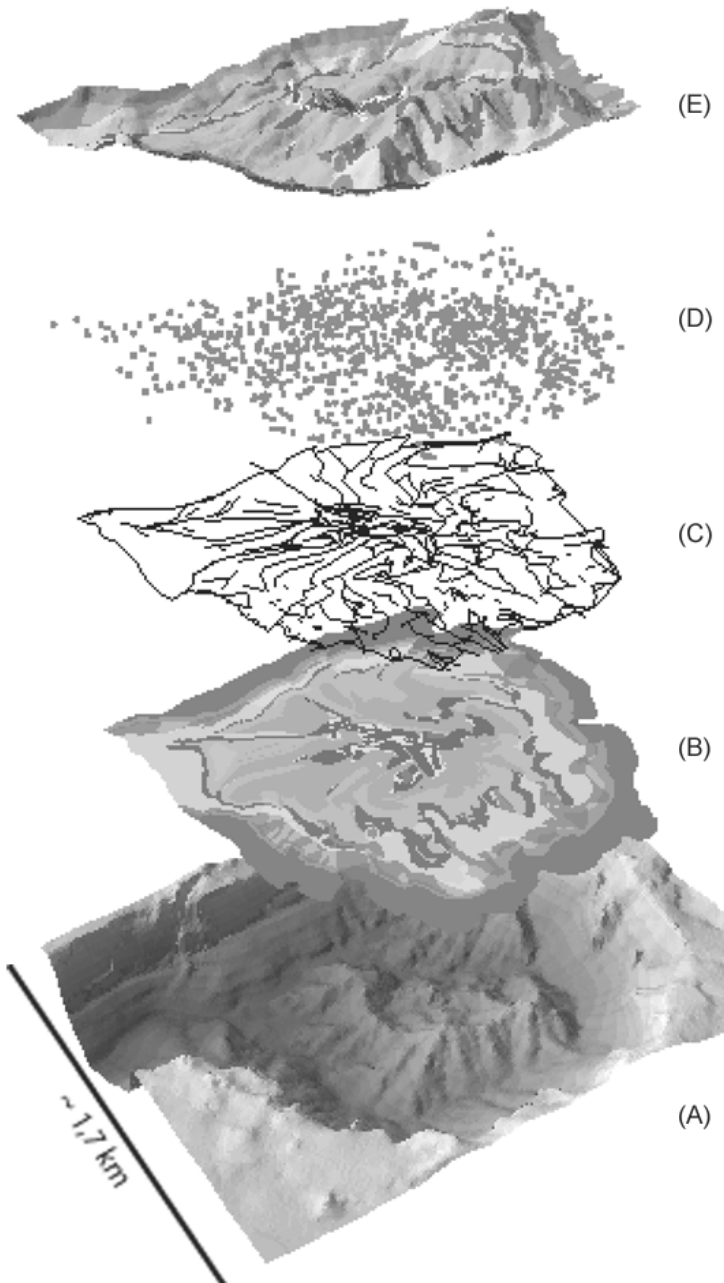


**Fig. 2:** Components of 3D-geological model.

Using spatial analytical tools, such as geostatistical interpolation for generating surface data from point information, we processed the data, generating thematic maps. Fig. 3 shows a dip-map (interpolation via kriging), that lines out the spatial variance of dip angles. Since the Kayenta Formation, just inside of the ring syncline, is a well stratified (and traceable) unit, distributed intraformational faulting, makes for strong varying dip-angles that reach high values, and results in thickening of the unit [6]. Even though a canyon cuts through the WNW' perimeter of the structure, there seems to be some symmetry with low dip-angle sectors in the WNW and ESE, since comparing dip-angles with topographic height showed no significant trend. This spatial variation might reflect an oblique impact scenario as proposed earlier [6], striking WNW-ESE.

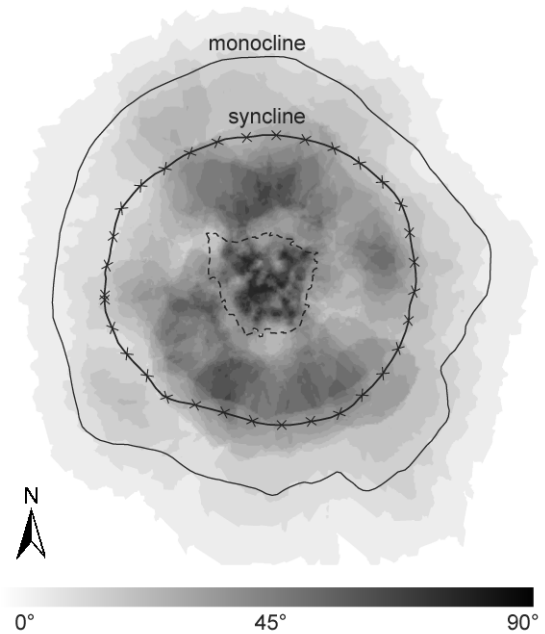


**Fig. 3:** Dip-map. Inner polygon is the mapped area.

**Acknowledgement:** This work is funded by the German Science Foundation (DFG), grant KE-732-6.

**References:**[1] Shoemaker, E. M., Herkenhoff, K. E. (1984) LPSC XV, 778-779. [2] Jackson, M. P. A. et al. (1998) GSA Bulletin, 110(12), 1547-1573. [3] Kriens, B. J. et al. (1999) JGR, 104(E8), 18,867-18,887. [4] Kanbur, Z. et al. (2000) JGR, 105(E5), 9489-9505. [5] Kenkmann, T. (2003) EPSL (submitted). [6] Kenkmann, T., Scherler, D. (2002) LPSC XXXIII, #1037. [7] Shoemaker, E. M., Shoemaker, C. S. (1996) AGSO J. Austr. Geol. & Geoph., 16(4), 379-398.

**COMPOSITION OF THE LATE INFLUX OF THE EARTH.** G. Schmidt<sup>1</sup>, <sup>1</sup>Institut für Kernchemie, Universität Mainz, Fritz-Straßmann-Weg 2, D-55099 Mainz, Germany, gschmidt@mail.kernchemie.uni-mainz.de.

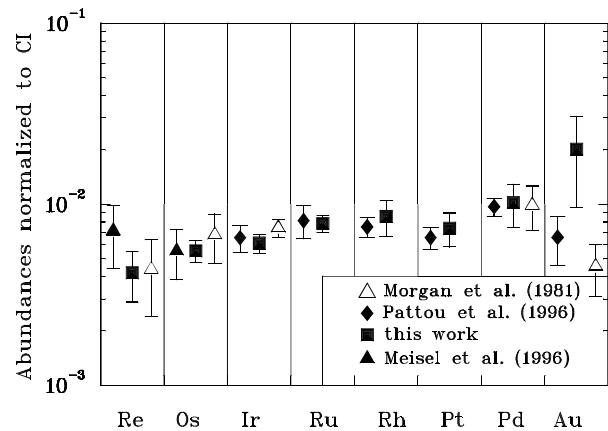
**Introduction:** Many authors explain the relative “high” abundances of HSE and their broadly chondritic proportions in the Earth’s mantle (PUM) by the addition of a late chondritic veneer after core formation. Many recent studies have documented significant regional variations in absolute HSE abundances and inter-element ratios in mantle samples. Such variations may have been caused by complex geochemical processes such as partial melting, melt percolation and aqueous metasomatism in the subcontinental lithosphere [1]. For a better characterisation of the late veneer component(s) of the Earth I review here selected neutron activation data from our own studies for orogenic spinel lherzolites [2,3] that have suffered only slight melt depletion ( $\text{Ca/Si} > 0.086$ ) and compare this data with selected data from the literature [4-6].

**Results:** Abundances of HSE in PUM sampled by lherzolites from our studies [2,3] are as follows;  $0.16 \pm 0.05$  ng/g Re;  $2.69 \pm 0.38$  ng/g Os,  $2.80 \pm 0.34$  ng/g Ir,  $5.60 \pm 0.61$  ng/g Ru,  $1.20 \pm 0.27$  ng/g Rh,  $7.33 \pm 1.55$  ng/g Pt,  $5.68 \pm 1.52$  ng/g Pd and  $3.06 \pm 1.60$  ng/g Au [7]. From a large number of mantle derived peridotites Morgan et al. [8] have found that Ir is normally distributed with a mean of  $3.2 \pm 0.2$  ng/g or  $(6.7 \pm 0.5) \times 10^{-3}$  CI. The worldwide distribution of Ir agrees reasonably well with the mean Ir value of  $2.80 \pm 0.34$  ng/g Ir estimated from our studies (TABLE 1).

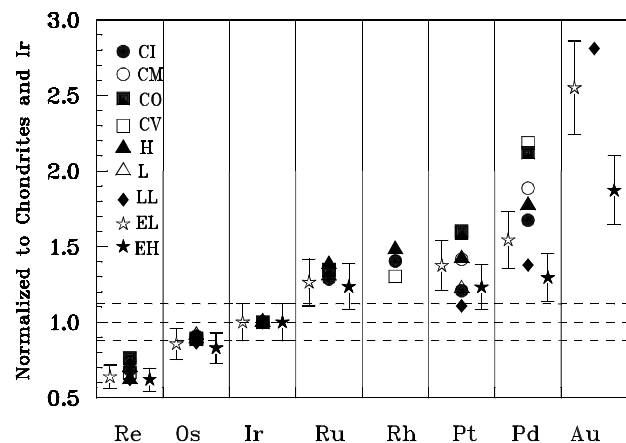
	Ca/Si	Re	Os	Ir	Ru	Rh	Pt	Pd	Au
		ng/g	ng/g	ng/g	ng/g	ng/g	ng/g	ng/g	ng/g
L92	0.098	0.10	3.35	3.52	6.61	1.31		7.80	1.93
L66	0.108	0.09	2.57	2.51	5.11	1.15		6.01	1.32
L732A	0.097	0.20	3.13	3.00	5.31	1.50		8.16	2.76
L79	0.086	0.15	3.23	3.18	6.53	1.26		6.99	1.68
ERN1/2	0.109	0.19	2.26	2.30	5.13	1.05	6.18	5.30	2.84
ERN1/4	0.102	0.17	2.56	2.72	5.56	0.87	6.53	4.11	2.96
ERN1/5	0.104	0.23	2.61	2.56	5.50	1.21	8.06	6.75	2.07
ERN2/16	0.113	0.10	2.47	2.40	4.71	1.14	8.32	4.73	6.38
ERN2/18	0.099	0.15	2.22	2.64	5.20	0.78	6.18	4.14	2.34
ERR3/3	0.090	0.17	2.86	3.02	6.19	1.31	10.90	6.43	3.34
ERS2/2	0.116	0.19	2.39	2.84	5.86	1.84	6.87	5.56	6.40
ERS2/4	0.087	0.12	2.93	3.00	6.17	1.14	6.38	3.05	3.32
ERSP4	0.103	0.20	2.34	2.70	4.98	1.04	6.58	4.81	2.41
Average		0.16	2.69	2.80	5.60	1.20	7.33	5.68	3.06
S.D.		0.05	0.38	0.34	0.61	0.27	1.55	1.52	1.60
S.D. (%)		29	14	12	11	22	21	27	52
CI		38.3	486	459	714	140	994	556	152
Mantle x 10 <sup>-3</sup> CI		4.1	5.5	6.1	7.8	8.6	7.4	10.2	20.1
S.D.		1.2	0.8	0.7	0.9	1.9	1.6	2.7	10.5

In a large number of „fertile“ samples [2-6] the abundance distribution of the HSE is remarkably uniform with slightly increasing abundances with decreasing

refractory character of the elements from Re to Pd, except Pt (FIG. 1).



In FIG. 2 mantle HSE abundances (this work) are plotted normalized to Ir and chondrites. The Pd/Ir-, Pt/Ir-, Ru/Ir- and Os/Ir inter-element ratios of E-chondrites agree reasonably well in comparison to the averaged mantle HSE abundances of the Earth’s upper mantle.



The HSE systematics show that the late veneer closely resembles E-chondrites or LL-chondrites [7,8].

**References:** [1] Schmidt G. et al. (2003) *Chem. Geol.*, 196, 77-105. [2] Lorand J.P. et al. (2000) *Lithos*, 53, 149-164. [3] Snow J.E. et al. (2000) *EPSL*, 175, 119-132. [4] Morgan J.W. et al. (1981) *Tectonophysics*, 75, 47-67. [5] Meisel T. et al. (1996) *Nature*, 383, 517-520. [6] Pattou L. et al. (1996) *Nature*, 379, 712-715. [7] Schmidt G. (2003) *Annual Report 2002, Institut für Kernchemie, IKMz 2003 - ISSN 0932-7622*. [8] Morgan J.W. et al. (2001) *Meteorit. Planet. Sci.*, 36, 1257-1275.

**THE ICDP DRILL CORE YAXCOPOIL-1, CHICXULUB IMPACT CRATER, MEXICO: SHOCK METAMORPHISM OF THE IMPACTITE UNITS (794 – 894 M).** R. T. Schmitt, A. Wittmann and D. Stöffler, Institute of Mineralogy, Museum of Natural History, Humboldt-University of Berlin, Invalidenstr. 43, D-10115 Berlin, Germany (e-mail: [ralf-thomas.schmitt@rz.hu-berlin.de](mailto:ralf-thomas.schmitt@rz.hu-berlin.de)).

**Introduction.** The ICDP drilling Yaxcopoil-1 (Yax-1) in a distance of ~60 km from the center of the Chicxulub impact crater, Mexico exposes 795 m of Tertiary sediments, 100 m of allochthonous suevite-like, melt rich breccias resting on 616 m of obviously displaced Cretaceous sediments, which are cut by several impact dike breccias [1, 2]. The suevitic sequence is composed of six units: (1) Upper sorted suevite (794.63 – 807.75 m), (2) lower sorted suevite (807.75 – 823.25 m), (3) upper suevite (823.25 – 846.09 m), (4) middle suevite (846.09 – 861.06 m), (5) brecciated melt rock (861.01 – 884.96 m), (6) lower suevite (884.96 – 894.94 m) [1]. In this study we focus on the shock metamorphism of these six impactite units.

**Methods.** Thin sections of the impactites from Yax-1 have been investigated for shock effects by optical microscopy, REM and Raman spectroscopy (DILOR LabRam, HeNe laser beam 632.8 nm, 50x lens). The shock classification of the components using the method described in [3]. Geochemical analysis were carried out by XRF analysis (SIEMENS SRS 3000) on glass tablets (0.6 g pulverized sample, 3.6 g Lithiumtetraborate) using international rock standards.

#### Results:

(1) *Shock metamorphism of silicates.* A description of the observed shock effects is given in [4]. Within all six impactite units more or less the same shock features within silicate grains or fragments are observed: (a) Quartz and feldspar of shock stage I display one or more sets of decorated PDFs (Fig. 1, 2). (b) Unaltered fragments of shock stages II (diaplectic quartz glass) and III (normal quartz or feldspar glass) are lacking. Therefore ballen quartz textures (Fig. 3) and checkerboard plagioclase are relatively frequent. (c) Melt fragments of shock stage IV are the dominating component within all impactite units. In most of the units at least two different types of silicate melt fragments occur. They are crystallized, in many cases indicate a possible exsolution of carbonate melts (droplet-like and/or dike-like shapes of calcite) and contain shocked and recrystallized crystalline fragments.

(2) *Search for high-pressure polymorphs of quartz.* The microscopic investigation of the thin sections do not show grains with diaplectic quartz glass, coesite or stishovite. Raman spectroscopy (samples Yax-1\_842.51 m and Yax-1\_894.26 m) on quartz grains with two sets of decorated PDFs display only Raman bands of  $\alpha$ -quartz (~206  $\text{cm}^{-1}$ , ~645  $\text{cm}^{-1}$ ), whereas

Raman bands of the high pressure polymorphs coesite or stishovite could not be detected yet. Ballen quartz aggregates of these two samples also display only Raman bands of  $\alpha$ -quartz.

(3) *Indications for carbonate melt in the lower suevite.* A carbonate agglomerate (Fig. 4, Tab. 1) from the top of the lower suevite (sample Yax-1\_884.92 m) was analyzed in detailed. In the top of the sample a grey non-porous limestone (Fig. 4, A) is in direct contact with crystallized silicate melt particles, recrystallized quartz grains and the matrix of the suevite. In some areas of the contact a replacement of crystallized silicate melt particles by the grey limestone is visible. Fragments of crystallized silicate melt particles could be observed within the grey limestone. The rims of these fragments are intensely corroded (Fig. 5). The grey limestone has a composition of  $\text{Ca}_{0.93}\text{Mg}_{0.07}(\text{CO}_3)$  (Tab. 1 A) and consists of calcite and rare dolomite grains. The second type of limestone in this sample is a porous, creamy colored limestone (Fig. 4, B) with a composition of  $\text{Ca}_{0.80}\text{Mg}_{0.20}(\text{CO}_3)$  (Tab. 1 B), which consists of Mg-calcite. This creamy colored limestone shows a fuzzy transition to the grey limestone and does not contain any fragments of silicate melt particles. Both types of limestone were cut by white, coarse grained calcite (Fig. 4, C). The petrographic observations within this agglomerate indicate, that the grey limestone may represent a carbonate melt.

**Discussion.** The full range of the progressive stages of shock metamorphism is observed in quartz and feldspar grains and lithic fragments of all six impactite layers, in particular PDFs in quartz and feldspar, recrystallized quartz and feldspar glass (ballen quartz and checkerboard plagioclase), and abundant whole rock melt particles. The intense (re)crystallization of mineral/rock and melt fragments indicates very high post-depositional temperatures and a strong post impact hydrothermal activity [5] which are typical processes accompanying melt-rich impactite units. In comparison to suevite deposits of smaller impact craters (e.g. Nördlinger Ries [6, 7]) the content of melt fragments within the Chicxulub suevites is much higher [8].

**Acknowledgment.** This work is supported by the Deutsche Forschungsgemeinschaft (DFG, Ke 732/8-2).

**References:** [1] Stöffler D. et al. (2003) *LPSC*, 34, Abstract #1553. [2] Wittmann, A. et al. (2003) *this volume*. [3] Stöffler D. (1971) *JGR*, 76, 5541-5551. [4] Schmitt R. T. et al. (2003) *LPSC*, 34, Abstract #1327.

- [5] Hecht L. et al. (2003) *LPSC*, 34, Abstract #1583.  
 [6] Stöffler D. et al. (1977) *Geologica Bavarica*, 77, 163-189. [7] Engelhardt v. W. (1997) *MAPS*, 32, 545-554. [8] Grieve R. F. A. et al. (1996) *MAPS*, 31, 6-35.

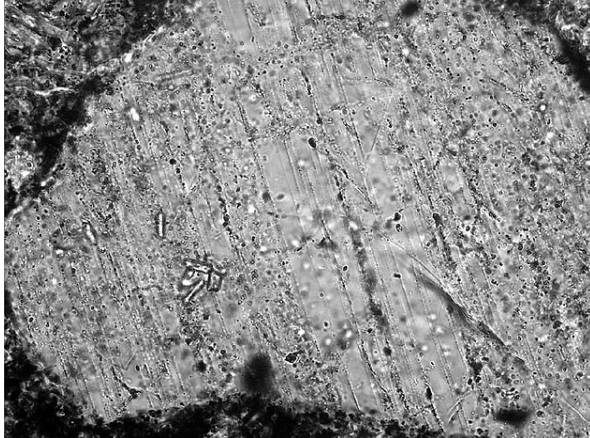


**Fig. 1:** Quartz grain with decorated planar deformation features from a melt particle, sample Yax-1\_865.01 m, thin section, plane polarized light, width 260  $\mu\text{m}$ .

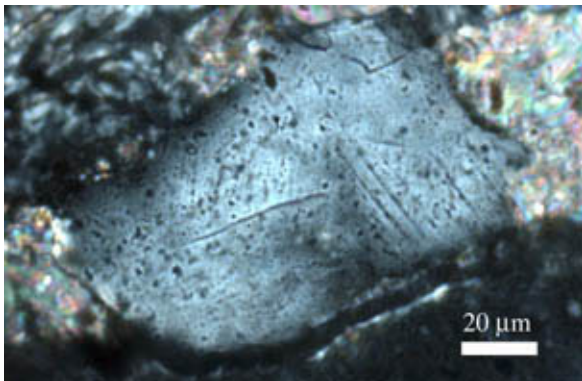


**Fig. 2:** Quartz grain with two sets of decorated planar deformation features, sample Yax-1\_894.26 m, thin section, crossed polars.

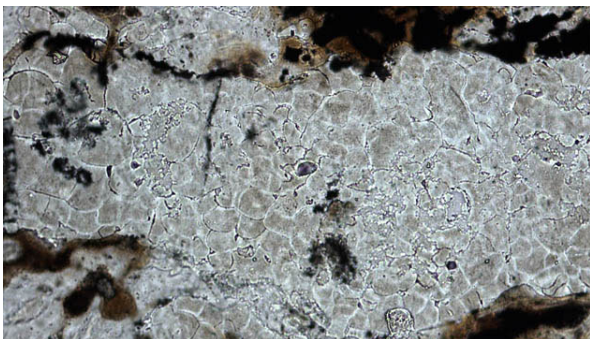


**Fig. 3:** Polycrystalline aggregate of ballen quartz, sample Yax- 1\_852.80 m, thin section, plane polarized light, width 570  $\mu\text{m}$ .

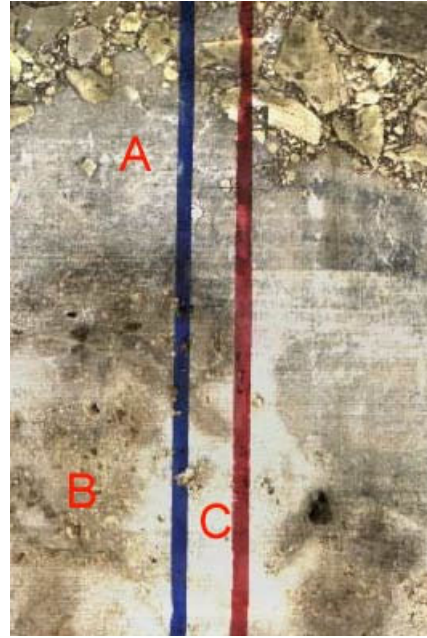


**Fig. 4:** Carbonate agglomerate at the top of the lower suevite (drill core scan, sample Yax-1\_884.92 m): (A) Grey non-porous limestone with some silicate melt fragments in contact to silicate melt particles and the matrix of the suevite. (B) Porous, creamy colored limestone with fuzzy transition to the grey limestone. (C) White, coarse grained calcite.

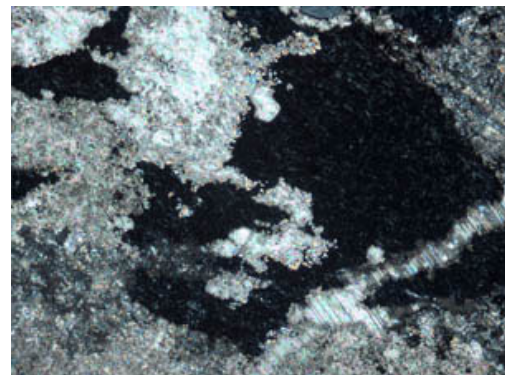


**Fig. 5:** Intensely corroded crystallized silicate melt particles (black) within the grey carbonate (Fig. 4, A), sample Yax-1\_884.92 m, thin section, crossed polars, width 570  $\mu\text{m}$ .

**Tab. 1:** Geochemical analysis of the two different limestones A and B of Fig. 4. Total Fe as  $\text{Fe}_2\text{O}_3$  and total S as  $\text{SO}_3$ .

weight%	A	B
$\text{SiO}_2$	0.5	0.5
$\text{TiO}_2$	<0.01	<0.01
$\text{Al}_2\text{O}_3$	<0.2	<0.2
$\text{Fe}_2\text{O}_3$	0.17	0.18
MnO	0.41	0.35
MgO	1.52	4.60
CaO	54.2	49.6
$\text{Na}_2\text{O}$	<0.02	0.06
$\text{K}_2\text{O}$	<0.02	<0.02
$\text{P}_2\text{O}_5$	0.01	0.01
$\text{SO}_3$	0.1	<0.1
LOI	43.0	44.3
total	99.91	99.60

**INTERNAL SHEARING AND SUBSURFACE EROSION FROM THE CHICXULUB EJECTA BLANKET (ALBION FM.), QUINTANA ROO, MEXICO.** F. Schönian<sup>1</sup>, T. Kenkmann<sup>1</sup> and D. Stöffler<sup>1</sup>, <sup>1</sup>Museum of Natural History, Humboldt-University of Berlin, Invalidenstr. 43, D-10115 Berlin, Germany, e-mail: frank.schoenian@museum.berlin.de.

**Introduction:** Processes leading to far-reaching ejecta outflows and ejecta blanket fluidization on planetary bodies with atmospheres and/or volatiles in the target (i.e. Venus, Mars, and Earth) are poorly understood because of the lack of field control. The Chicxulub ejecta blanket has been considered as a favourable study object for examining these processes because of its preservation by rapid post impact burial on a shallow marine platform. Ejecta material considered as part of the continuous ejecta blanket from the Chicxulub crater have first been described from Albion Island, Northern Belize, at a distance of 4 crater radii (354 km) from the proposed impact center [1,2]. In the Albion quarry the ejecta blanket is represented by a two-fold sequence of a basal spheroid bed, and the Albion diamictite, the ejecta blanket *sensu stricto* [1,2]. The Albion diamictite has been interpreted as a product of a secondary flow after ejecta curtain collapse and has been compared to fluidized ejecta blankets on Mars and Venus [2,3,4]. The flow has either been discussed of being a secondary turbulent/laminar debris flow [1] or a turbulent atmospheric flow produced by drag-induced ring vortices (ring vortex model, [2,5]). It is considered that most of the Albion Formation is composed of primary ejecta from Chicxulub [2] and ‘ablated’, polished and striated clasts are thought to represent high-altitude ballistic ejecta [6,7].

**Chicxulub ejecta blanket in Quintana Roo:** Detailed mapping revealed that west of the Laguna Bacalar / Rio Hondo fault zone the Chicxulub ejecta blanket is irregularly draping a karstified upper Cretaceous land surface, filling paleovalleys and overlying or surrounding hills of upper Cretaceous dolomites (Barton Creek / Sarabia Fm.). The ejecta blanket could be identified at localities within radial ranges of 295 to 365 km from the impact center. In the north (Caanlumil locality) the ejecta blanket is discordantly overlain by the Plio-Pleistocene Bacalar / Felipe Carillo Puerto Fm., whereas in the south it is overlain by the lower Tertiary (Eocene?) Estero Franco Fm. It is a very heterogeneous, chaotic carbonaceous breccia or diamictite with a high variability in particle roundness and shape, sorting, matrix composition, clast populations and internal structures. Its thickness is hardly to determine from the outcrops and is most likely highly variable as well. However, there are some general trends in composition and texture from north to south.

*Northern study area.* At the northern localities (295-300 km from the impact center) the matrix has a smaller carbonate content and contains less altered impact glasses (< 2%), components are less rounded and display only faint abrasion features. Only rarely larger boulders (> 50 cm) and no matrix-coated boulders were found. Irregular laminations are present, but no shear planes could be observed.

*Central study area.* In the central part (Chetumal area, 315-325 km from Chicxulub Pto.) the ejecta blanket is covering morphologically elevated upper Cretaceous dolomites (Campanian-Maastrichtian Sarabia Fm.), which are well exposed in the large Sarabia quarries. Carbonate content of the matrix rises significantly as well as the amount of altered impact glasses. Shear planes and shear breccias within the diamictite and at its base become abundant and the first large boulders of the upper Sarabia facies with sheared coatings can be observed. Clasts are more often abraded and some display facets and striations.

*Southern study area.* Farther south (Rio Hondo region, 330-350 km from the impact center) the upper Cretaceous paleorelief becomes more pronounced, in part with hills elevated above the ejecta blanket (Alvaro Obregon locality) and with paleovalleys filled with ejecta blanket material (Saxán and Palmar localities). Matrix composition is usually dolomitic, but highly variable. Linear, curved and in part highly chaotic shear planes or zones, often connected with polished and slickensided surfaces, sheared ejecta material, clay rich shear breccias or comminuted matrix material, become a major sedimentological feature. Clasts extracted from such shear zones display strong surface abrasion and striations. Large boulders (up to 12 m) of the lower Sarabia facies become abundant, some with sheared or laminated coatings.

The internal sedimentological structures can best be studied near Sabidos, where close to the upper contact with the Tertiary a major subhorizontal primary and numerous secondary shear planes are present as well as normal bedding planes, slumps and structures related to turbulent flow.

Strong erosion and shearing at the base is evident at Palmar/Ramonal, where an unsheared spheroid rich basal ejecta layer is filling a paleovalley, which towards S becomes heavily sheared around an obstacle of highly recrystallized and brecciated Upper Cretaceous dolomites. The latter display an undulating paleorelief

with evidence of erosion and displacement of topographic highs towards the S (brecciated and parautochthonous boulders).

Preliminary macroscopic observations on the clays enriched along shear planes or within shear breccias suggest that they are in part altered impact glasses and in part normal clays derived from erosion. Some shear breccias seem to consist mainly of altered impact glasses (melt), others are almost exclusively locally derived clays. In many cases a distinct layering between different types of shear breccias can be observed. Glasses were obviously still molten during emplacement as is evident from their shaped preferred orientation along shear zones.

A certain difficulty in studying the complex processes that acted during emplacement of the Albion diamictite are the poor outcrop quality due to strong tropical weathering and the scarcity of outcrops with respect to the large study area.

**Conclusions:** Field observations on sedimentological features of the Albion diamictite and their variability in a larger study area are leading to some new ideas regarding the processes that acted during final emplacement of the Chicxulub ejecta blanket on the southeastern Yucatán peninsula (c.f. [2,3]): The bulk ejecta material of the Albion diamictite moved as a ground-hugging flow of relatively high viscosity with transitions of laminar to turbulent flow and with strong frictional forces within and at the base of the flow. The flow regime and its variability was controlled by the pre-existing upper Cretaceous relief with stronger shearing above and around obstacles. The observations in Quintana Roo argue against atmospheric turbulences (ring vortices) and low viscosity (non-cohesive) debris flows as being responsible for the final ejecta emplacement.

The observed large run-out distance ( $> 4$  crater radii from the impact center) following initial ballistic emplacement (c.f. [8]) might be explained by a decrease of viscosity due to the high amount of molten material and the incorporation of locally derived clays. Both might have acted as lubricants in highly mobile shear zones.

The less sheared succession at Albion Island was most likely deposited within a paleodepression. This is consistent with the preservation of the spheroid bed and paleocaliche on the top of the Barton Creek Fm. [1,2,9]. However, the results suggest that many of the features observed at Albion Island and attributed to primary ejecta processes [2] are related to secondary erosion and internal shearing. These features include: the dolomitic matrix, the large boulders and the matrix-coated boulders (interpreted as 'accretionary blocks' [2]) and the abraded, faceted, striated and pitted (?)

clasts, thought to have been formed within the ejecta curtain [2,6,7]. Much of the ejecta blanket consists of material derived from erosion of the Cretaceous land surface. The two grain size populations observed at Albion Island [2] are probably the result of incorporation of locally eroded large boulders (2-8 m) within the flow.

The significance of erosion of local materials in the emplacement of the Albion Fm. suggests that over a wider area the Chicxulub ejecta blanket should display significant variations in composition reflecting the local Cretaceous bedrock lithologies. Polymict breccias with different lithological properties but similar internal structures are widely distributed over the Southern Yucatán Peninsula.

**References:** [1] Ocampo A. R. et al. (1996) In: Ryder G. et al. (Eds.), *Geol. Soc. Am., Special Paper*, 307, 75-88. [2] Pope K. O. et al. (1999) *EPSL*, 170, 351-364. [3] Pope K. O. and Ocampo A. C. (1999) *LPSC XXX*, Abstract #1380. [4] Kletetschka G. et al. (2001) *AGU Spring Meeting*, Abstract #P32A07K. [5] Barnouin-Jha O. S. and Schultz P. H. (1996) *J. Geophys. Res.*, 101; 21099-21115. [6] Pope K. O. and Ocampo A. C. (2000) *LPSC XXXI*, Abstract #1419 [7] Ocampo A. C. et al. (1997) *LPSC XXVIII*, #1861. [8] Oberbeck V. R. (1975) *Geophys. Space Phys.*, 13, 337-362. [9] Fouke B. W. et al. (2002) *Sedimentology*, 49(1), 117-138.

**Acknowledgements:** This project is funded by the graduate research program 'Evolutive Transformations and Mass Extinctions' of the German Science Foundation at the Museum of Natural History, Berlin, Germany (DFG, GRK 503, project A1).

**ADDITIONAL OBSERVATIONS ON THE IMPACT BRECCIAS OF THE CHICXULUB EJECTA BLANKET FROM THE UNAM-7 DRILL CORE, YUCATÁN, MEXICO.** F. Schönian<sup>1</sup>, T. Salge<sup>1</sup>, D. Stöffler<sup>1</sup> and J. Urrutia Fucugauchi<sup>3</sup>, <sup>1</sup>Museum of Natural History, Humboldt-University of Berlin, Invalidenstr. 43, D-10115 Berlin, Germany, <sup>3</sup>Instituto de Geofísica, UNAM, Mexico, e-mail: frank.schoenian@museum.berlin.de.

**Introduction:** In 1994/95 a shallow drilling program was carried out by the Universidad Nacional Autónoma de México (UNAM) within and around the Chicxulub crater. 7 drill cores were recovered (2800 m in total), only three of which encountered impact breccias (UNAM-5 at Santa Elena, 110 km S from center, UNAM-7 near Tekax, 125 km SE from center, UNAM-6 near Peto, 150 km SSE from the center, [1,2,3]). These breccias provide an excellent opportunity to compare the proximal Chicxulub ejecta with that of the well studied Ries crater in Germany.

In the Ries crater (24 km) two types of proximal ejecta facies are present. The continuous ejecta blanket consists of a lithic impact breccia without melt particles and rare clasts of deeper target lithologies [4]. This 'Bunte Breccia' is thought to have been deposited from the ejecta curtain by 'Ballistic Sedimentation' [4,5]. Close to the crater rim it is overlain with a sharp contact by a lithic breccia with melt particles ('Flaedle') and abundant basement clasts, the Suevite. The Suevite is believed to have been deposited by a collapse of the ejecta plume [5,6].

The breccias of the proximal Chicxulub ejecta blanket from the UNAM wells have been described as Suevite (UNAM-5 and upper breccia in UNAM-7) or as Bunte-Breccia-like deposit (UNAM-6 and lower breccia in UNAM-7, [2,3]). These two facies of the proximal ejecta blanket have been distinguished based on (a) abundance of basement versus evaporitic clasts and (b) variations in magnetic susceptibility [2,3]. The UNAM-6 and UNAM-7 drill cores still lack a detailed description. The UNAM-7 core is particularly interesting since it is thought to represent a Bunte Breccia / Suevite sequence similar to that of the Ries Crater. Recent observations on the UNAM-7 core and sample material require a revision of the original descriptions.

**Matrix properties:** Three principal matrix types of the impact breccias can be distinguished within the UNAM-7 core: (a) a usually poorly consolidated, greenish-grey, lithic matrix, (b) a poorly to well consolidated, greenish-yellowish-ocre vitreous or pelitic matrix, and (c) a well consolidated, greyish brown to dark brown carbonate-rich matrix. However, none of these types is exclusive, there are transitions between all of them (Fig. 2). In the upper part of the succession sometimes gradual sometimes abrupt changes from one to another type can be observed. Sometimes there is a complex interfingering of units or pockets of different

matrix types, displaying a inhomogeneous textures or breccia-in-breccia-type structures. In the lower part of the succession the matrix becomes more carbonaceous, homogeneous, and very well consolidated. Nevertheless, intercalations of lithic or vitreous, less consolidated breccias can still be observed.

**Basement clasts and melt fragments:** Basement clasts do preferentially occur in the upper breccia, mainly within lithic or vitreous matrix types. However, they are also present within the carbonate-rich matrix and down to the lower parts of the breccia succession. Basement clasts are subangular to subrounded and do often display 'reaction rims' or coatings of yellowish-green to greenish altered melt.

Melt fragments occur within all matrix types but are more abundant within the lithic and vitreous ones. In the upper and middle parts they are sometimes not clearly distinguishable from the matrix. They show different shapes and do not rarely contain lithic cores or clasts. There appear to be three distinct types of melt particles (alteration products?): a light-yellow / ocre to greenish, a green to greenish grey, and a dark green to brownish one. The most important observation is, that they occur in the entire succession down to its base (Fig. 1). However, the frequency and size of melt fragments decreases downwards. Matrix samples from the proposed 'Bunte Breccia' display melt fragments with lithic cores of anhydrite and carbonates.

**Sedimentary clasts:** There is an inverse relationship in abundance of sedimentary versus basement clasts. However, although more frequent in the lower succession, sedimentary clasts are abundant in the upper breccia as well. This applies for carbonate (dolomite and limestone) clast as well as for evaporitic (anhydrite and gypsum) clasts. Sedimentary clasts are usually less rounded. Carbonates are angular to subrounded and sometimes display a rim of altered impact glasses. Anhydrite clasts are generally angular to highly angular (Fig. 2) and do not show such rims. The size and frequency of anhydrite clasts increases within the lower breccia towards the bottom. 'Intercalations' or beds of anhydrite and marls have been reported from the lower part of the drill core [2,3]. These sediments show irregular or inclined contacts with the impact breccias and are internally strongly disturbed, in part brecciated. This favors an allochthonous interpretation as large clasts or boulders as supposed earlier [1].

**The contact ‘Bunte Breccia’/‘Suevite’:** The contact between the lower and the upper breccia unit is considered to be situated at 348.4 m [3] or 350.5 m [2] because of a significant drop in magnetic susceptibility within this interval. Lithologically, no sharp contact between the two distinct units can be observed. The transition between the highly variable upper and the more lower breccia is transitional and covers almost 5 core boxes (122-126, appr. 344 m – 358 m, Fig. 2).

**The basal contact:** In lithological columns the basal contact of the impact breccias was indicated at a depth of around 575 m [1,2,3]. However, massive brownish, carbonaceous, polymict impact breccias with abundant anhydrite clasts can be observed down to 680 m (Fig 1). The basal contact occurs >100 m deeper than proposed at around 681 m. This implies a total ejecta thickness of at least 459 m. The total depth of UNAM-7 is 702.4 m. The 21 m thick anhydrite/marl sequence in the lower part appears to be evenly horizontally bedded. It contains some minor dissolution breccias. However, anhydrite clasts within the overlying breccia unit show an apparent horizontal bedding as well. At present it is not clear if the UNAM-7 well bottomed out in upper Cretaceous bedrock or if this lower part represents another sedimentary megaclast.

**Discussion:** The two distinct breccia units of UNAM-7 could be confirmed within this report. However, they are lithologically very different from the Ries ejecta and cannot be described as a sequence of ‘Bunte Breccia’ and ‘Suevite’. Following the strict definition of impact lithologies [7] the complete succession should be defined as ‘Suevite’ (lithic impact breccia with melt particles). Nevertheless, a distinct, melt-rich upper unit can be defined, but with a more or less gradational contact to the underlying breccia unit. The high melt production in comparison to smaller craters like the Ries is consistent with scaling laws that predict an unproportionally increase of melt with increasing crater diameter [9]. Additionally, impact angle and atmospheric turbulences might have a significant effect on melt distribution within the ejecta blanket. A detailed description and analysis of the impact breccias of the UNAM wells and, if accessible, the PEMEX drill cores (T1, Y1, Y2, Y5a, and Y4) outside the Chicxulub crater would provide the opportunity to better understand the processes that acted during crater excavation and early stage ejecta emplacement.

**References:** [1] Urrutia Fucugauchi et al. (1996) *Geofísica Internacional*, 35(2), 125-133. [2] Urrutia Fucugauchi et al. (1996) *Geophys. Res. Lett.*, 23(13), 1565-1568. [3] Rebolledo Vieyra M. et al. (2000) *Int. Geol. Rev.*, 42(10), 948-978. [4] Hörz F. et al. (1983) *Rev. Geophys. Space Phys.*, 21, 1667-1725. [5] Oberbeck V. R. (1975) *Geophys. Space Phys.*, 13, 337-362.

[6] Von Engelhardt W. (1990), *Tectonophysics*, 171, 259-273. [7] Stöffler D. and Grieve R. A. F. (1994), *LPSC, XXV*, 1347-1348. [8] Melosh H. J. (1989), *Oxford Monogr. Geol. Geophys.*, 11, 245 p.

**Acknowledgements:** This work was supported by the graduate research program 503 of the German Science Foundation at the Museum of Natural History (DFG, GRK 503).

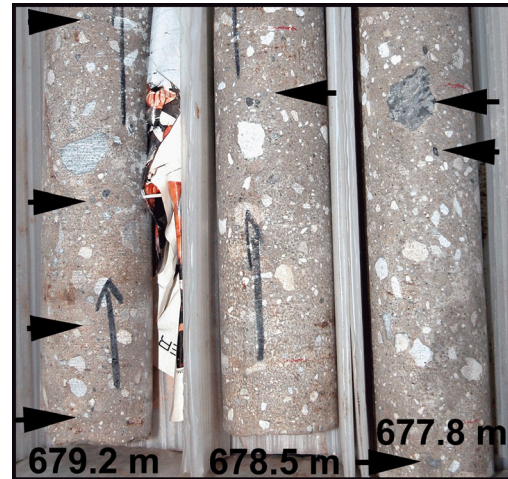


**Fig. 1:** Polymict impact breccia with carbonate-rich, brown matrix in the lower part of the breccia succession (box 219). Note the abundant greenish-grey melt fragments (only some of them are marked).

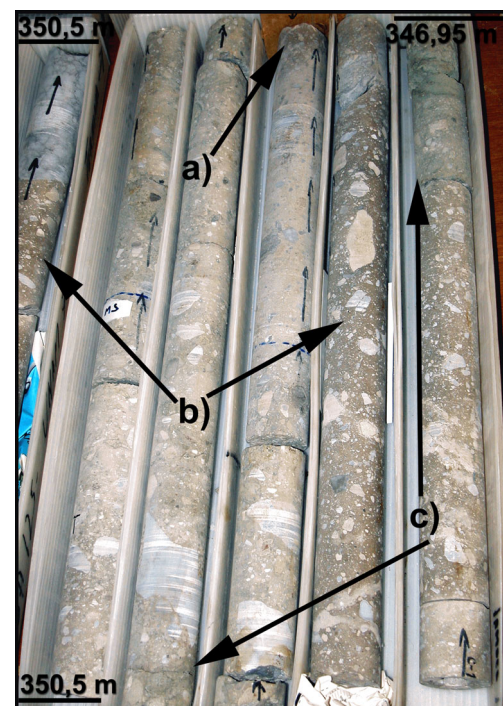


**Fig. 2:** Box 124 (346.95 m – 350.5 m). a) proposed contact of Bunte Breccia / Suevite (348.4 m). Note repetition of lithologies b) and c)

**“FINGERPRINTING” TARGET LITHOLOGIES OF THE CHICXULUB CRATER IN EJECTA FROM NE MEXICO AND TEXAS: YUCATAN SUBSURFACE REVISITED.** Peter Schulte<sup>1</sup>, Agnes Kontny<sup>2</sup>, and Wolfgang Stinnesbeck<sup>1</sup>, <sup>1</sup> Geologisches Institut, Universität Karlsruhe (TH), Kaiserstr. 12, D-76128 Karlsruhe, Germany (peter.schulte@bio-geo.uni-karlsruhe.de), <sup>2</sup> Geologisch-Paläontologisches Institut, Universität Heidelberg, Im Neuenheimer Feld 234, D-69120 Heidelberg, Germany.

**Introduction:** Microtektite- (“spherule”-) bearing proximal Chicxulub ejecta deposits from K-T sites in NE Mexico and Brazos, Texas, are a valuable tool to constrain original target lithologies at the Yucatán impact site, particular since the NE Gulf of Mexico region probably received ejecta from the northwestern, not yet drilled crater sector [1,2]. In addition, petrological characteristics of the ejecta may allow detailing ejection and dispersion processes [3].

**Locations:** The 0.2-1 m thick spherule deposits in NE Mexico are either embedded within upper Maastrichtian marls, often by soft-sediment deformation, or, more commonly, are present at the base of a multiple-debris flow sand-siltstone deposit, at, or close to, the K-T boundary [2]. At Brazos, Texas, a 20-cm thick graded spherule deposit, topped by cm-thick micritic limestone with thin interbedded sands, overlies upper Maastrichtian shales and underlies shales with very low fossil content and unclear age assignment, which in turn are overlain by early Danian calcareous shales.

**Material and methods:** Ejecta from the La Sierrita (LAS), El Peñon (EPO), and El Mimbral (MIM) outcrops in NE Mexico, and from a core (BRA) drilled close to the Brazos River K-T site in Texas, have been investigated by back-scattered electron (BSE) imaging, electron microprobe (EMP) analyses, cathodoluminescence, and magnetic susceptibility.

**Petrological characteristics:** Spherule deposits in Mexico and Texas comprise a chaotic, microbreccia-like fabric with a diverse suite of well preserved ejecta com-

ponents, usually mm-cm in size: vesiculated, globular spherules, angular to ribbon-like (ejecta-) fragments, carbonate clasts and globules, and 0.2-2 mm sized carbonaceous “lapilli” grains with accretionary features [3]. Ejecta components in NE Mexico also show welding and amalgamation, and often enclose other components, resulting in a foam-like texture. Additionally, ejecta particles are made of multiple compositional phases (Fig. 1) with textures indicative of either silicate-silicate or carbonate-silicate “liquid immiscibility”, and/or quenching from a melt (e.g., ‘feathery calcite’) [3].

**Mineralogical and geochemical phases:** Silicic ejecta phases from NE Mexico show a considerable compositional variability, though several “batches” can be distinguished that occur as distinct phases, even within individual ejecta particles (Table 1, Figs. 1, 2): (i) a FeO- (22-30 wt%), MgO- (8-14 wt%) rich phase with ~24-32 wt% SiO<sub>2</sub>, altered to dioctahedral chlorite, (ii) a FeO- (15-24 wt%), MgO- (10-18 wt%) rich phase with ~32-42 wt% SiO<sub>2</sub>, altered to di, trioctahedral chlorite, (iii) a K<sub>2</sub>O- (5-8 wt%) and Al<sub>2</sub>O<sub>3</sub>- (~30 wt%) rich hydrated glass with ~50 wt% SiO<sub>2</sub>. Besides in the latter K-rich phase, alkalis are generally <1 wt%. EMP analysis reveals that quenched carbonates are enriched in Fe and Mg (up to 1 wt%), they show also dark red-brown luminescence, in contrast to the bright luminescence colors of the carbonaceous matrix. Within spherules, hematite and goethite crystals, altered K-feldspar and pyroxene, dendritic or lamellar Ti-Fe oxides, and μm-sized, Co-, Ni-rich metallic and sulfidic phases are present. The magnetic susceptibility of the ejecta is

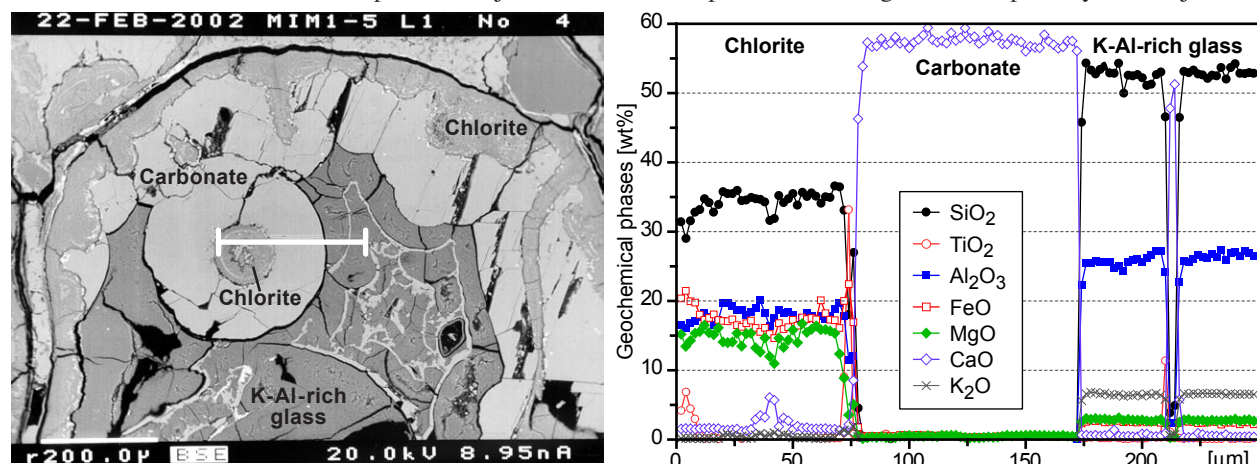


**Figure 1.** BSE photo and EMP linescan of a spherule from El Mimbral, illustrating the coexistence of different compositional phases (carbonate, chlorite, K-Al-rich glass). It also reveals petrologic characteristics related to the “liquid immiscibility” of ejecta phases (“tektite in tektite” texture), for instance carbonate veining, curved concave-convex menisci with sharp boundaries, or the distinct massive, “marble-like” texture of the carbonate inside the spherule.

elevated compared to the enclosing marls, and correlates with the iron content. Ejecta components from Texas are thoroughly altered and replaced by authigenetic high-Mg smectite ( $\text{SiO}_2 \sim 60$  wt%, 20 wt%  $\text{Al}_2\text{O}_3$ , 5 wt%  $\text{MgO}$ , alkalis <1wt%), and (rare) chlorite, which is similar in composition to (i) outlined above. Some spherules are also replaced by pyrite framboids.

**Conclusions:** Morphologically and compositionally similar microtektites have been found in K-T sites from the Western Interior to Central America, the Pacific, and the Atlantic. However, in contrast to the ejecta found in these K-T sites, which has been related to andesitic target rocks in Yucatán, the ejecta in NE Mexico and Texas is unusually heterogeneous in composition and, in NE Mexico, of prevalent mafic character. This may suggest highly localized ejecta compositions, incomplete mixing of target rocks, and different precursor lithologies including mafic rocks [e.g., amphibolite, 1], and rocks with substantial K and Al contents, albeit possible blending of melts from different rocks and/or fractionation effects make a clear evaluation difficult. Rare amphibolite fragments, and mafic rocks have been observed from within the Chicxulub crater [1,5,6], yet microkrystites and microspherules of mafic (pyroxene, K-feldspar), as well as of andesitic composition are a common constituent of the basal K-T boundary clay [e.g., in the Tethyan, 6,7]. Hence, our results may suggest the complex (local) interaction of proximal-distal ejection processes and, also, the findings of K-rich ejecta may constrain possible precursor phases

which acted as sources (?) to the intense alkali metasomatism in the Chicxulub crater breccia [8].

**Table 1:** Mineralogical formulae calculated stoichiometrically from representative EMP analyses of ejecta particles. Analysis MIM correspond to di, trioctahedral chlorites; EPO, LAS, and BRA1 reflect trioctahedral chlorites (all on basis of  $\text{O}_{10}(\text{OH})_8$ ); whereas BRA2 corresponds to Mg-rich smectites (on basis of  $\text{O}_{10}(\text{OH})_2$ ).

	MIM	EPO	LAS	BRA1	BRA2
	[# of cations per half structural unit cell]				
Si	3.69	2.74	2.82	3.43	3.93
Al(IV)	0.31	1.26	1.18	0.57	0.07
$\Sigma$ (Tetrahed.)	4.00	4.00	4.00	4.00	4.00
Al(VI)	1.68	1.32	1.31	1.65	1.66
Fe	1.39	2.96	3.53	2.00	0.04
Mg	1.93	1.64	0.89	1.73	0.41
Ti	0.14	0.01	0.04	0.03	0.02
$\Sigma$ (Octahed.)	5.15	5.93	5.77	5.41	2.12
Ca	0.06	0.03	0.13	0.01	0.01
K	0.09	0.01	0.04	0.03	0.08
$\Sigma$ (Interlayer)	0.15	0.04	0.16	0.04	0.10
Fe/(Fe+Mg)	0.42	0.64	0.80	0.54	0.09

**References:** [1] Kettrup, B. & Deutsch, A. (2003), *MAPS*, **38**, in press; [2] Schulte, P. et al. (2003), *IJEaS*, **92**, 114-142; [3] Graup, G. (1999) *MAPS*, **34**, 425-438 (1999); [4] Stöffler, D. et al. (2003), *LPS*, **34**, #1553; [5] Kring, D.A. et al. (2003) *LPS*, **34**, #1641; [6] Smit, J. et al. (1992) *LPI* **22**, 87-100; [7] Bauluz, B. (2000) *EPSL*, **182**, 127-136; [8] Hecht, R.T. et al. (2003) *LPS*, **34**, #1583.

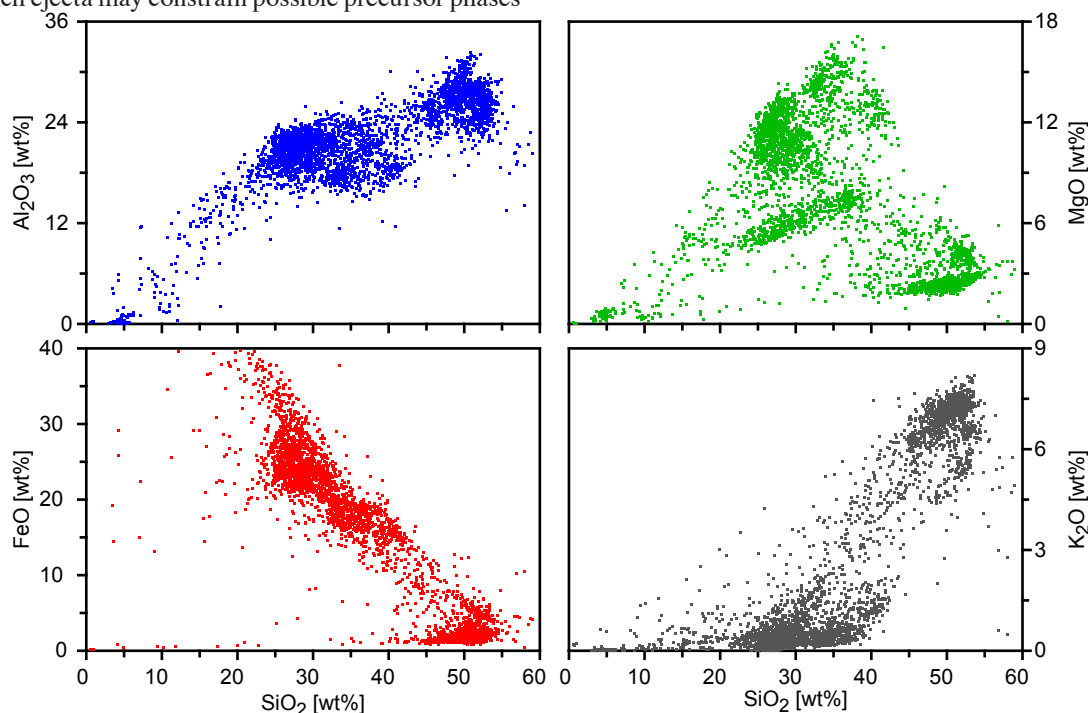


**Figure 2.** Oxide-correlation diagrams for Chicxulub ejecta from NE Mexico with results from individual EMP analyses ( $n = 3500$ , totals >80 wt%). Note the wide ranges in element abundance with several distinct compositional batches.

**AL-RICH ORTHOPYROXENES IN IMPACT MELT COATINGS OF GNEISS BOMBS FROM POPIGAI, RUSSIA – NEW ATEM DATA** A.-M. Seydoux-Guillaume<sup>1</sup>, A. Deutsch<sup>1</sup> and R. Wirth<sup>2</sup> <sup>1</sup>Univ. Münster, Inst. f. Planetologie, Wilhelm-Klemm-Str. 10, D-48149 Münster, Germany. <seydoux@uni-muenster.de>, <deutsca@uni-muenster.de>, <sup>2</sup>GeoForschungsZentrum-Potsdam, Div. 4, Telegrafenberg, 14473 Potsdam, Germany

**Introduction:** Popigai is an excellently preserved complex impact crater with a diameter of ~100 km [1,2]. In suevites and fine-grained fragmental breccias, numerous gneiss bombs, up to 40 cm across, occur. These gneiss bombs are coated with <3 cm thick layers of impact melt [1-4] which carry information about the time-temperature path that the bombs experienced between ejection and deposition as part of the allogenic breccias. The coatings consist of various melt layers, ranging from fresh, colorless to brownish, non-transparent crypto-crystalline glasses. Geochemical and Sr, Nd isotopic data of the coatings point to quite different precursor materials for the glass [4].

**Orthopyroxenes in the melt coatings – previous evidence.** In a preliminary TEM survey, [5] characterized the opx laths (Pbca - structure) in the melt coatings: the crystals display moderate densities of stacking faults and have an unusual composition. In particular exotic are high Al<sub>2</sub>O<sub>3</sub> contents. Crystallographic sites hosting the Al atoms could not be constrained by [5]. It was argued that either a complex Mg/Fe ↔ Al substitution, or Al atoms associated with the stacking faults may reasonable explain the data.

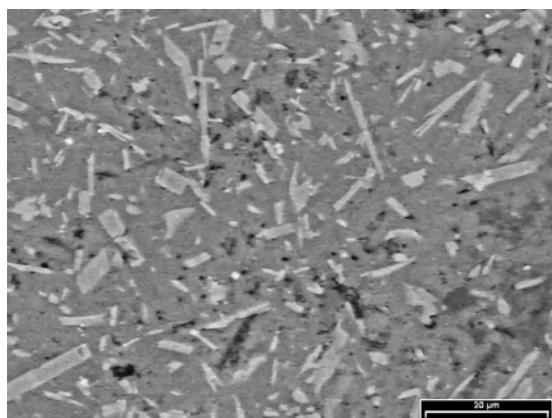


**Fig. 1.** SEM image of opx laths in a glassy matrix. Sample KD-1. Scale bar = 20 μm, picture by B.Kettrup.

**New data:** This ATEM study demonstrated that the Al<sub>2</sub>O<sub>3</sub> content is even higher than previously thought, clustering at ~ 9 wt.%, except in some domains (#1 and #8, Table 1) with still higher values ~ 13 wt.%. The Fe and Mg contents are quite heterogeneous. MgO ranges from 16 to 23 wt.%, and Fe from 15 to 26 wt.%. In summary, the composition is highly uncommon for orthopyroxenes [6]. We document that Al is distributed rather homogeneously throughout the crystal, making Al-rich inclusions of nm-sized phases rather unlikely;

yet we still can not exclude the presence of an annex phase (e.g., glassy inclusion) in the pyroxene.

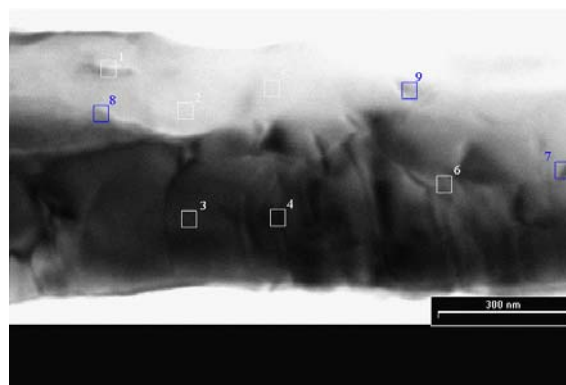


**Fig. 2.** BF-Scan TEM image of a pyroxene showing locations of some analysis given in Table 1. Sample KD-1.

**Table 1.** Chemical composition of a single crystal pyroxene (EDX-TEM point analysis, spot size ~30 nm). Sample KD-1

wt.%	#1	#3	#4	#6	#8	#9
SiO <sub>2</sub>	47,8	46,7	46,9	47,7	50,6	50,4
TiO <sub>2</sub>	0,9	0,8	0,7	0,9	0,5	0,8
Al <sub>2</sub> O <sub>3</sub>	<b>13,1</b>	9,3	8,8	8,2	<b>13,9</b>	7,8
Cr <sub>2</sub> O <sub>3</sub>	0,7	0,6	0,5	0,7	0,5	0,5
MgO	20,6	17,2	16,4	18,0	16,5	20,4
FeO <sup>TOT</sup>	15,5	24,5	26,0	23,8	16,6	19,3
CaO	1,0	0,6	0,5	0,5	0,8	0,7
K <sub>2</sub> O	0,6	0,2	0,2	0,2	0,7	0,2
total	100,2	99,9	100,0	100,0	100,1	100,1

Number corresponds to locations shown in Fig. 1.

**References:** [1] Masaitis V. L. (1998) *MAPS* 33, 349; [2] Deutsch A. et al. (2000) *Episodes* 23, 3-11, [3] Masaitis V.L., Deutsch A. (1999) *LPSC XXX*, Abstract #1237; [4] Kettrup B. et al. (2003) *Geochim. Cosmochim. Acta* 67, 733-750; [5] Kerschhofer L. et al. (2000) *LPSC XXXI*, Abstract #1360. [6] Prewitt C. T. (ed) (1980) *Pyroxenes. Rev. in Mineralogy* 7, Min. Soc. Am.

**Acknowledgments:** This work is supported by the Deutsche Forschungsgemeinschaft (DFG grant DE 401/18-1). We thank L. Kerschhofer, F. Langenhorst, and V. L. Masaitis for valuable discussion and comments.

## SHOCKED QUARTZ AT THE PERMIAN-TRIASSIC BOUNDARY (P/T) IN SPITI VALLEY, HIMALAYA, INDIA.

A. D. Shukla, N. Bhandari and P. N. Shukla, Physical Research Laboratory, Ahmedabad- 380 009, Gujarat, India.  
E-mail: anilds@prl.res.in.

The Permian -Triassic boundary (PTB, ~250 Ma) marks the transition of Paleozoic to Mesozoic. Several causative mechanisms involving terrestrial and extra-terrestrial processes have been advocated to explain physical and chemical anomalies found at this horizon. Short duration biological crisis (<10 – 165ky) [1-3 and references therein], anomalous  $^3\text{He}$  in fullerenes [3], planar deformation features in quartz [4] and sharp  $\delta^{13}\text{C}$  excursion [5, 6], anomalous  $\delta^{34}\text{S}$  [7] etc suggest sudden and catastrophic nature of this event.

In Spiti valley, the PTB is identified as a ferruginous band, sandwiched between Permian gray-black shale and Triassic limestone [1]. Earlier studies [1, 2 & 6] carried out on the same sedimentary sequences confirmed that records of geochemical and geological events such as global anoxia,  $\delta^{13}\text{C}$  excursion (both in organic and inorganic), as observed in worldwide P/T sections are present here. Anomalous europium enrichment reported from the Lalung section favors an iridium-poor and europium-rich impactor [2]. Recently we have also found nano-size iron oxy-

hydroxide phases similar to those observed at KTB and expected to originate in the impact vapour plume [8].

Here we report the presence of quartz grains with planar deformation features found in a thin section (Fig.1) in the ferruginous band from Attargoo (Lingti) section. In this section, the quartz grains are confined to two parallel bands (dark) embedded in phosphatic nodular groundmass (Ca & P). In Fig. 1b an enlarged backscatter image of a quartz grain is shown. The individual lamellae thickness varies between 3-6  $\mu\text{m}$  while the PDFs are <2-3 $\mu\text{m}$  thick, indicating a high degree (>10Gpa) of shock pressure, usually encountered in impact events [9]. Such features can not be related to Himalayan tectonism because there is no evidence of any metamorphism in the adjacent Permian shale as well as Triassic limestone horizons. Therefore, it is likely that these grains were incorporated in the ferruginous band as part of the ejecta after they were formed during an impact event. The presence of shocked quartz grains thus support a catastrophic event at the P/T boundary.

**References:** [1] Shukla A. D. et al. (2002) *Geol.Soc. Am. Sp. Paper*, 356, 445-453. [2] Bhandari N. et al. (1992) *GRL*, 19, 1531-1534. [3] Becker L. et al. (2001), *Science*, 291, 1530-1533. [4] Retallack G. J. et al. (1998) *Geology*, 26, 979-982. [5] Musashi M. et al. (2001) *Earth Planet. Sci. Lett.*, 191, 9-20. [6] Ghosh P. et al. (2002) *Current Science*, 83, 498-502. [7] Kaiho K. et al. (2001) *Geology*, 29, 815-819. [8] Verma H. C. et al. (2002) *Hyperfine Interactions*, 141/142, 357-360. [9] French B. M. (1998) *LPI Cont. No. 954*, 120pp.

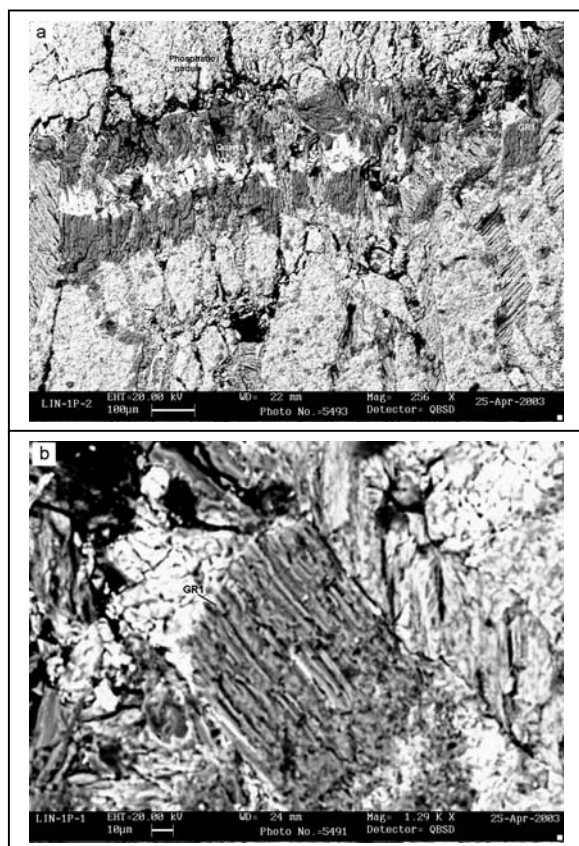


Fig.1. (a) A backscatter electron image of thin section of the ferruginous band material from the Attargoo section. PDF bearing quartz grains are confined to two dark bands; (b) Enlarged image of a quartz grain from the band showing PDFs.

**CRATERING PROCESS AFTER OBLIQUE IMPACTS.** V. V. Shuvalov, Institute for Dynamics of Geospheres RAS, Leninsky pr., 38, bld.1, Moscow, 119334, Russia, shuvalov@idg.chph.ras.ru

**Introduction:** It is well known that most impacts are oblique, and most craters are circular [1]. Nevertheless, there are several markers, which can indicate the obliquity of impacts, and even allow estimating an impact angle [2]. The main indication of the obliquity is ejecta distribution. The distal ejecta formed at the beginning of excavation stage is the most asymmetrical feature [3] and is commonly used to determine an impact angle and direction. However, the distal ejecta is also the most short-living feature (because of a small thickness of a layer of deposits) and often can not be used to estimate the obliquity.

Another possibilities to determine a value of trajectory angle and the direction of the projectile flight for craters resulting from oblique impacts have been discussed in several recent papers. Based on geological and geophysical observations and laboratory experiments, Schultz and Anderson [4] suggested to derive impact angle and direction from second order asymmetry of impact crater itself. They applied the following features: (1) maximum central uplift offset uprange from the geometrical center, (2) breached central peak complex parallel to the trajectory, (3) large central uplift diameter relative to crater diameter, (4) larger diameter transverse to the trajectory, (5) maximum structural rim uplift transverse to the trajectory, and (6) shallower than expected excavation. However, Ekholm and Melosh [5] using Magellan data investigated two of these most frequently used criteria, (1) and (3), in studies of terrestrial craters. They found the offset distribution to be random and very similar to that for near vertical impacts, and no correlation between central peak diameter and impact angle. Even less investigated is the influence of impact angle on internal structure (target deformation and material displacement) of the crater. Numerical modelling can be a good instrument to clarify these problems, allowing us to follow the process of central peak formation and its evolution in time.

The purpose of this paper is to study the cratering process after an oblique impact using direct numerical simulations. I consider impacts of 0.5-km- and 8-km-radius asteroids, which result in formation of complex craters with central peak (0.5 km) and peak ring (8 km). An angle of trajectory inclination varies from 30 to 90 degrees (with respect to horizon). Impact velocity is assumed to be 15 km/s.

**Numerical model.** A 3D version of the SOVA multi-material hydrocode is used to model all stages of cratering (penetration, excavation, and modification). To model material strength the approach developed by

Melosh and Ivanov [6] and O'Keefe and Ahrens [7] is used. It is based on the "rigid-plastic" model [8]. For fractured rocks (loose materials with finite cohesion), the yield strength was defined as by [9,10]

$$Y = \min(Y_0 + kP, Y_{max}), \quad (1)$$

where  $Y_0$  is the cohesion,  $k$  is the coefficient of dry friction,  $P$  is the pressure, and  $Y_{max}$  is the limiting yield strength of the material at high pressure. The mechanism of acoustic fluidization [1,11] is also taken into account.

**Results of simulations.** Fig.1 shows a sequence of snapshots illustrating the 45 degrees impact of a 8-km-radius dunite asteroid. 50 s after the impact all projectile material has escapes from the crater, and the crater reaches its maximum depth of about 30 km. The Moho boundary (between granite crust and dunite mantle) at a depth of 32 km is deformed by the cratering flow. The central high appears approximately 100 s after the impact and it is strongly offset in the uprange direction. However, the peak of the central high move downrange and already 150 s after the impact it becomes near symmetrical, however, its internal structure remains asymmetrical. The central high reaches its maximum height (approximately 20 km) at 200 s, then it descends and spreads along the crater floor transforming into peak ring. In the final crater the Moho boundary is only slightly disturbed, but the target material from a depth of 20-25 km rises to the surface in the process of central high growth.

In all cases under consideration the central high arising is offset in the uprange direction, where crater reaches it maximum depth earlier, whereas downward motion continues in the downrange part of the crater. Later a peak of the central high moves downrange and crater surface becomes more symmetrical, but its internal structure (shown by displacement of initially horizontal layers) is not symmetrical. A displacement of the central high downrange is explained by (1) a downrange motion and displacement of central high material and (2) by an increased late rise of the crater floor in the downrange part of the crater.

The final shape (a birds eyes view) of the crater is shown in Fig.2 for the same variant as shown in Fig.1.

**Discussion and conclusion.** The process of cratering can roughly be divided into three stages: compression/penetration, excavation, and modification [1]. In the case of oblique impacts the penetration stage is strongly asymmetrical, occurring with dimensions comparable to projectile size. The modification stage, in contrast, is close to symmetrical because the size of the final crater (i.e., characteristic size of modification process) is considerably larger

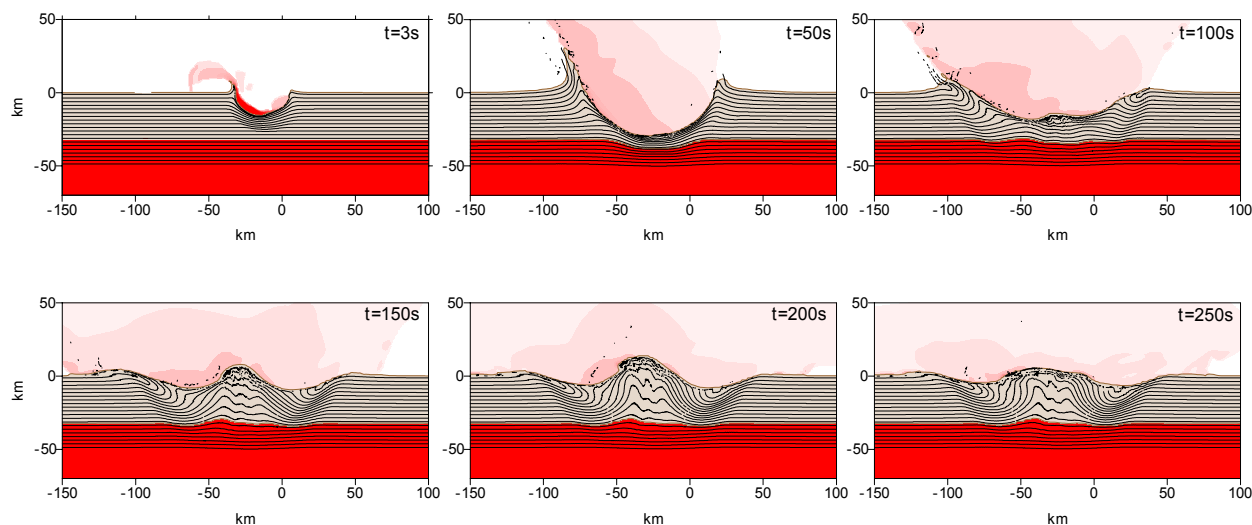


Fig.1. Impactor (red), crust (brown) and mantle (red) material distributions after a 45 degrees oblique impact of a 8-km-radius asteroid.

than the projectile size, and initial asymmetry attenuates at this distance. The excavation is an intermediate stage with early ejecta being strongly asymmetrical and late ejecta (forming crater rim) only slightly asymmetrical. Therefore we can divide all criteria of obliquity for three groups depending on governing processes. The distal ejecta, are formed at the beginning of the excavation (and the end of penetration) and its distribution is the most convincing criterion that is commonly used to determine an impact direction on other planets and satellites. The second group includes the crater rim, which is formed at the end of the excavation stage. All other criteria use second order asymmetry features formed during the modification (most symmetric) stage. Unfortunately spatial resolution is not high in these preliminary simulations and does not allow describing crater relief properly. Nevertheless the results show maximum structural rim uplift transverse to the trajectory,

shallower excavation, but do not show larger diameter transverse to the trajectory. Also the numerical results substantiate the conclusion of Ekholm and Melosh [5] that an uprange offset of the central uplift probably can not be used as a criterion of obliquity. Moreover, the numerical results are believed to explain the random distribution of the offset. At the beginning of modification a transient crater is still asymmetrical and the initial uplift is offset uprange. Thereafter it moves downrange, and then uprange again. The uplift may stop at different points in these quasi-oscillations, depending on target strength, degree of acoustic fluidization, etc. In other words this effect is comparable to those resulting from both average target strength and its local fluctuations. One more important conclusion is that internal crater structure is not symmetric.

**References:** [1] Melosh H. J. (1989) *Impact Cratering: A Geologic Process*, 245 pp. [2] Pierazzo E. and Melosh H. J. (2000) *Annu. Rev. Earth Planet Sci.*, 28, 141-167. [3] Gault D. E. and Wedekind J. A. (1978) *LPS IX*, 3843-3875. [4] Schultz P. H. and Anderson R. R. (1996) In *The Manson Impact Structure, Iowa: Anatomy of an Impact Crater*, *GSA Special Paper 302*, 397-417. [5] Ekholm A. G. and Melosh J. H. (2001) *Geoph. Res. Lett.*, 28, 4, 623-626. [6] Melosh H. J. and Ivanov B. A. (1999) *Annu. Rev. of Earth and Planet. Sci.*, 27, 385-425. [7] O'Keefe J. D. and Ahrens T. J. (1999) *JGR*, 104, 27,091-27,104. [8] Dienes J. K. and Walsh J. M. (1970) In *High-Velocity Impact Phenomena* (ed. R. Kinslow), pp.46-104. [9] Lundborg N. (1968) *Int. J. Rock. Mech. and Mining Sci.*, 5, 427-454. [10] Zamyshliaev B. V. and Evtrev L. S. (1990) *Models of Dynamic Deforming and Failure for Ground Media*. 215 pp., in Russian. [11] Ivanov B. A. and Turtle E. P. (2001) *LPS XXXII*, Abstract #1284.

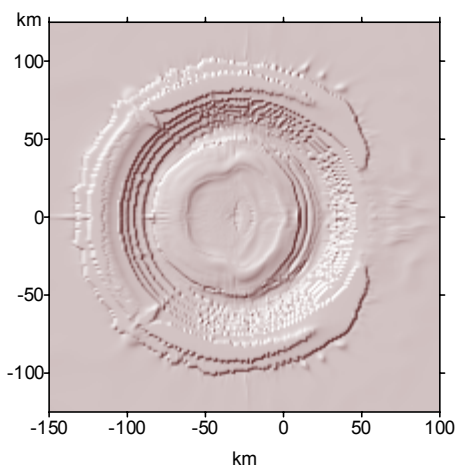


Fig.2. Final shape of the crater shown in Fig.1.

**MECHANISMS OF TSUNAMI GENERATION BY IMPACTS.** V.V. Shuvalov, Institute for Dynamics of Geospheres RAS, Leninsky pr. 38-1, 119334 Moscow, Russia, e-mail: shuvalov@idg.chph.ras.ru.

**Introduction.** At present, tsunami waves are considered as one of the main shock factors in the problem of asteroid hazards [1]. In the analysis of the consequences of tsunami arising on the marine impact of cosmic bodies, the following formula is commonly used [2]

$$h = 45 \frac{H}{L} (Y)^{0.25},$$

where  $H$  is the water basin depth,  $h$  is the wave amplitude in meters,  $L$  is the distance from the source, and  $Y$  is the released energy in kilotons TNT equivalent. This formula was derived from the analysis of data obtained at the Baker nuclear explosion in the 60-m deep lagoon on Bikini atoll; its energy was about 20 kt [2].

However, the existing results of experimental and theoretical studies show that the cratering process in marine targets and a mechanism of tsunami formation strongly depends on the parameter  $d/H$ , where  $d$  is the impactor diameter and  $H$  is the sea depth. When  $d/H < 0.1$ , no underwater crater is formed at all [3], and tsunami wave results from the collapse of water transient cavity. When  $d > H$ , the water column has almost no effect on the crater-forming flow [4] and tsunami wave is formed due to the expulsion of water by the rim of the crater that grows in the soil and by the uplift of the sea floor in the cratering flow process. The most complicated flow arises in the intermediate case when  $0.1 < d/H < 1$ .

Recently Melosh [5] has concluded that tsunami created by asteroids  $< 1$  km in diameter could not cause strong devastation to coastal areas. His conclusions are based on the report of the US Office of Naval Research [6] summarising the results obtained for tsunami generated by nuclear explosions in the ocean. According to this report waves with periods in the range of 20 to 100 s are expected to break on the outer continental shelf and tsunami with little onshore damage (contrary to tsunami with periods of 100 s to 1 hour generated by earth quakes). This means that in order to estimate a risk from impact generated tsunami we should also calculate a period of these waves.

In this study I analyze these three regimes of underwater crater formation and tsunami generation by means of numerical modelling of the three terrestrial marine target impacts: Eltanin, Lockne, and Mjølñir. These impact structures are well studied and characterize the typical regimes of crater formation at

different ratios of impactor diameter to the sea depth:  $d/H = 0.25$  for Eltanin,  $d/H = 4$  for Mjølñir, and  $d/H = 1$  for Lockne.

**Numerical model.** The SOVA multi-dimensional multi-material hydrocode [7] is used to simulate main stages of the impact (the impactor penetration into the target, the crater-forming flow, the filling of the crater with water, the generation of tsunami waves).

To calculate the thermodynamic parameters of air, water, and soil the tabular equation of state for air [8], the Tillotson equation of state [9], and the tables obtained by the ANEOS code [10] are employed.

The model of strength developed by Melosh and Ivanov [11] and the algorithm for taking "acoustic fluidization" into account were included into the SOVA code in order to simulate the crater modification.

**Eltanin.** Eltanin [12] is the only presently known impact structure formed during the fall of a cosmic body into a deep (4–5 km) oceanic basin. According to the estimates made by Gersonde and Kyte [13], the impact structure of Eltanin was formed on impact of an asteroid 0.5–2 km in size that occurred 2.2 Myr ago. No traces of the underwater crater have been discovered.

Numerical simulations of a vertical impact of a 1-km-diameter asteroid show that approximately at 30 s after the impact a transient water cavity 15 km in diameter is formed. Its collapse produces tsunami waves with amplitudes 1200, 800, 450, and 320 m at distances 20, 30, 50, and 70 km from the impact point. Formula (1) gives the wave amplitudes 850, 570, 340, and 240 m at the same distances. Since the difference does not exceed 30% the agreement can be considered as satisfactory. A period of the tsunami waves is about 150 s. This correlates well with

**Mjølñir.** According to Dypvik et al. [14], the 40-km-diameter Mjølñir crater in the Barents Sea is a result of the impact of an asteroid that occurred 140 Myr ago. The estimated diameter of the asteroid is 1–3 km; the probable depth of the sea was 300–500 m. In this case the water layer is very thin in comparison with crater depth, it very slightly influences the cratering flow. The rim of the growing crater pushes the sea water outward and upward, thereby generating a water surge. This surge moves from the center ahead of the crater wall and the excavated-material cone. The height of the water surge increases first, and then the surge collapses, breaking down into several waves. The interaction between these waves results in a tsunami.

For the energy 250 Gtons of TNT equivalent released at the formation of the Mjølner crater, the formula of Glasstone and Dolan gives an amplitude of about 40 m at a distance of about 60 km from the crater center. This value is significantly lower than that obtained in our simulations (about 200 m). The reason of this discrepancy is another mechanism of tsunami generation. Both in the Eltanin and Bikini test tsunami wave was a result of transient water crater evolution and collapse. In the Mjølner case tsunami is generated by the motion of solid material. In some sense it is more similar to landslides induced tsunami when the wave is generated due to motion of solid surfaces. As a result we have another energy-amplitude dependence. We also have a much large period of the waves – about 1000 s.

**Lockne.** The age of the underwater crater Lockne located in Sweden is estimated to be approximately 450 Myr [15]. Presumably, this crater is the result of the fall of an asteroid into the sea with a depth ranging from 200 to 1000 m. More exact estimate is 500–700 m [16]. Numerical simulations for depths 200, 500, and 1000 m show a gradual transition from a Mjølner-like to an Eltanin-like mechanism of tsunami generation. Modification of basement crater and its infilling by water makes the flow much more complicated. In both last cases (Lockne and Mjølner) similar to earthquake generated tsunami a net volume of water (negative) is transported across a large area of the ocean. The net volume appears due to formation of basement crater. This effect increases a period of the wave.

**Asymmetry of tsunami waves produced by oblique impacts.** The process of cratering can roughly be divided into three stages: compression/penetration, excavation, and modification [17]. In the case of oblique impacts the penetration is strongly asymmetrical, occurring at distances comparable to projectile size. The modification stage, in contrast, is close to symmetrical because the size of the final crater (i.e., characteristic size of modification process) is considerably larger than the projectile size, and initial asymmetry attenuates at high distance. It is comparable to a high energy explosion, where shock wave propagation and cratering depend on the energy release only. The excavation is an intermediate stage with early ejecta being strongly asymmetrical and late ejecta (forming crater rim) only slightly asymmetrical.

Therefore we can expect that all effects produced during the penetration and early excavation stage should be asymmetric (for example distal ejecta) and all phenomena generated during the modification stage should be near symmetric (all craters are near circular). Tsunami waves form during the late modification stage and we should not expect strong asymmetry. Of

course, this concerns only moderately oblique impacts (with angles exceeding 20-30 degrees to horizon). Grazing impacts can probably produce strongly asymmetric waves. Numerical simulations confirm this conclusion.

**Conclusions.** There are two mechanisms of tsunami-wave generation by marine target impacts: If the sea depth exceeds the impactor diameter by a factor of 2-4 or more, tsunamis are generated at the infilling of the transient water crater, and the wave amplitude can be estimated using the formulas derived for underwater nuclear explosions. If the impactor size is larger than the sea depth, tsunamis are formed due to the expulsion of water by the rim of the crater that grows in the soil and by the uplift of the sea floor in the cratering flow process. In this case, the wave amplitude and period can be several times larger than that estimated by the formulas for nuclear explosions.

And in the intermediate case we have even more complicated mechanism of tsunami formation. And one more conclusion: a use of any simplified formulas for the initial shape velocity distributions can lead to strong errors in determination of tsunami energy and amplitude.

Oblique impacts produce almost symmetrical tsunami wave.

**References:** [1] Adushkin V.V. and Nemchinov I.V. (1994) *Hazards due to Comets and Asteroids* (Ed. T.Gehrels), 721-778. [2] Glasstone S. and Dolan P.J. (1977) *The effects of nuclear weapons*, 653 p. [3] Gault D.E. and Ch.P. Sonett (1982) *GSA Special Paper*, 190, 69-92. [4] Shuvalov V. et al. (2002) *JGR*, 10.1029/2001JE001698, 1-1-1-12. [5] Melosh H.J. (2003) *LPSC XXXIV*, #2013. [6] Van Dorn et al. (1968) *Handbook of explosion-generated water waves*. [7] Shuvalov V.V. (1999) *Shock Waves*, 9(6), 381-390. [8] Kuznetsov N.M. (1965) *Thermodynamic Functions and Shock Adiabats for air at High Temperatures*, 464 p., (in Russian) [9] Tillotson J.H. (1962) *General Atomic Rep. GA-3216*, 137p. [10] Thompson S.L. and Lauson H.S. (1972) *Rep. SC-RR-71 0714*, 119 pp., Sandia National Lab. [11] Melosh H.J. and Ivanov B.A. (1999) *Annu. Rev. Earth Planet. Sci.*, 27, 385–425. [12] Gersonde R. et al. (1997) *Nature*, 390, 357-363. [13] Gersonde R. and Kyte F. T. (2001) *Meteoritics & Planet. Sci.*, 36, Supplement, p.A64. [14] Dypvik H. et al. (1996) *Geology*, 24, 779–782. [15] Ormö J. and Lindström M. (2000) *Geol. Mag.*, 137(1), 67–80. [16] Ormö J. et al. (2002) *JGR*, 107, 3-1-3-9. [17] Melosh H.J. (1989) *Impact Cratering: A Geologic Process*, 245 pp.

**EXPERIMENTALLY SHOCK-LOADED ANHYDRITE: UNIT-CELL DIMENSIONS, MICROSTRAIN AND DOMAIN SIZE FROM X-RAY DIFFRACTION.** R. Skála<sup>1</sup> and F. Hörz<sup>2</sup>, <sup>1</sup>Czech Geological Survey, Klárov 3/131, CZ-118 21 Praha 1, Czech Republic, skala@cgu.cz, <sup>2</sup>NASA-JSC, SN-2, Houston, Texas 77058, USA.

**Introduction:** Cretaceous/Tertiary (K/T) boundary is traditionally associated with one of the most dramatic mass extinctions in the Earth history. A number of killing mechanisms have been suggested to contribute to the widespread extinctions of Cretaceous biota at this boundary, including severe, global deterioration of the atmosphere and hydrosphere from the shock-induced release of CO<sub>2</sub> and SO<sub>x</sub> from carbonate- and sulfate-bearing target rocks, respectively [1-9]. Recently carried out calculations revealed that the global warming caused by CO<sub>2</sub> release was considerably less important than the cooling due to SO<sub>x</sub> gases release during the Chicxulub impact event [10]. Considering apparent potential importance of the response of sulfates to the shock metamorphism, relative lack of the data on shock behavior of sulfates as well as some general difficulties encountered during thermodynamic modeling of the shock-induced CO<sub>2</sub> loss from carbonates [11, 12] we subjected anhydrite to a series of shock experiments designed for complete recovery of the shocked material. We report here on the detail X-ray diffraction analysis of seven samples that were subjected to experimental shock-loading from 10 to 65 GPa.

**Experimental:** The shock-recovery experiments employed a 20-mm-caliber powder propellant gun at the NASA JSC, Houston, as detailed in e.g. [13]. Double-polished disks (diameter 7.3 mm, thickness 1.0 or 0.7 mm) of polycrystalline, massive anhydrite from Bees, Canton Vaud/Waadts, Switzerland, were encased in metal target holders (aluminum, stainless steel, W-alloy, and pure W) and impacted by metal flyer plates (also made from these metals). Peak shock pressures achieved by multiple shock wave reverberations were obtained with a graphical impedance match method [14] using the equations of state of [15] and the actual

impact velocity measured via IR laser occultation methods. Details on the experiments are given in Table 1. Powder X-ray diffraction patterns were acquired at the Bayerisches Geoinstitut (BGI), Bayreuth, using the diffractometer STOE in the transmission geometry, and at the Dip. Scienze della Terra, University of Siena, Siena, using a Philips diffractometer in the reflecting geometry. The former experimental setup uses CoK<sub>α1</sub> radiation, the latter one employs CuK<sub>α</sub> radiation. In the transmission geometry, silicon was used as an internal standard while LaB<sub>6</sub> was utilized as an external standard in the case of the reflecting geometry. Qualitative phase analysis employed the Bede Search/Match software and a PDF2 database (1998 release). Unit cell dimensions were refined using the program UnitCell [16] from the individual peak positions yielded with program XFit [17]. Domain size and microstrain were evaluated with both fundamental approach to modeling of peak shapes as implemented in XFit [17] and the whole powder pattern fitting techniques with pre-defined instrumental resolution function as implemented in FullProf [18].

**Results:** Samples recovered from the metal containers are pervasively fractured and disintegrate easily. Optical microscopy confirmed macroscopic observations and revealed that samples are strongly fragmented. All XRD patterns yield anhydrite only and no extra peaks due to other phase(s) have been observed. The unit-cell dimensions, refined from the positions of ten most prominent not overlapping diffraction lines in patterns taken in the transmission geometry (with *hkl* indices: 111, 102, 220, 122, 031, 013, 302, 322, 142, and 224), do not display any systematic correlation with the pressure; maximum differences are less than 0.1 rel. % (Fig. 1). Line broadening, however, is prominent already at 10 GPa and increases systematic-

**Table 1.** Experimental conditions for the shock recovery experiments on anhydrite. Impact velocity ( $v_i$ ), initial shock pressure in the sample ( $P_1$ ), number of reverberations, and final peak shock pressure in the sample ( $P_{sample}$ ) and its duration are given.

Shot #	Flyer plate material	Container material	$v_i$ (km/s)	$P_1$ (GPa)	number of reverberations	$P_{sample}$ (GPa)	peak pressure pulse ( $\mu$ s)
3283	Al2024	Al2024	1.212	9.34	5	10.39	0.02
3284	Al2024	SS304	1.533	12.38	4	19.65	0.08
3327	SS304	SS304	1.245	13.70	4	33.44	0.10
3287	FS77	FS77	1.240	16.19	3	40.20	0.05
3289	W	FS77	1.415	19.77	3	49.78	0.03
3336	W	SS304	1.448	20.38	5	60.82	0.04
3342	W	SS304	1.517	21.65	5	64.39	0.03

cally with pressure, albeit not linearly, up to 40 GPa. Above this limit the broadening decreases slightly. Simultaneously, the peak height decreases and is some 50 % of that for standard sample at the pressure of 10 GPa; from this point on, peak heights remain invariant

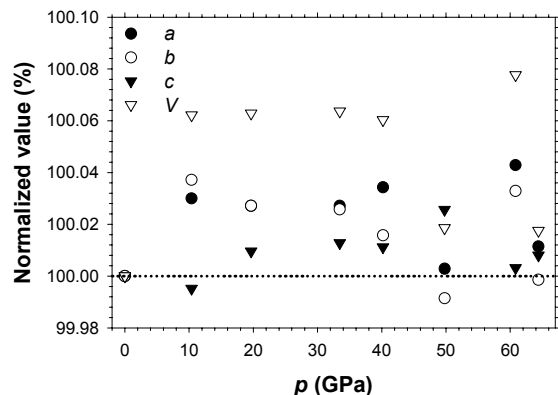


**Fig. 1.** Unit cell dimensions of experimentally shock-loaded anhydrite.

within experimental errors. Domain size and microstrain, which are known to depend on peak shapes [19], tightly copy trends for peak widths and heights, respectively (Fig. 2).

**Conclusions:** The results of our X-ray diffraction study show, contrary to [5] who found incipient vaporization of anhydrite to require *ca* 32 GPa, that an-

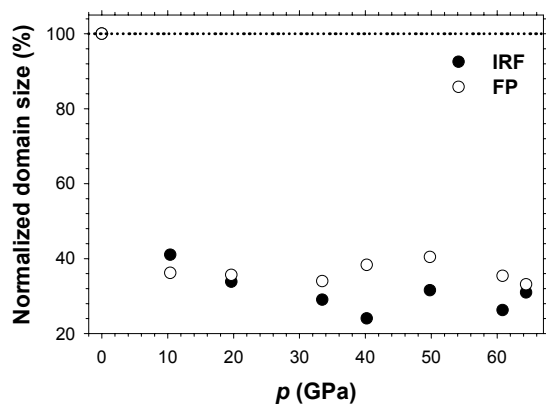


**Fig. 2.** Domain size for the shocked anhydrite calculated with whole powder pattern fitting technique (IRF) and applying the fundamental approach to model peak shapes (FP).

hydrite turns out to be a rather stable mineral under the conditions simulated by our experiments, including peak shock pressure of almost 65 GPa. While we observed marked microstrain increase and significant decrease in domain size with increasing peak shock pressure, we did not observe any phase changes, either

high-pressure polymorphs, or any decomposition products. The invariance in unit-cell dimensions with changing pressure is consistent with observations of anhydrite + quartz mixtures shocked to 60 GPa in [20] and our preliminary results [21] but not with the data of Langenhorst et al. [22] who found strong correlation between the length of parameter *a* and shock pressure (maximum difference *ca* 0.2 rel. %). Our data on peak widths, domain size and microstrain seem to agree with features seen in powder patterns presented in [22] but quantitative comparison is not possible. Gradual narrowing of peaks above 40 GPa, thus, may support an idea of Langenhorst et al. [22] suggesting either solid-state recrystallization or melting with subsequent crystallization of anhydrite due to high post-shock temperature following compression to pressures more than 40-50 GPa.

**Acknowledgements:** X-ray diffraction experiments in transmission geometry were performed at the Bayerisches Geoinstitut under the EU "IHP – Access to Research Infrastructures" Programme (Contract No. HPRI-1999-CT-00004 to D.C. Rubie). Diffraction data in reflecting geometry were acquired when RS was a visiting scientist at the Dip. Scienze della Terra, University of Siena under the support of the CNR-NATO Outreach Programme Fellowship.

**References:** [1] Emiliani C. et al. (1981) *EPSL*, 55, 317-334. [2] Crutzen P.J. (1987) *Nature*, 330, 108-109. [3] Brett R. (1992) *GCA*, 56, 3603-3606. [4] Sigurdsson H. et al. (1992) *EPSL*, 109, 543-559. [5] Chen G. et al. (1994) *EPSL*, 128, 615-628. [6] Pope et al. (1997) *JGR*, 102 (E9), 21645-21664. [7] Yang W. and Ahrens T. J. (1998) *EPSL*, 156, 125-140. [8] Pierazzo E. et al. (1998) *JGR*, 103, 607-626. [9] Gupta S. et al. (2001) *EPSL*, 188, 399-412. [10] Pierazzo E. (2001) *LPS XXXII*, Abstract #1196. [11] Skála, R. et al. (2002) *GSA Spec. Paper*, 356, 571-585. [12] Agrinier P. et al. (2001) *GCA*, 65, 2615-2632. [13] Hörz F. (1970) *NASA TN*, D-5787, 1-18. [14] Duvall G.E. (1962) *Bull. Seism. Soc. Am.*, 4, 869-893. [15] Marsh S.P. (1980) *Shock Hugoniot Data*, Univ. Calif. Press. [16] Holland T.J.B. and Redfern S.A.T. (1997) *Min. Mag.*, 61, 65-77. [17] Coelho A. A. and Cheary R.W. (1997) *X-ray Line Profile Fitting Program, XFIT*. <ftp://ftp.minerals.csiro.au/pub/xtallography/koalariet>. [18] Rodríguez-Carvajal J. (2001) *FullProf2.k* – a computer program, <ftp://charybde.saclay cea.fr/pub/divers/fullp>. [19] Klug H.A. and Alexander L.E. (1974) *X-Ray Diffraction Procedures*. John Wiley and Sons. [20] Schmitt R.T. and Hornemann U. (1998) *LPS XXIX*, Abstract # 1019. [21] Skála R. and Hörz F. (2001) *MAPS*, 36, A192. [22] Langenhorst F. et al. (2003) *LPS XXXIV*, Abstract #1638.

**DIAPLECTIC GLASS CONTENT IN EXPERIMENTALLY SHOCK-LOADED QUARTZ DETERMINED BY X-RAY POWDER DIFFRACTION.** R. Skála<sup>1</sup>, F. Hörz<sup>2</sup> and F. Langenhorst<sup>3</sup>, <sup>1</sup>Czech Geological Survey, Klárov 3/131, CZ-118 21 Praha 1, Czech Republic, skala@cgu.cz, <sup>2</sup>NASA-JSC, SN-2, Houston, Texas 77058, USA, <sup>3</sup>Bayerisches Geoinstitut (BGI), University of Bayreuth, D-95440 Bayreuth, Germany.

**Introduction:** Quartz is the most common mineral of terrestrial crustal rocks and thus a widespread indicator for impact cratering and associated shock metamorphism. Planar deformation features (PDFs) are among the most prominent and diagnostic shock features in quartz and they represent thin lamellae of glass that formed via solid-state transformations. This so-called “diaplectic” glass becomes pervasive at higher pressures and results in optically isotropic and X-ray-amorphous phases that resemble texturally the original quartz grains (without evidence of melt flow).

In the past, it has been shown that the amount of this amorphous material in experimentally shock-loaded quartz correlates with peak shock pressure [1,2]. Both reports derive the glass content from density measurements of individual crystals employing the equation  $X(\%) = (\rho_x - \rho_0)/(\rho_x - \rho_{gl})$ , where  $\rho_x$  and  $\rho_0$  stands for X-ray and average (optical) density, respectively. The density of glass,  $\rho_{gl}$ , was adopted as  $2.2 \text{ g.cm}^{-3}$ . Though the same procedures had been applied, the resulting glass content differs significantly among the above studies as indicated in Fig. 1. In the present study, we are using a new approach – based solely on the integral intensity of a single, carefully selected reflection in the XRD pattern, and we will compare our data to those reported in the literature.

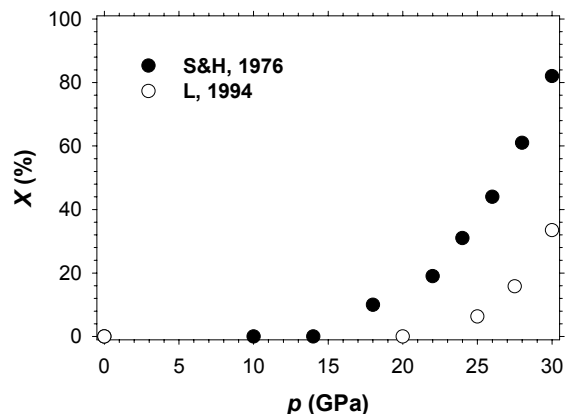


**Fig. 1.** Diaplectic glass content in experimentally shock-loaded quartz as reported by Schneider and Hornemann [1] and Langenhorst [2].

**Experimental:** For this study we shock-loaded double-polished disks of quartz (7.3 mm diameter; 1.0 mm thick; cut from a single, optical-quality crystal) with metal flyer plates that were launched with a 20

mm, powder-propellant gun [3]. The peak shock pressures attained by multiple reverberations were calculated by a graphical shock impedance method [e.g. 4] and ranged from 8.3 to 33.4 GPa (Table 1). Powder X-ray diffraction data for the samples were collected at the Czech Geological Survey employing a Philips X'Pert MPD System diffractometer with  $\text{CuK}\alpha$  radiation. TEM and SAED data of ion-thinned samples have been acquired using a Philips CM20 FEG transmission electron microscope at the Bayerisches Geoinstitut (BGI), Bayreuth.

**Table 1.** Experimental conditions for the shock recovery experiments on quartz targets.

Shot #	Flyer plate	Cover plate	$v_i$ (km/s)	$p$ (GPa)
3002	Lexan	SS304	1.739	8.34
3003	Al2024	SS304	1.281	15.90
3004	Al2024	SS304	1.436	18.16
941	Al2024	SS304	1.652	21.46
3193	SS304	SS304	1.126	23.14
3192	SS304	SS304	1.146	23.61
3005	Al2024	SS304	1.838	24.34
319	SS304	SS304	1.223	25.45
3006	SS304	SS304	1.240	25.87
3194	SS304	SS304	1.250	26.11
3010	SS304	SS304	1.312	27.63
3009	SS304	SS304	1.338	28.27
956	SS304	SS304	1.359	28.94
3011	SS304	SS304	1.424	30.43
3013	SS304	SS304	1.557	33.43

**Method:** Determination of the diaplectic glass content in quartz can be understood as the analysis of the mixture consisting of the 2 components: crystalline quartz and diaplectic silica glass. Obviously, both components in this mixture have the same mass absorption coefficient  $\mu^* = 35.89 \text{ cm}^2.\text{g}^{-1}$ . In such a case one can directly relate the intensity of a specific diffraction line in the diffractogram to the concentration of the corresponding crystalline phase as described in [5]. Consequently, we measured the integral intensity of the (101) diffraction line of quartz to calculate the absolute quartz content, with the remaining fraction (to 100 %) reflecting the absolute diaplectic glass content. Determination of the intensity of the (101) reflection in the step-scanned powder diffraction pattern has been carried out with the software program XFit [6].

**Results:** Qualitative phase analysis using the Bede ZDS Search/Match and ICDD PDF2 database programs did not reveal any crystalline compounds in the samples studied other than  $\alpha$ -quartz. The only major difference, immediately apparent from side-by-side comparisons of individual powder patterns, was the broadening of peaks and decrease in relative height, as well as the appearance of broad diffraction phenomena due to decreased long-range-order. The measured integral intensities of the (101) diffraction line were converted to diaplectic glass content applying the equation  $X(\%) = 100 \times (I_0 - I_s)/I_0$ , where  $I_0$  and  $I_s$  represent the intensity measured for the unshocked material and shocked sample, respectively. Results of these calculations are shown in Fig. 2.

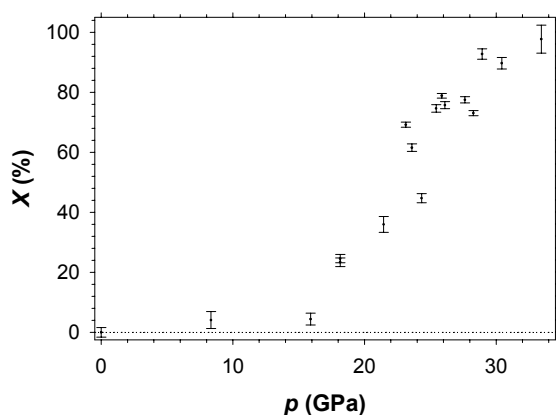


**Fig. 2.** Glass content in experimentally shock-loaded quartz calculated from the intensity of (101) diffraction line.

The relatively high content of amorphous material reported here has also been confirmed independently with BF and DF TEM and SAED imaging. At low pressures, one observes well-defined thin PDFs, whereas at higher pressures the PDFs widen and coagulate. For example, in the sample shocked to 33 GPa, only rare small patches of crystalline material remain, the rest being completely converted to glass (Fig. 3).

**Discussion:** This powder diffraction study confirmed the positive correlation between the glass content and peak shock pressure in experimentally shocked quartz. There is almost no amorphous material (below 5 %) up to the pressure of 16 GPa. At 18 GPa, the glass content increases abruptly reaching almost 25 %. From this point on, a relatively tight linear correlation between modal glass content and pressure occurs up to 33 GPa where less than 5 % of material remains crystalline.

When compared to the existing literature data [1,2], our results seem to be closer to those by Schneider and

Hornemann [1]. The differences between datasets might have several reasons such as variations in temperature history and quality of precursor crystal.

The method we described offers good reproducibility as exemplified by two measurements carried out for shot #3004 (18.2 GPa) which yielded identical results within experimental uncertainties (see Fig. 2). Also, the X-Ray method is completely independent of density measurements which are always associated with substantial experimental uncertainties and consequently not very accurate, if not error-prone. The XRD method should provide the more reliable data because the intensity measurements are relatively accurate as well as reproducible.

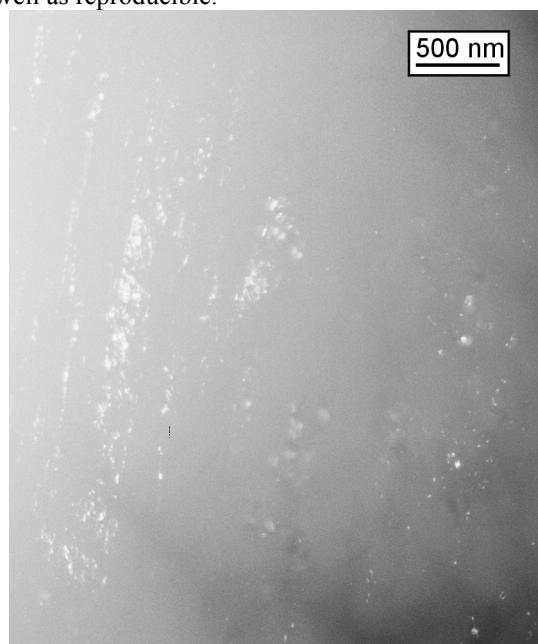


**Fig. 3.** Dark-field TEM image of the sample #3013 shock-loaded to 33 GPa. Sample contains rare patches of crystalline material (white) embedded in glass (gray).

**Acknowledgements:** The TEM studies were performed at the Bayerisches Geoinstitut under the EU "IHP – Access to Research Infrastructures" Programme (Contract No. HPRI-1999-CT-00004 to D.C. Rubie).

**References:** [1] Schneider H. and Hornemann U. (1976) *Contrib. Mineral. Petrol.*, 55, 205-215. [2] Langenhorst F. (1994) *EPSL*, 128, 683-698. [3] Hörz F. (1970) *NASA TN, D-5787*, 1-18. [4] Duvall G.E. (1962) *Bull. Seism. Soc. Am.*, 4, p. 869-893 and Marsh S.P. (1980) *Shock Hugoniot Data*, Univ. Calif. Press. [5] Klug H.A. and Alexander L.E. (1974) *X-Ray Diffraction Procedures*. John Wiley and Sons. [6] Coelho A. A. and Cheary R.W. (1997) *X-ray Line Profile Fitting Program, XFIT*. <ftp://ftp.minerals.csiro.au/pub/xtallography/koalariet>.

**CHILLING EVIDENCE FOR THE BULK COMPOSITION OF THE IMPACT MELT SHEET AT SUDBURY: EVIDENCE FROM OFFSET DYKES.** John G. Spray<sup>1</sup>, Alain J. Murphy<sup>1</sup>, Cliff S.J. Shaw<sup>1</sup> and Martin G. Tuchscherer<sup>1</sup>, Planetary and Space Science Centre, Department of Geology, University of New Brunswick, 2 Bailey Drive, Fredericton, New Brunswick E3B 5A3, Canada. Corresponding author's email address: jgs@unb.ca

**Introduction:** Determining the bulk composition of impact-generated melt sheets in impact structures presents a number of difficulties. For small (simple) structures, local splash melts may provide viable indicators. However, there is some debate as to whether melt ejecta represent bulk fused target compositions, or whether they represent specific layers, successfully revealed and removed during penetration and excavation. For ejecta, the latter scenario would appear more likely. For larger (complex) structures, and especially peak-ring and multi-ring basins, there is the likelihood of impact melt differentiation, such that the original bulk melt is not preserved. In these cases, the original impact melt composition can be determined by carefully reassembling individual layer compositions and thicknesses. In the case of the Sudbury impact structure of Ontario, Canada, estimates of the original bulk composition have been determined by several workers over the last century using the reassembly approach. An alternative and more direct method is afforded by the chilled margins of impact melt dykes that penetrate the footwall. Because of their limited dimensions and their juxtaposition with relatively cold country rock, such dykes can effectively isolate impact melt from subsequent differentiation and so retain their more primitive composition. This work concerns the use of chilled margins of certain Offset Dykes at Sudbury to constrain to bulk composition of the original impact melt. These compositions are used to model the evolution of the Sudbury igneous complex (SIC), Sublayer and related economic deposits.

**Offset Dykes:** Sudbury is distinctive amongst the terrestrial impact structures in that well-developed radial and concentric dykes are now exposed below the remains of what was originally the impact melt sheet. These are referred to as Offset Dikes [1,2]. They are of considerable economic importance as hosts to many of the Ni-Cu-platinum group element (PGE) deposits, for which Sudbury is renowned. Within the impact paradigm, the offset dikes also provide critical insight into the excavation and modification stages of the impact process, which in turn places temporal and spatial constraints on ore genesis and ore distribution. Only Vredefort shows comparable features in the form of the

Granophyre dykes that occupy the central uplift and collar regions [3].

Following extensive field work and sampling [4, 5], two chilled margin locations from the Foy Offset Dyke and inclusion-poor quartz diorite samples from the Whistle-Parkin Offset Dyke were selected. Major, trace and rare earth element analysis of these samples facilitates the modelling of fractional crystallization of the melt sheet based on a knowledge of cumulate layer thicknesses, known mineralogy of the cumulate units, and published partition coefficients.

The results yield a more realistic indication of the bulk composition of the Sudbury impact melt body. Moreover, the new data provide bulk trace and rare earth element information that is difficult to extract from averaging layer thicknesses and their compositions. In addition, by carefully modelling the evolution of the impact melt sheet, it is possible to provide constraints on the original volume of Cu-Ni sulfides and platinum-group elements that were precipitated from the melt body. This yields important new information on ore reserves, which has profound economic implications.

Sudbury provides one of the best exposed and best preserved, large (>100 km diameter) impact structures on Earth. Determining the bulk composition of its impact melt sheet through the discovery of well-preserved chilled margins enables us to explore how a large, superheated melt body evolves through time and generates world-class ore deposits.

**References:** [1] Coleman, A.P. (1903). *Ontario Bureau of Mines Report 103*, 235-303. [2] Grant, R.W. and Bite, A. (1984). *Ontario Geological Survey Special Volume 1*, 275-300. [3] Therriault, A.M., Reimold, W.U. and Reid, A.M. (1997). *South Afr. J. Geol.* 100, 115-122. [4] Tuchscherer, M.G. and Spray, J.G. (2002) *Econ. Geol.* 97, 1377-1397. [5] Murphy, A.J. and Spray, J.G. (2002) *Econ. Geol.* 97, 1399-1418.

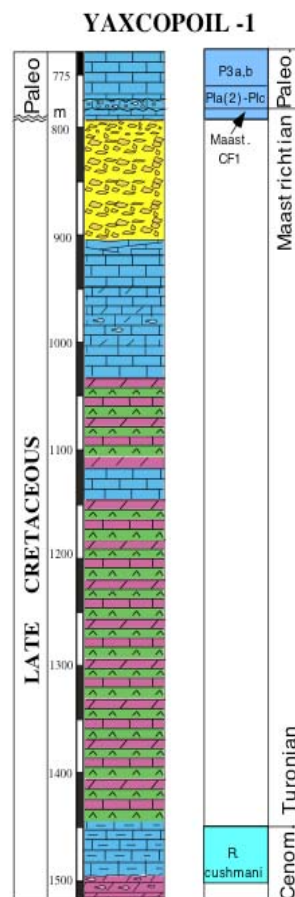
**YAXCOPOIL-1 AND THE CHICXULUB IMPACT** W. Stinnesbeck<sup>1</sup>, G. Keller<sup>2</sup>, T. Adatte<sup>3</sup>, M. Harting<sup>4</sup>, D. Stüben<sup>4</sup>, <sup>1</sup>Geologisches Institut, Universität Karlsruhe, 76128 Karlsruhe, Germany; <wolfgang.stinnesbeck@bio-geo.uni-karlsruhe.de><sup>2</sup>Department of Geosciences, Princeton University, Princeton 08544, USA; <sup>3</sup>Geological Institute, University of Neuchâtel, Neuchâtel, CH-2007, Switzerland; <sup>4</sup>Institut für Mineralogie und Geochemie, Universität Karlsruhe, 76128 Karlsruhe, Germany

We examined the lithology, stratigraphy and mineralogy of the CSDP well Yaxcopoil-1, which was drilled on the southern inner flank of the Chicxulub impact crater, approximately 60 km from its center [1]. Between 775m and 1511m depth we identified 10 major bio- and lithostratigraphic units. The lower part of the core up to 894m contains a sequence of limestones, dolomites and anhydrites of late Cretaceous ages. Lithologies, microfacies and fossil contents indicate deposition occurred in various carbonate platform environments (e.g., sabkha, lagoons). In addition, a marly limestone between 1511 and 1495m contains abundant planktic foraminifera that reflect an open marine shelf environment of latest Cenomanian age (top *R. cushmani* Zone).

A prominent 100m thick suevitic breccia between 794-894m reveals upward-fining and reworking by ocean water in the top 15m of this unit. Latest Maastrichtian dolomitic limestones overlie the suevite and contain planktic foraminiferal assemblages indicative of the *Plummerita hantkeninoides* zone CF1, which spans the last 300 ky of the Maastrichtian. An erosional surface 55cm above the breccia/dolomite contact marks the K/T boundary and a hiatus. Limestones above this contact contain the first Tertiary planktic foraminifera indicative of an upper *P. eugubina* zone P1a(2) age and deposition in a quiet open marine shelf environment. 7 cm upsection, another hiatus separates zone P1a(2) and limestones of planktic foraminiferal Zone P1c. Planktic foraminiferal assemblages of Zone P1c to P3b age are present from a depth of 794.04m up to 775m and indicate open shelf environments that become increasingly more proximal as indicated by debris flows from nearby shallow carbonate platform environments.

The Cretaceous sediment sequence is largely parautochthonous, with a stratigraphical sequence comparable to Cretaceous sediments known from outside the Chicxulub crater and correlatable biohorizons over several hundred kilometers in northern and southern Yucatan. This supports the presence of normal deposition rather than an interpretation as chaotic megablocks sliding into the Chicxulub crater. Our investigation revealed no evidence for major disruption of sediments, chaotic changes in lithology, overturned or deep dipping megablocks, or major mechanical fragmentation, shock alteration or ductile deformation.

Breccia units intercalated in the carbonate platform sequence show conformable and sometimes gradational contacts to under- and overlying non-brecciated sediments and appear to be of intraformational origin (e.g., dissolution of evaporites), rather than a consequence of instant shaking and shearing. No glass spherules or altered glass shards are present in any of these layers and no basement rocks or other exotic clasts were detected. No melt rock has been detected and only two dyke-like injection veins were positively recognized at a depth of 1399m and 1348m, and two suevitic breccia dykes (at 915m and 909m) close to the contact between Cretaceous sediments and overlying suevite.



The contact between suevite and overlying hemipelagic carbonates of late Maastrichtian age is abrupt and there is no evidence for reworking. The

complete absence of reworked suevitic breccia material in the uppermost Maastrichtian and lowermost Paleocene limestone sequences, the incomplete K/T boundary record, and the reduced thickness or even absence of early Paleocene faunal zones relate to normal sedimentation interrupted by non-deposition due to current activity and sea level changes that are characteristic of the Caribbean area. There is no sedimentological evidence for compaction, mass sliding and subsequent shaking during the post-impact period.

The Cretaceous sediment sequence indicates that Yaxcopoil-1 is located outside the transient crater cavity, either on the upper end of an elevated and tilted horst of the terrace zone or even outside the annular crater cavity. Major disturbances of strata by the impact appear to have been confined to less than 60km from the proposed impact center. Chicxulub thus represents a fairly large impact event that predates the larger K-T boundary impact event, known from global Ir anomalies, by about 300 ky[2].

[1] Dressler B.O. et al. (2003) *EOS*, 85, 125, 130.

[2] Keller G. et al. (2002) *Earth Science Reviews* 1283, 1-37.

**Acknowledgements:** This work was supported by the German Science Foundation grants STI 128/7-1 to 3, and STU 169/10-1 to 3, and the Swiss National Fund No. 8220-028367 (TA). We also want to acknowledge the International Continental Drilling Program, the Chicxulub Scientific Drilling Project team, and the Universidad Nacional Autónoma de México.

**ORIGIN AND EMPLACEMENT OF THE IMPACT FORMATIONS AT CHICXULUB, MEXICO, WITH SPECIAL EMPHASIS ON THE YAX-1 DEEP DRILLING.** D. Stöffler<sup>1</sup>, B. A. Ivanov<sup>2</sup>, L. Hecht<sup>1</sup>, T. Kenkmann<sup>1</sup>, R. T. Schmitt<sup>1</sup>, T. Salge<sup>1</sup>, F. Schönian<sup>1</sup>, R. Tagle<sup>1</sup>, S. Weseler<sup>1</sup>, and A. Wittmann<sup>1</sup>, <sup>1</sup>Institute für Mineralogie, Museum für Naturkunde, Invalidenstr. 43, 1099 Berlin, Germany, dieter.stoeffler@rz.hu-berlin.de, <sup>1</sup>Institute for Dynamics of Geospheres, Leninsky Prospect, 38, bldg.1, 119334, Moscow, Russia, baivanov@idg.chph.ras.ru,

**Introduction:** The ICDP drilling Yaxcopoil-1, located in the annular ring trough of the 190 km Chicxulub peak ring impact basin, exposes some 715 m of impact-related lithologies below 795 m of post-impact Tertiary sediments [1]. We use 2D numerical modeling of the impact event to reproduce the crater growth and collapse and main ejecta mass deposition at the point where Yax-1 is located.

**Main Results of the Yax-1 Drilling and Comparison with Profiles from other Drill Holes:** The profile of Yax-1 reveals two major impact related formations: 100 m of suevite-type breccias resting on top of a 615 m thick, displaced Cretaceous limestone-dolomite-anhydrite sequence which is cut by polymict and monomict impact breccia dikes [2, 3]. The suevite can be subdivided into 6 subunits which represent polymict, allochthonous material derived predominantly from the crystalline basement (melt, clasts) and from Cretaceous carbonate rocks (clasts and minor carbonate melt) [2]. The Cretaceous unit has the characteristics of a displaced megablock with deformation and dike features indicative of an origin from the upper, near-rim section of the pre-impact target rocks [3]. Previous drillings (PEMEX and UNAM) indicate a characteristic radial variation of the type, thickness, and stratigraphy of the allochthonous breccia and melt formations [4]: Coherent impact melt layer topped with suevite in the central depression inside the peak ring and in the inner zone of the annular trough, megablocks and polymict lithic breccias overlain discontinuously by suevite-like breccias and minor melt rock layer in the outer part of the annular trough and in the ejecta blanket beyond the final crater rim. The suevite/melt units and the polymict lithic breccias range in thickness from 0 to 330 m and from 300 to ~900 m at 1 – 2 crater radii, respectively.

**Implications of the Observational Data for the Origin and Emplacement of the Impact Formations:** The lithologies at Yax-1 (~ from 60 km from the point of impact) appear to be derived from upper target rocks (Cretaceous megablock) displaced from the original position during the crater modification stage, from ground-surgled material flow moving radially outward during the transient cavity formation and during its collapse phase (suevite units 6 and 5), from material falling back from the lower ejecta plume in an early phase (units 4 and 3), and from material of the upper plume settling back through the restored

atmosphere (sorted suevite units 2 and 1) in a late phase. The impact formations exposed in the other drillings are interpreted as follows: The sorted suevite may not be preserved in the ejecta blanket. The lithic breccias appear to be deposited from the ejecta curtain moving outward beyond the crater rim. The suevite from the earlier phase is obviously discontinuously deposited on top of the ejecta blanket beyond the crater rim as also known from the Ries crater [5].

**Modeling Results for the Crater Formation, Collapse of Transient Cavity, Collapse of Ejecta Plume and Late Crater Modifications:** The general philosophy of the Chicxulub impact crater formation [6] assumes a chain of consecutive models increasing in accuracy. The first order of accuracy model we use here includes two-dimension (2D) modeling of a vertical impact into a two-layer target (crust/mantle or sediments/crystalline basement). The aim of the modeling is to simulate the shock wave passage through the target rocks, transient cavity growth and following gravity-driven collapse. No atmosphere is included into the modeling. Hence, only motion of large rock masses is computed adequately. The formation and evolution of a dusty vapor plume for an oblique impact is presented as a separate study [7].

*Overview of the crater formation process.* The numerical modeling allows us to reveal the main stages of impact. The shock wave, propagating through the target is slightly reflected at the crust/mantle (Moho) boundary and transforms to stress (and later to seismic) waves. An important marker for the shock wave decay in comparison with observations is the shape and size of the melting zone. For this purpose one can use simple estimates of the shock pressures for incipient melting (after pressure release) and complete melting which is 46 and 56 GPa, respectively, according to [8] for the granite - ANEOS. Depending on the assumed projectile size and velocity the computed total melted volume varies from 5,000 to 12,000 km<sup>3</sup>. Amazingly, only a small amount of this melt is ejected beyond the transient cavity margin. Partially this is an effect of a vertical impact; oblique impacts may splash out more melt.

During the transient crater collapse part of impact melt is trapped between rock masses moving to the center line where the melt forms a ~ 20 km deep “rod” (Fig. 2). In modeling, this melt is pure melt, but in reality this melt should be mixed with solid clasts as

seen in the ground surged suevite and clast-rich melt rocks at Yax-1.

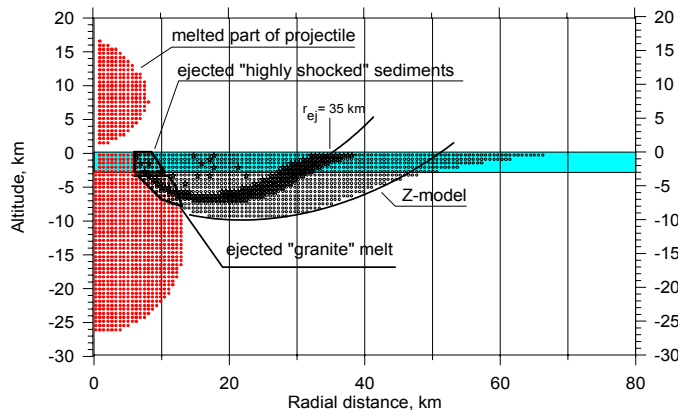


Fig. 1

**Transient cavity.** It reaches its maximum depth of 26 to 35 km (Moho depth at  $\sim 33$  km) within 17 to 20 seconds. The cavity floor immediately begins to rise up (well before the end of excavation). The maximum transient cavity volume is achieved at  $\sim 40$  seconds after impact. Then the transient crater volume begins to decrease to its residual value which is a factor of 4 to 5 smaller than the maximum value. The motion of the target material stops at 400-600 seconds after impact. This value ( $\sim 10$  minutes) can be used as an effective measure of the morphological crater formation duration. The Cretaceous surface (Fig. 2) in the model is subsided and has an average dip angle of 6 to 7 degrees (terraces cannot be reproduced at the available resolution). The hinge zone of Cretaceous (pre-impact) surface is at a distance of  $\sim 45$  km from the center giving a good estimate of the modeled transient crater radius. At a later time the crater structure may be modified on a fine scale, possibly by sea water back-slash, by prolonged fallout of fine particles from the crater plume, and, at a longer time scale, by subsidence due to thermal contraction of subcrater rocks, slowly cooling down with the time, and finally by long term isostatic relaxations which may even be related to the slight displacement ( $\sim 1$  km) of the crust-mantle boundary.

**Ejecta deposition at Yax-1 site.** Massless tracer particles allow to trace the motion of material ejected out of the transient cavity and sedimented at a distance of 60 km from the center (Yax-1). The current resolution is not high enough to make a detailed analysis. In the first step low-resolution modeling (computational cells 500x500 m or 300x300m) the number of tracers with a final distance of 60 km is not large. To make first order estimate we analyze all particles which landed (and stopped) at distances 55 to 65 km. Fig. 1 shows the initial position of these ejecta in relation to the melt and ejecta zones. The ejecta at the Yax-1 site

originate from a "stream tube" crossing the surface at  $\sim 35$  km off the center. Mostly clastic material and relatively little basement melt is ejected. For the ballistic transport over a distance of 25 km (from 35 to 60 km) an ejection and deposition velocity of  $0.5 \text{ km s}^{-1}$  is required causing a relatively violent process of the ballistic sedimentation at the Yax-1 site in agreement with what is observe in the lowermost layers of suevite in the Yax-1 drill core.

**Ejecta properties and thickness at the Yax-1 site.**

The average effective ejecta thickness (assuming the density of the original material) varies from 200 to 400 m if averaged over 55-65 km ring zone. Azimuthal variations and bulking of the fragmented material may change this value by factors of  $> 2$  up and down. The fraction of crystalline clasts varies with projectile size and velocity (see [6]) and is typically around 0.5 (roughly equal amounts of sedimentary and crystalline clasts). The shock state of basement clasts varies from 5 to 45 GPa with a dominance of clasts experienced shock pressure 5 to 10 GPa ( $\sim 40\%$  by mass).

**Conclusions:** Drilling data provide an important opportunity to test the numerical models against the natural impact event and vice versa. In many respects the model presented here is in agreement with the observations except for the fact that the Yax-1 impactites are much more melt-rich than the model predicts.

**Acknowledgement.** BAI thanks the "Von Humboldt Foundation" for the support of his work, the other authors acknowledge support by DFG.

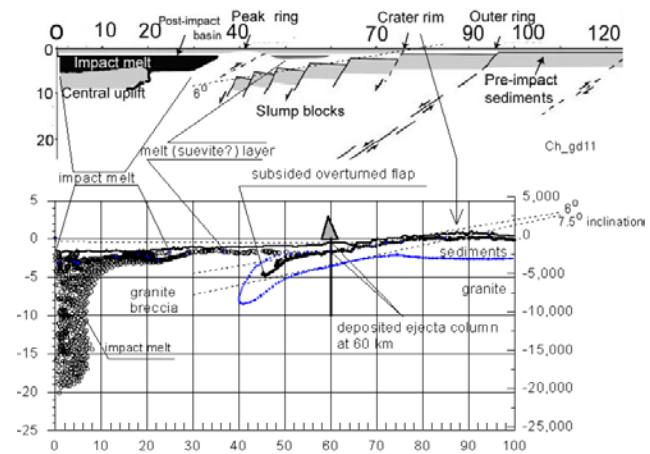


Fig. 2

**References:** [1] Dressler B.O. et al. (2003) *EOS* 184, 125, 130. [2] Stöffler D. et al. (2003) *LPS XXXIV*, Abstract #. 1553. [3] Kenkmann T. et al. (2003) *LPS XXXIV*, Abstract # 1368 [4] Urrutia et al. (2001) *Geophys. Res. Lett.*, 23, 1565-1568. [5] Stöffler D. and Ostertag (1983) *Fortschr. Min.*, 61, 71-116. [6] Ivanov B. A. (2003) this volume. [7] Artemieva N.A. et al. (2003) this volume. [8] Pierazzo E. et al. (1997) *Icarus*, 127, 408-432.

**SIMULATIONS OF VERY LARGE IMPACTS ON THE EARTH.** V. V. Svetsov, Institute for Dynamics of Geospheres RAS, Leninsky Prospekt 38-1, Moscow, 119334, Russia, svetsov@idg.chph.ras.ru

**Introduction:** The largest impact craters discovered on the Earth, from 200 to 300 km in diameter, could be produced by collisions with asteroids 10–20 km in size. However, the early Earth experienced intense bombardment of much larger bodies. The impacts of bodies 10–100 km in size have been studied in detail in numerous works. Giant impacts of Mars-sized bodies against the early Earth have been modelled and studied relatively well in several works [1, 2]. The authors of [3] carried out numerical simulations of vertical impacts of asteroids from 10 to 1600 km in size at 20–30 km/s. This is the only paper covering the range of asteroid sizes from 100 to 1000 km, however, many outcome characteristics of these impacts, necessary for determination of the early Earth state, have not been reported and the range of impact velocities did not include typical collision velocities which are smaller than 20 km/s.

In this work, numerical hydrodynamic simulations have been made for vertical impacts of asteroids, from 100 to 1000 km in diameter, on the Earth. Impact velocities were from 10 to 20 km/s. The purpose of the simulations was to obtain the most important characteristics of the impacts: energy partitioning and mass distribution, mass captured to Earth-bound orbits and mass escaping the Earth gravitational field.

**Numerical model:** The large impacts considered in this paper have global consequences so that the sphericity of the planet must be taken into account. On the other hand, the mass of a 1000-km asteroid is only about 0.025 % of the Earth's mass and the planetary gravitational field is influenced by these impacts only slightly, so this field is considered to be central and constant. A state of the early Earth was assumed to be identical to the state of the modern Earth. The density of the preimpacted undisturbed spherical Earth was taken from the PREM model [4]. The uppermost layers of low density associated with oceans were changed for stony. The pressure inside the Earth was determined by the hydrostatic equation.

The simulations were based on the hydrodynamic equations. The spherical system is the most natural for the simulations due to Earth sphericity, however, it is suitable only for the problems in which the motion of the centre is insignificant because the origin of the coordinates is a singular point. For the impacts of 1000-km-diameter and smaller asteroids the Earth's inner core is subjected only to slight disturbances, so the spherical system of coordinates was used. Two kinds of equations of state – Tillotson's and ANEOS were used. The mantle was treated as dunite. If the density in the Earth's upper layers was lower than  $3.32 \text{ g/cm}^3$  (normal

density of dunite) EOS for granite was used. The projectile was assumed to be made of granite. Strength of the Earth material was neglected.

An Eulerian method SOVA developed for multi-material flows in [5] was used for the simulations, however, some important modifications of the method have been made here for spherical geometry in which additional terms appear in the hydrodynamic equations. The modifications have been made to provide accurate conservation of kinetic, internal and potential energies. The code calculates the potential and kinetic energies and angular moment of each cell mass, determines the orbits, and calculates the whole masses which are on elliptical and hyperbolic orbits.

The mesh was not uniform. The smallest cells were arranged in the vicinity of the impact site and at the Earth surface. The best mesh resolution was from 20 to 180 cells per a projectile diameter. The total number of cells varied from 65 to 300 thousands. To follow the motion of Earth layers, passive particles representing different material domains were used. The number of tracer particles was from 100 to 300 thousands.

**Numerical results:** After the impact of a 1000-km-diameter asteroid the transient crater is produced mainly by compression of the target material, not by excavation. The upward motion of dense material begins in several minutes after the impact and the maximum lift to a height about 1500 km above the Earth surface occurs in 15 min, then the dense column falls back forming a shallow crater in 40 min. Then the material rebounds upward and the surface continues to oscillate. The transient crater diameters following from the scaling law [6] are 510 and 3200 km for 100 and 1000 km impactors. The numerical simulations give smaller values: 400 and 2000 km respectively.

The flow initiated by large impacts is connected with transformations of energy. The main part of the impactor kinetic energy initially goes to the heating of the target and then the internal energy acquired by the target transforms into potential energy of the rising material. During the first lift the potential energy of the whole system exceeds the initial kinetic energy of the projectile due to release of elastic energy stored in the compressed layers of the Earth interior. When the ejecta falls back, it spreads over the Earth surface. Some part of the impactor particles collide at the point antipodal to the impact. No asteroid material remains below the Earth's surface except for the initial cratering dynamics because of the dense uplifting target material. In about an hour the material of the deep mantle comes up to the surface and spreads over it.

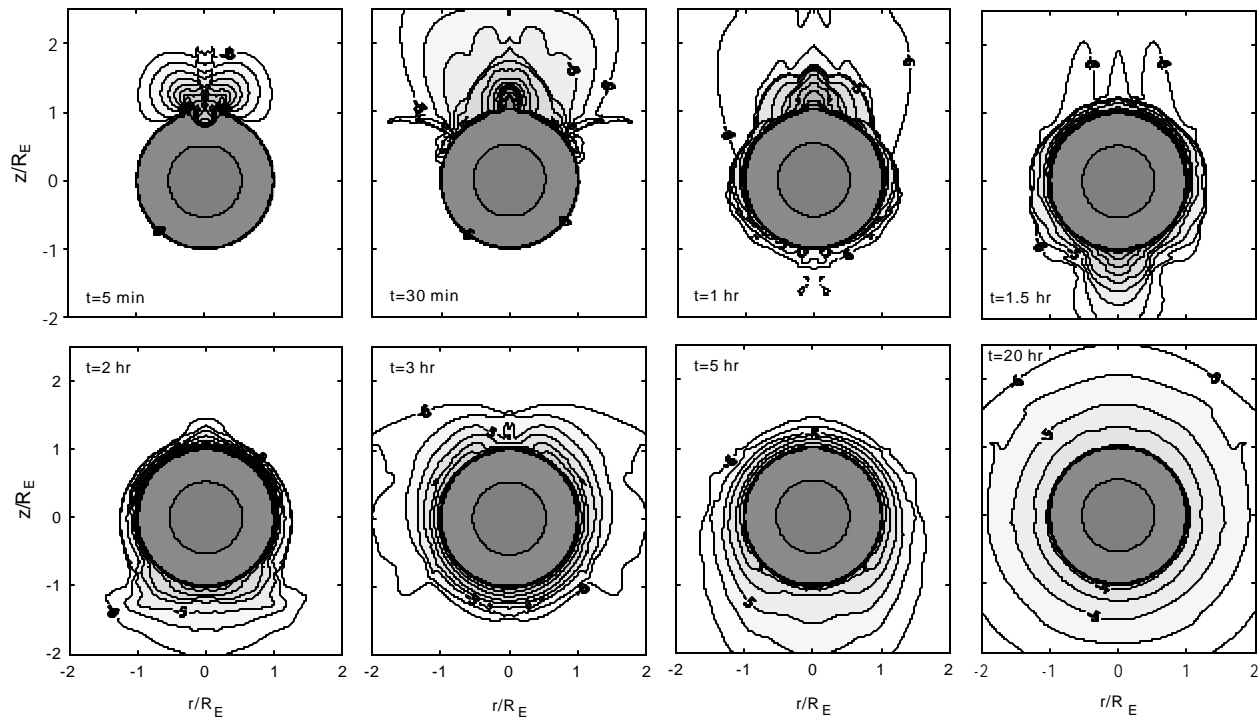


Fig.1. Contours of constant density in the flow around the Earth after the impact of a 1000 km asteroid at 20 km/s. The contours are plotted with an interval  $10^{0.5}$  (in the logarithmic scale) from  $10^{-6}$  g/cm<sup>3</sup> (the outer contour) to 10 g/cm<sup>3</sup> (the inner contour located in the Earth core near its boundary).

Figure 1 shows how the vapour plume expands to several Earth radii and then falls to the Earth. The silicate atmosphere oscillates during hours and in about 20 hours settles into equilibrium. (Estimates [7] show that it will take a few months to radiate away the energy of the rock vapour atmosphere.)

The calculations of escaping masses show that they are small and depend both on the mesh resolution and equation of state. The simulations with ANEOS at  $V=20$  km/s give that only from 1 to 1.5 percent of the impactor mass escapes the Earth gravitational field. This depends on the impactor diameter only slightly. The escaping mass is about 0.3 % for  $V=15$  km/s and an order of magnitude smaller for  $V=10$  km/s. If the Tillotson equation of state was used for the projectile, the escaping mass was from 4 to 7 percents for  $V=20$  km/s. The mass on elliptical orbits was smaller than 0.1%. However, this mass must be bigger for oblique impacts.

The state of the whole Earth is changed after large impacts. For the impact of a 1000 km asteroid at 20 km/s about half of the impactor energy is released as thermal energy. The space far below the impact site becomes filled by the hotter material risen from the depth. In 2 hours, the upper layers of the Earth at the impact site have lower internal energy than before the impact, and the layers at distances larger 5000 km from the impact

site along the surface are hotter in comparison to the state of the preimpacted Earth due to the fall of ejecta.

**Conclusions:** The SOVA code modified for spherical geometry makes possible to simulate the flow after large impacts with acceptable accuracy. However for long times the model must include viscosity and friction. The cratering process has specific features for large impacts, most important is the gravity which plays an important role from the earliest stages of cratering. The impacts cause the lifts of dense material to great heights and the upward motion of deep mantle layers. A big part of the impactor kinetic energy transforms into the potential energy of lifted material

**References:** [1] Cameron A.G.W. (2000) In *Origin of the Earth and Moon*, Univ. Arizona Press, Tucson, 2000. pp. 133-144. [2] Canup R.M. and Asphaug E. (2001) *Nature*, 412, 708-712. [3] Jach K., Leliwa-Kopystynski J., Mroczkowski M., Swierczynski R., Wolanski P., Gault D. E. and Wedekind J. A. (1994) *Earth. Planet. Space Sci.*, 42, 12, 1123-1137. [4] Dzievonski A.M. and Anderson D.L. (1981) *Phys. Earth Planet. Inter.* 25, 297-356. [5] Shuvalov V.V. (1999) *Shock Waves*, 9, 6, 381-390. [6] Schmidt R.M. and Housen K.R. (1987) *Int. J. Impact Engng.*, 5, 543-560. [7] Zahnle K.J. and Sleep N.H. (1996) In *Comets and the Origin and Evolution of Life*, Springer-Verlag, New York, pp. 175-208.